TRƯỜNG ĐẠI HỌC QUY NHƠN
QUY NHON UNIVERSITY

TẠP CHÍ KHOA HỌC
JOURNAL OF SCIENCE

CHUYÊN SAN KHOA HỌC TỰ NHIÊN VÀ KỸ THUẬT
ISSUE: NATURAL SCIENCES AND ENGINEERING

15 (5)
2021

BÌNH ĐỊNH, 10/2021

MỤC LỤC

1. Nghiên cứu khả năng bắt giữ khí thải của vật liệu khung hữu cơ kim loại Ni(BDC)$(TED)_{0,5}$ bằng phương pháp mô phỏng cổ điển
Nguyễn Thị Xuân Huynh, Bùi Thị Duyên, Phạm Thảo Trâm, Trần Thị Diễm Thanh, Nguyễn Trương Mỹ Duyên.....5

2. Ứng dụng Raspberry và PLC Mitsubishi trong thiết kế hệ thống tự động phân loại cà chua
Bùi Văn Vũ, Nguyễn Đức Thịnh, Phạm Thanh Bình, Đỗ Văn Cần.....13

3. Phân tích quá trình điện từ của máy biến áp khi đóng vào lưới điện bằng phần mềm Ansys Maxwell
Đoàn Thanh Bảo, Hà Huỳnh Huy Vũ.....21

4. Thiết kế hệ thống điều khiển và giám sát theo hướng thông minh cho đô thị có hệ thống chiếu sáng phân tán
Lê Thái Hiệp, Đinh Quốc Đạt.....29

5. Phân lớp ảnh điện tâm đồ bằng kỹ thuật học sâu hỗ trợ chẩn đoán bệnh tim mạch
Lê Xuân Vinh, Lê Xuân Việt, Vũ Hoàng Thương.....39

6. Nghiên cứu lý thuyết sự hấp phụ sulfamethoxazole trên bề mặt rutile-TiO_2 (110) bằng phương pháp hóa học lượng tử
Nguyễn Ngọc Trí, Nguyễn Tiến Trung.....47

7. Bài toán ước lượng lỗi H∞ cho một lớp hệ có trễ sử dụng một phép biến đổi trạng thái mới
Đặng Thị Kiêm Hồng, Lê Bá Thông, Đinh Công Hướng.....55

8. Khảo sát các chế độ làm việc của hệ thống chỉnh lưu PWM - động cơ điện một chiều kích từ độc lập
Bùi Văn Vũ, Võ Phương, Đỗ Văn Cần, Lê Thái Hiệp.....75

9. Nghiên cứu điều chế mỡ bôi trơn từ dầu nhờn thải tái sinh
Lê Thu Hương, Trương Thanh Tâm.....87

TẠP CHÍ KHOA HỌC
TRƯỜNG ĐẠI HỌC QUY NHƠN

Nghiên cứu khả năng bắt giữ khí thải của vật liệu khung hữu cơ kim loại $Ni(BDC)(TED)_{0,5}$ bằng phương pháp mô phỏng cổ điển

Nguyễn Thị Xuân Huynh[1,*], Bùi Thị Duyên[2], Phạm Thảo Trâm[2], Trần Thị Diễm Thanh[2], Nguyễn Trương Mỹ Duyên[2]

[1]Khoa Khoa học Tự nhiên, Trường Đại học Quy Nhơn, Việt Nam
[2]Khoa Sư phạm, Trường Đại học Quy Nhơn, Việt Nam

Ngày nhận bài: 19/04/2021, Ngày nhận đăng: 30/05/2021

TÓM TẮT

Sự phát thải các khí độc hại tác động tiêu cực ồ ạt đến môi trường và sức khỏe của con người như CO_2 và SO_2 do sự tăng nhanh dân số toàn cầu và việc đốt ngày càng nhiều nhiên liệu hóa thạch để đáp ứng nhu cầu năng lượng. Song song với việc tìm ra nguồn năng lượng thay thế nhiên liệu hóa thạch, việc tìm ra một biện pháp để bắt giữ, giảm tải và xử lý khí thải độc hại ra môi trường, gây hiệu ứng nhà kính cũng hết sức quan trọng và cấp bách nhằm ngăn chặn sự biến đổi khí hậu ngày càng trầm trọng hơn. Vật liệu khung hữu cơ kim loại $Ni(BDC)(TED)_{0,5}$ được đánh giá là vật liệu xốp có khả năng hấp phụ mạnh CO_2 và SO_2. Bằng phương pháp mô phỏng Monte Carlo chính tắc lớn, chúng tôi đã đánh giá được khả năng bắt giữ hai loại khí này của $Ni(BDC)(TED)_{0,5}$ với lượng hấp phụ SO_2 mạnh hơn CO_2 ở vùng áp suất thấp dưới 25 bar; trong khi đó, ở vùng áp suất cao, lượng hấp phụ CO_2 có khuynh hướng tăng (đạt 14,4 mmol/g ở 50 bar) nhưng hấp phụ SO_2 thì sớm bão hòa ở áp suất 5 bar với 13,6 mmol/g. Sự hấp phụ mạnh hơn của SO_2 so với CO_2 trong vùng áp suất thấp cũng được làm sáng tỏ qua nhiệt hấp phụ của SO_2 (32,7 kJ/mol) lớn hơn nhiều so với CO_2 (17,3 kJ/mol) trong $Ni(BDC)(TED)_{0,5}$.

Từ khóa: *$Ni(BDC)(TED)_{0,5}$, mô phỏng Monte Carlo chính tắc lớn, bắt giữ CO_2, bắt giữ SO_2, hấp phụ đẳng nhiệt.*

**Tác giả liên hệ chính.*
Email: nguyenthixuanhuynh@qnu.edu.vn

https://doi.org/10.52111/qnjs.2021.15501

JOURNAL OF SCIENCE
QUY NHON UNIVERSITY

Research on the capture of flue gases of the metal-organic framework Ni(BDC)(TED)$_{0.5}$ by the classical simulation method

Nguyen Thi Xuan Huynh[1,*] , Bui Thi Duyen[2], Pham Thao Tram[2], Tran Thi Diem Thanh[2], and Nguyen Truong My Duyen[2]

[1]Faculty of Natural Sciences, Quy Nhon University, Vietnam
[2]Faculty of Pedagogy, Quy Nhon University, Vietnam

Received: 19/04/2021, Accepted: 30/05/2021

ABSTRACT

The emission of toxic gases has massive negative impacts on the environment and human health such as CO_2 and SO_2 because of the rapid increase of the global population and the burning of more and more fossil fuels to meet energy needs. Together with seeking alternative clean energy sources, finding methods to capture, reduce and treat harmful gases in the environment is urgent to prevent climate change and global warming. The metal-organic framework Ni(BDC) (TED)$_{0.5}$ was evaluated as a porous material with strong adsorption of CO_2 and SO_2. By grand canonical Monte Carlo simulation, we quantitatively evaluated the capture capacities of CO_2 and SO_2 in Ni(BDC) (TED)$_{0.5}$ based on the adsorption mechanism. Our results indicated the adsorption of SO_2 was higher than that of CO_2 in the pressures below 25 bar. Meanwhile, in the high-pressure range, the CO_2 adsorption in Ni(BDC) (TED)$_{0.5}$ was still in increase, reaching 14.40 mmol/g at 50 bar, but SO_2 adsorption was soon saturated at the pressure of 5 bar with 13.6 mmol/g. The stronger adsorption of SO_2 compared with CO_2 in the low-pressure range was also elucidated by the isosteric heat of adsorption that was Q_{st} of SO_2 (32.7 kJ/mol), which was much greater than that of CO_2 (17.3 kJ/mol) on Ni(BDC) (TED)$_{0.5}$.

Keywords: *Ni(BDC)(TED)$_{0.5}$, grand canonical Monte Carlo, CO_2 capture, SO_2 capture, adsorption isotherms.*

1. INTRODUCTION

Flue gas emissions such as CO_2 and SO_2 have seriously affected the environment and human health. It is always the hot problem at conferences, workshops, and seminars due to the urgent need to find solutions to capture, treat and convert exhaust gases. Several studies have been performed on separating and capturing toxic gases from the gas mixture so far. Over the past few decades, adsorption-based gas capture and storage in porous materials have been noticed due to their extraordinary features such as high surface area, high pore, extra-high porosity up to 90% free volume, adjustable internal surface properties, and tunable pore size.[1] Many adsorbents have been investigated, such as activated carbon (AC), zeolite, silica gel (SG), and especially metal-organic frameworks (MOFs).[2,3] Among porous materials, MOFs seem to be the most encouraging.

More than 90,000 MOFs have been synthesized, and more than 500,000 structures

*Corresponding author.
Email: nguyenthixuanhuynh@qnu.edu.vn

https://doi.org/10.52111/qnjs.2021.15501

have been predicted up to now.[4] Nevertheless, very few MOFs have been evaluated and analyzed for storage, capture, separation, and other applications. Among MOFs, Ni(BDC)$(TED)_{0.5}$ structure, in which the metal component is Ni^{2+} (nickel ion), and the organic linkers are H_2BDC = 1,4-benzene-dicarboxylate (C_4H_6-1,4-$(CO_2H)_2$, TED = triethylenediamine ($C_6H_{12}N_2$), has been noted for CO_2 and SO_2 captures. By both experiment and computation, K. Tan et al. showed that Ni(BDC)$(TED)_{0.5}$ had higher SO_2 adsorption than M(BDC)$(TED)_{0.5}$ (M = Zn, Mg) and many other MOF structures.[5] However, this research was only performed in the pressure range below 2 bar. For CO_2, Arstad and co-workers also showed, at the room temperature, Ni(BDC)$(TED)_{0.5}$ adsorbed 14 wt% at the atmosphere pressure and up to at 25 atm.[6]

For comparing the experiment data and extending the uptake in the pressure range up to 50 bar, we performed grand canonical Monte Carlo (GCMC) simulations. The obtained results evaluate and explain the capture of CO_2 and SO_2 in Ni(BDC)$(TED)_{0.5}$ at 298 K and the pressures under 50 bar in detail.

2. GRAND CANONICAL MONTE CARLO METHOD

GCMC method[7] was employed to quantitatively assess CO_2 and SO_2 uptakes on the surface of the Ni(BDC)$(TED)_{0.5}$ MOF. The interactions between gases (CO_2, SO_2) and the MOF are the pairing interaction between the atoms *i* and *j* at a distance r_{ij}, described by:

$$U(r_{ij}) = k\frac{q_i q_j}{r_{ij}} + 4\varepsilon_{ij}\left[\left(\frac{\sigma_{ij}}{r_{ij}}\right)^{12} - \left(\frac{\sigma_{ij}}{r_{ij}}\right)^{6}\right] \quad (1)$$

In Formula (1), the first term describes the electrostatic (Coulomb) interactions between the pairs of atoms *i* and *j*, where $k = \frac{1}{4\pi\varepsilon_0}$ is the Coulomb constant (ε_0 is the electric constant), q_i is the i^{th} atomic charge in Ni(BDC)$(TED)_{0.5}$, including nickel (Ni), nitrogen (N), oxygen (O), carbon (C), and hydrogen (H). These partial charge parameters were calculated using DDEC (Density Derived Electrostatic and Chemical) algorithm to set the force field for electrostatic interactions. Besides, these interactions were handled using the Ewald summation technique[8] with the cut-off radius of 12 Å. The remaining term in Formula (1) describes the van der Waals interactions with an Lennard-Jones (LJ) potential, 6-12 potential. Here, ε_{ij}, σ_{ij} correspond to the depth and diameter of the potential well for each pair of atoms *i* and *j*, handled using Lorentz–Berthelot rule:

$$\varepsilon_{ij} = \sqrt{\varepsilon_i \varepsilon_j};\ \sigma_{ij} = \frac{1}{2}(\sigma_i + \sigma_j), \quad (2)$$

where σ_i, ε_i (*i* represents Ni, N, O, C, H of Ni(BDC)$(TED)_{0.5}$) were taken from general force fields for MOF in RASPA sofware[7] (Table 1). A cut-off radius of 14 Å was utilized for the LJ interactions. This factor affects calculation results, therefore it was checked carefully and showed in the results and discussion section. The calculation used the TraPPE force field for CO_2 molecule[9] with a linear three-point model with bonding length d_{C-O} = 1.16 Å ; whereas, SO_2 was modeled as the three-point model[10] with $d_{S-O} = 1.43$ Å, $\angle_{O-S-O} = 119.5°$. The force field parameters of CO_2 and SO_2 are also listed in Table 1.

Our calculations used the μVT set, where volume V, temperature T and chemical potential μ were constant in the simulation process. The room temperature (298 K) and pressures up to 50 bar were selected. The optimized primary unit cell of Ni(BDC)$(TED)_{0.5}$ has 22 C, 20 H, 8 O, 2 N, 2 Ni (54 atoms). In GCMC, the simulation box was kept fixed, while adsorbate molecules were moved randomly to reach equilibrium adsorption. Each calculated point ran 10^4 equilibration cycles and followed by 2×10^5 MC cycles. These parameters were checked carefully for their equilibrium.

https://doi.org/10.52111/qnjs.2021.15501

Table 1. LJ parameters of the atoms in $Ni(BDC)(TED)_{0.5}$

Atoms	ε/k_B [K]	σ [Å]	q [e]
Ni (MOF)	7.55	2.52	0.660
N (MOF)	38.95	3.26	-0.118
O (MOF)	48.16	3.03	-0.528
C (on BDC)	47.86	3.47	-0.067
C (BDC-TED)			-0.079
C (on TED)			-0.025
C (bonded with O)			0.636
H (on BDC)	7.65	2.85	0.093
H (on TED)			0.071
C (CO_2)	27.00	2.80	+0.700
O (CO_2)	79.00	3.05	- 0.350
S (SO_2)	145.90	3.62	0.471
O (SO_2)	57.40	3.01	-0.236

Note that for calculating gas adsorption in MOF, measured experimental data are usually the excess adsorption amount (N_{ex}). Simulations usually calculate the total adsorption amount or the absolute amount of gas adsorbed (N_{ab}). The expression describing the relationship between them is

$$N_{ab} = N_{\text{ex}} + \rho V_{\text{p}}, \quad (3)$$

In which, V_{p} is the pore volume and ρ is the density of gas (CO_2, SO_2) in the bulk phase.

3. RESULTS AND DISCUSSION

3.1. Optimizing and selecting the simulation box for $Ni(BDC)(TED)_{0.5}$

$Ni(BDC)(TED)_{0.5}$ has tetragonal structure symmetry with the lattice constants $a = b$ and the angles $\alpha = \beta = \gamma = 90^o$ (Figure 1). In $Ni(BDC)(TED)_{0.5}$, the metal-oxide-carbon (Ni-O-C) clusters link to BDC and TED ligands. Herein, BDC and TED stand for 1,4-benzene dicarboxylate and triethylenediamine. Stability and high porosity of the paddle-wheel units in the heat are the noticed characteristics to improve the amount of gas adsorbed.[11]

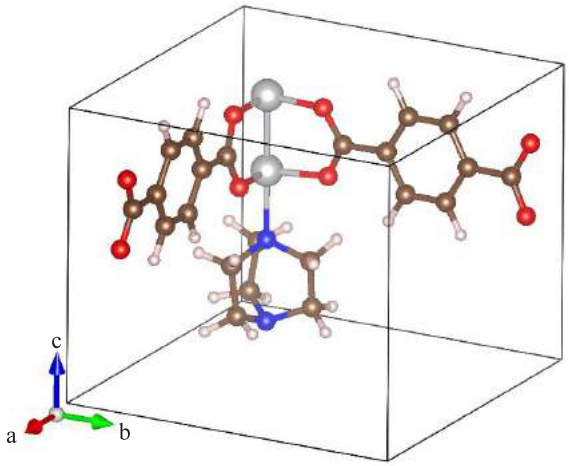

Figure 1. The primary unit cell of $Ni(BDC)(TED)_{0.5}$, herein the atoms Ni, N, O, C, and H correspond to light gray, blue, red, brown, and light pink balls.

After designing and optimizing the unit cell, all the atomic positions in the structure were relaxed to meet the equilibrium state based on the density functional theory with van der Waals (vdW-DF) correction.[12] The obtained results are $a = b = 11.98$ Å and $c = 9.38$ Å, leading to the volume of the unit cell is 1131 Å.[3] The simulated results are entirely close to the experiment data of Tan's group,[5] $a = b = 11.15$ Å and $c = 9.53$ Å. The lengths of the simulation box were repeated three times (≥ 28 Å) to perform GCMC simulations with high accuracy, as shown in Figure 2.

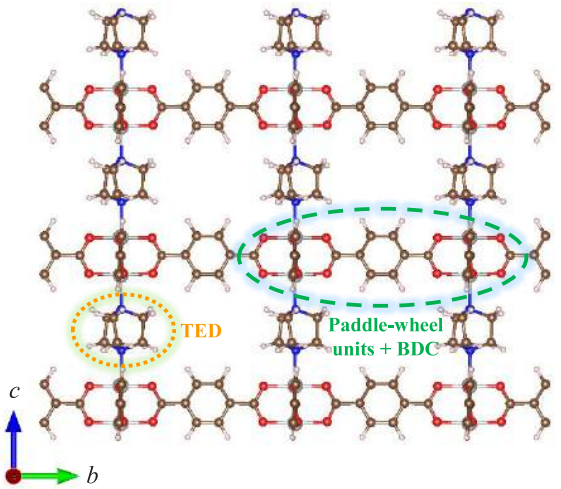

Figure 2. The 2D box of GCMC simulation (viewed along a axis). Two paddle-wheel units and one BDC ligand are in the blue curve; the TED unit is in the orange curve.

https://doi.org/10.52111/qnjs.2021.15501

3.2. The cut-off radius for Lennard–Jones interactions

The cut-off radius for electrostatic interactions was taken by default as 12 Å in the code because it has little impact on the amount of gas adsorbed to the MOF. In this section, the cut-off radius for the LJ interactions was regarded.

Based on the amount of gas adsorption in the MOF versus the LJ cut-off radius (r_c) at 1 bar, 5 bar and 10 bar (Figure 3), the value 14 Å was determined. Increasing r_c can improve accuracy, but it is insignificant and takes a long time for calculations. Therefore, we selected the value of approximately 14 Å with the unit cell repeating up 3 x 3 x 3 (*i.e.* 27 times) the unit cell in Figure 2. Furthermore, we also carefully checked the convergence of equilibration and MC cycles. The results achieved 10^4 equilibration cycles and 2 x 10^5 MC cycles.

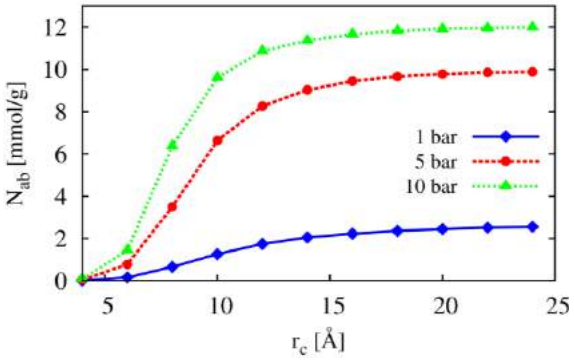

Figure 3. The selected LJ cut-off radius based on CO_2 adsorption in Ni(BDC)(TED)$_{0.5}$.

3.3. Investigation of structural features of Ni(BDC)(TED)$_{0.5}$

After relaxing the ions in the structure and selecting suitable parameters, we also calculated the specific surface area (SSA) and pore volume (V_p) of Ni(BDC)(TED)$_{0.5}$, essential features of porous crystalline frameworks affecting gas capture. The parameters SSA and V_p were determined by calculating the adsorption amount of nitrogen (N_2) at 77 K. This calculation proved to be relatively consistent with the Brunauer-Emmett-Teller (BET) method.[13]

The simulation results are and SSA = 1686 m^2/g and V_p = 0.76 cm^3/g, in good agreement with previous measurement results of experimental groups with specific surface areas corresponding to 1763 m^2/g[11] and 1698 m^2/g.[14] The achievements also show that although the SSA is smaller than the experimental data of X. Fan with 1905 m^2/g for Ni(BDC)(TED)$_{0.5}$, it closely resembles the remaining structural series M(BDC)(TED)$_{0.5}$ (M = Zn, Co, Cu).[15] Besides, the computed results also show that the pore volume of the MOF (0.76 cm^3/g) is entirely suitable with the obtained experimental data of 0.757 cm^3/g.[15] Again, it is proved that our calculations are very reliable.

3.4. Evaluation of the gas capture capacities

Firstly, we selected and tested the force field models before performing the calculations. The amount of gas adsorption corresponding to two force field models for CO_2 molecules, TraPPE[9] and EMP2,[16] are similar at 298 K and under 1 bar (Figure 4). The obtained results are N_{ab} = 2.30 mmol/g (*i.e.* 10.13 wt%) and N_{ex} = 2.27 mmol/g (10 wt%) at room temperature and standard atmospheric pressure. These values are also relatively close to the experimental data of Arstad et al. with 14 wt% under the same conditions.[6]

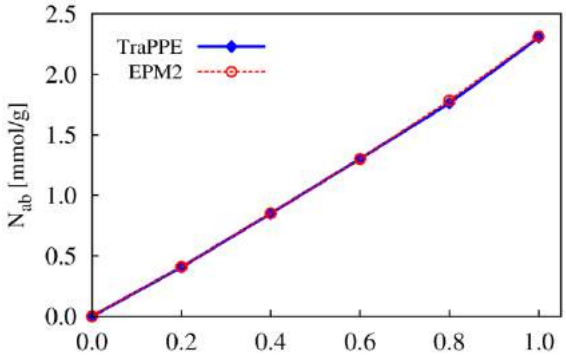

Figure 4. The CO_2 adsorption of Ni(BDC)(TED)$_{0.5}$ using TraPPE and EMP2 force fields.

Two force field models give the same results, so we use the TraPPE model for CO_2 in this work. The gas sorption amounts in Ni(BDC)(TED)$_{0.5}$ with various pressure points up to 50 bar were calculated, and then we plotted the adsorption isotherms for CO_2 and SO_2 at 298 K (Figure 5). At this temperature, CO_2 uptake in

https://doi.org/10.52111/qnjs.2021.15501

$Ni(BDC)(TED)_{0.5}$ results in N_{ab} = 13.53 mmol/g (59.53 wt%) and N_{ex} = 12.63 mmol/g (59.56 wt%) at 25 bar. Under the conditions above, Arstad et al.[6] experimentally measured N_{ex} = 60 wt%). Furthermore, at 30 bar, our evaluated excess uptake is approximately 12.7 mmol/g. In this same condition, Chen and coworkers computed N_{ex} = 13.6 mmol/g (*i.e.* 600 mg/g or 60 wt%) for $Zn(BDC)(TED)_{0.5}$,[17] listed in Table 2. In this publication, the highest amount of CO_2 capture in $Ni(BDC)(TED)_{0.5}$ was achieved at the value of 14.40 mmol/g (63,37 wt%) at 50 bar. This value is also remarkable compared to other MOFs evaluated for CO_2 adsorption.[18]

For SO_2, Figure 5 determines that adsorption-based SO_2 capture in $Ni(BDC)(TED)_{0.5}$ rapidly increases at low pressures under 5 bar. The adsorbed gas amount saturate at about 5 bar corresponding to N_{ab} = 13.6 mmol/g. Greater than 5 bar, the adsorbed amount insignificantly increase with increasing pressure to 50 bar (only 0.1 mmol/g achieved in this pressure range). At about 1 bar, our simulation indicated that the amount of gas adsorbed is 12 mmol/g, slightly higher than that of the K. Tan group with 10 mmol/g.[5]

Table 2. Absolute (total) and excess uptakes of CO_2 in $Ni(BDC)(TED)_{0.5}$, compared to other MOFs.

Uptakes	Pressure [bar]		
	1	25	30
N_{ab} (N_{ex}) [mmol/g]	2.30 (2.27)	13.53 (12.63)	13.81 (12.68)
N_{ab} (N_{ex}) [wt%]	10.14 (10.00)	59.53 (55.56)	60.76 (55.80)
$Ni(BDC)(TED)_{0.5}$[6] [wt%]	14	60	
$Zn(BDC)(TED)_{0.5}$[17] [mmol/g]			13.6

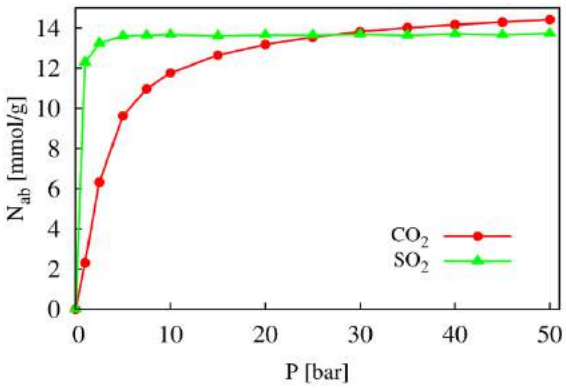

Figure 5. The CO_2 and SO_2 adsorption isotherms in $Ni(BDC)(TED)_{0.5}$ at T = 298 K and P ≤ 50 bar.

Our results also show that SO_2 adsorbs much more powerfully than CO_2 in the low-pressure region below 25 bar. Remarkably, the amount of SO_2 saturates while the CO_2 adsorption continues to increase at higher pressures. Therefore, at 50 bar, it results in N_{ab} CO_2 = 14.4 mmol/g, slightly larger than that of SO_2 with 14.4 mmol/g.

The gas adsorption (the linear 3-atom model) and SO_2 (the 3-atom model with the 119.5^O angle) were also visualized via Figure 6 and Figure 7, respectively. Visualization of gases shows that there is slightly more SO_2 than CO_2 in $Ni(BDC)(TED)_{0.5}$ at identical conditions. Significantly, the amount of SO_2 enormously increases compared to CO_2 according to the pressure up to 5 bar.

We also know the isosteric heat of adsorption (Q_{st}) is also an important parameter relating to gas adsorption. The results, calculated at low-pressures up to 1000 Pa (Figure 8), exhibit the average adsorption heats of SO_2 and CO_2 on $Ni(BDC)(TED)_{0.5}$ with respect to 32.7 kJ/mol and 17.3 kJ/mol. These values also elucidate that this MOF captures SO_2 more highly than CO_2 in the low-pressure region. This tendency is also consistent with the results of D. N. Son et al. with the prediction of adsorption capacities of CO_2 and SO_2 by adsorption energy based on density functional theory.[19] Herein, their work showed that, when studying the simultaneous adsorption of two gases, $Ni(BDC)(TED)_{0.5}$ strongly adsorbs

https://doi.org/10.52111/qnjs.2021.15501

SO_2 than CO_2 due to the primary interactions between the *d*-orbitals of Ni metal with the states (*2n, 3n, 4n*) of the SO_2 molecule but barely interacting with those of the CO_2 molecule.

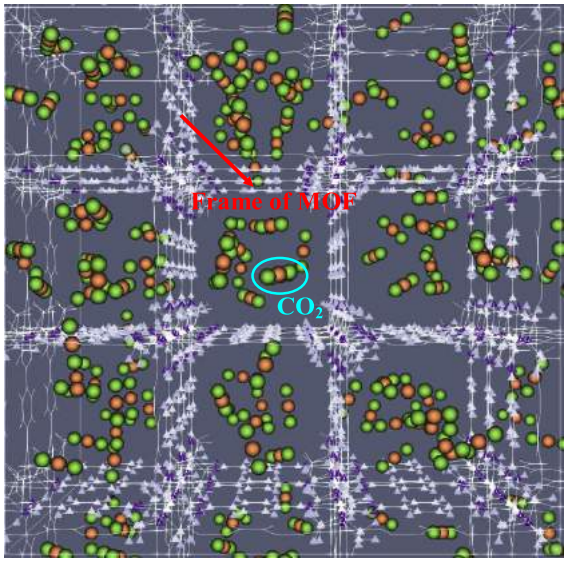

Figure 6. Visualization of CO_2 adsorption in Ni(BDC)$(TED)_{0.5}$ at 0.1 bar and 298 K, herein C and O atoms of CO_2 correspond to dark-orange and light-green balls.

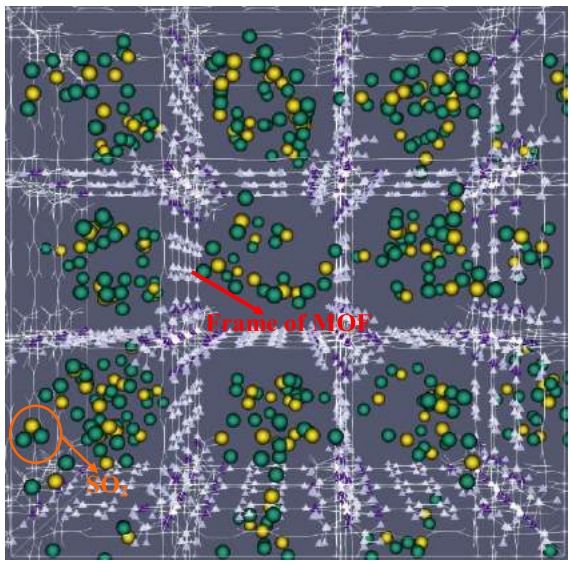

Figure 7. Visualization of SO_2 adsorption in Ni(BDC)$(TED)_{0.5}$ at 0.1 bar and 298 K, in which S and O atoms of SO_2 correspond to yellow and green balls.

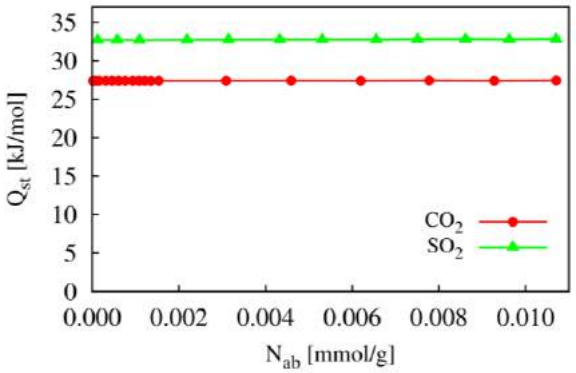

Figure 8. Heat of adsorption (Q_{st}) for CO_2 and SO_2 on Ni(BDC)$(TED)_{0.5}$ at 298 K.

4. CONCLUSIONS

In our research, the cut-off radius for the LJ potential with 14 Å is suitable for GCMC simulations to evaluate CO_2 and SO_2 capture capacities in Ni(BDC)$(TED)_{0.5}$. This value is an important parameter affecting the gas amount adsorbed in the Ni(BDC)$(TED)_{0.5}$ MOF.

Our calculations show that, at low pressures below 25 bar, the capture capacity of SO_2 is more robust than that of CO_2 in Ni(BDC)$(TED)_{0.5}$. Until the pressure exceeds 25 bar, only CO_2 uptake increases slightly while SO_2 uptake saturates. The calculated results are significant with 14.4 mmol/g for CO_2 capture at 50 bar and 13.6 mmol/g for SO_2 at 5 bar.

The heat of gas adsorption on Ni(BDC)$(TED)_{0.5}$ corresponding to the values 32.7 kJ/mol and 17.3 kJ/mol for SO_2 and CO_2 also shows that the SO_2 adsorbs more strongly than CO_2 in the MOF above in the low-pressure range.

Acknowledgment

This study is conducted within the framework of student scientific research projects at the institutional level of Quy Nhon University under the project code S2020.645.09.

REFERENCES

1. H. C. Zhou, J. R. Long, and O. M. Yaghi. Introduction to metal-organic frameworks, *Chemical Reviews*, **2012**, *112*, 673–674.

2. X. Peng, S. K. Jain, and J. K. Singh. Adsorption and separation of $N_2/CH_4/CO_2/SO_2$ gases in disordered carbons obtained using hybrid reverse Monte Carlo simulations, *The Journal of Physical Chemistry C,* **2017**, *121*, 13457–13473.

3. R. Sabouni, H. Kazemian, and S. Rohani. Carbon dioxide capturing technologies: A review focusing on metal organic framework materials (MOFs), *Environmental Science and Pollution Research*, **2014**, *21*, 5427–5449.

4. S. M. Moosavi et al. Understanding the diversity of the metal-organic framework ecosystem, *Nature Communications*, **2020,** *11*, 1–10.

5. K. Tan et al. Mechanism of preferential adsorption of SO_2 into two microporous paddle wheel frameworks $M(bdc)(ted)_{0.5}$, *Chemistry of Materials*, **2013**, *25*, 4653–4662.

6. B. Arstad, H. Fjellvåg, K. O. Kongshaug, O. Swang, and R. Blom. Amine functionalised metal organic frameworks (MOFs) as adsorbents for carbon dioxide, *Adsorption*, **2008**, *14*, 755–762.

7. D. Dubbeldam, S. Calero, D. E. Ellis, and R. Q. Snurr. RASPA: molecular simulation software for adsorption and diffusion in flexible nanoporous materials, *Molecular Simulation*, **2016**, *42*, 81–101.

8. M. P. Allen and D. J. Tildesley. *Computer simulation of liquids*, 2nd edition, Oxford University Press, Oxford-United Kingdom, 2017.

9. J. J. Potoff and J. I. Siepmann. Vapor-liquid equilibria of mixtures containing alkanes, carbon dioxide, and nitrogen, *AIChE Journal*, **2001**, *47*, 1676–1682.

10. F. Sokolić, Y. Guissani, and B. Guillot. Molecular dynamics simulations of thermodynamic and structural properties of liquid SO_2, *Molecular Physics*, **1985**, *56*, 239–253.

11. L. Peng et al. Application of metal organic frameworks $M(bdc)(ted)_{0.5}$ (M = Co, Zn, Ni, Cu) in the oxidation of benzyl alcohol, *RSC Advances*, **2016**, *6*, 72433–72438.

12. M. Dion, H. Rydberg, E. Schröder, D. C. Langreth, and B. I. Lundqvist. Van der Waals density functional for general geometries, *Physical Review Letters*, **2004**, *92*, 246401-1–246401-4.

13. K. S. Walton and R. Q. Snurr. Applicability of the BET method for determining surface areas of microporous metal-organic frameworks, *Journal of the American Chemical Society*, **2007**, *129*, 8552–8556.

14. R. Fu, A. J. Hern, and S. P. Hern. Long and local range structural changes in $M[(bdc)(ted)_{0.5}]$ (M = Zn, Ni or Cu) metal organic frameworks upon spontaneous thermal dispersion of LiCl and adsorption of carbon dioxide, *Microporous and Mesoporous Materials,* **2015**, *212*, 8–17.

15. H. Xiang *et al.* Selective adsorption of ethane over ethylene on $M(bdc)(ted)_{0.5}$ (M = Co, Cu, Ni, Zn) metal-organic frameworks (MOFs), *Microporous and Mesoporous Materials*, **2020**, *292*, 109724-1–109724-12.

16. J. G. Harris and K. H. Yungt. Carbon dioxide's liquid-vapor coexistence curve and critical properties as predicted by a simple molecular model, *The Journal of Physical Chemistry*, **1995**, *99*, 12021–12024.

17. Y. F. Chen, J. Y. Lee, R. Babarao, J. Li, and J. W. Jiang. A highly hydrophobic metal-organic framework $Zn(BDC)(TED)_{0.5}$ for adsorption and separation of CH_3OH/H_2O and CO_2/CH_4: An integrated experimental and simulation study, *The Journal of Physical Chemistry C*, **2010**, *114*, 6602–6609.

18. K. Sumida et al. Carbon dioxide capture in metal–organic frameworks, *Chemical Reviews*, **2012** *112*, 724–781.

19. D. N. Son, T. T. T. Huong, and V. Chihaia. Simultaneous adsorption of SO_2 and CO_2 in an $Ni(bdc)(ted)_{0.5}$ metal–organic framework, *RSC Advances*, **2018**, *8*, 38648–38655.

https://doi.org/10.52111/qnjs.2021.15501

TẠP CHÍ KHOA HỌC
TRƯỜNG ĐẠI HỌC QUY NHƠN

Ứng dụng Raspberry và PLC Mitsubishi trong thiết kế hệ thống tự động phân loại cà chua

Bùi Văn Vũ[1,*], Nguyễn Đức Thịnh[2], Phạm Thanh Bình[2], Đỗ Văn Cần[1]

[1]Giảng viên Khoa Kỹ thuật và Công nghệ, Trường Đại học Quy Nhơn, Việt Nam
[2]Sinh viên ngành Kỹ thuật điện - Điện tử, Khoa Kỹ thuật và Công nghệ, Trường Đại học Quy Nhơn, Việt Nam

Ngày nhận bài: 05/05/2021; Ngày nhận đăng: 18/08/2021

TÓM TẮT

Bài viết này trình bày về việc ứng dụng Raspberry và PLC Mitsubishi để thiết kế hệ thống tự động phân loại cà chua. Trong bài báo này, thuật toán KNN (K-Nearest Neighbors) và thuật toán xác định màu sắc quả được sử dụng để phân loại cà chua theo mức độ chín, hình dạng và kích thước. Các thuật toán này được nhúng vào Raspberry để xử lý hình ảnh. Sau khi xử lý, các tín hiệu điện từ Raspberry được truyền đến PLC Mitsubishi để điều khiển các cơ cấu phân loại của hệ thống. Thêm vào đó, tác giả cũng xây dựng hệ thống SCADA (Supervisory, Control and Data Acquisition) để điều khiển, giám sát và thu thập dữ liệu của hệ thống phân loại. Các kết quả thu được từ thực nghiệm cho thấy hệ thống phân loại cà chua hoạt động ổn định, độ chính xác khá cao và năng suất lao động cao.

Từ khóa: *PLC, SCADA, cà chua, hình dạng, thuật toán KNN.*

**Tác giả liên hệ chính.*
Email: bvvu@ftt.edu.vn

JOURNAL OF SCIENCE
QUY NHON UNIVERSITY

Application of Raspberry and PLC Mitsubishi to the design of tomato classified system automatically

Bui Van Vu[1,*], Nguyen Duc Thinh[2], Pham Thanh Binh[2], Do Van Can[1]

[1]Lecturer, Faculty of Technology and Engineering, Quy Nhon University, Vietnam
[2]Electrical student, Faculty of Technology and Engineering, Quy Nhon University, Vietnam

Received: 05/05/2021; Accepted: 18/08/2021

ABSTRACT

This article illustrates the application of Raspberry and PLC Mitsubishi to the design of a tomato classifying system automatically. In this paper, the KNN (K-Nearest Neighbors) algorithm is used in conjunction with the fruit color determination algorithm to determine the level of ripeness, shape and size of tomatoes. These algorithms are embedded into the Raspberry to perform image processing. After processing, the electrical signals from the Raspberry are transmitted to the PLC Mitsubishi to control the actuators of the sorting system. In addition, the authors also establish a SCADA (Supervisory, Control And Data Acquisition) system to control, monitor and collect data of the classification system. The experimental results point out that the tomato grading system is stable, with relatively high accuracy and high labor productivity.

Keywords: *PLC, SCADA, tomato, shape, KNN algorithm.*

1. INTRODUCTION

In Vietnam, agricultural products after harvest are often not classified or visually classified, leading to low productivity, high labor costs and low accuracy. This issue greatly affects the competitiveness of Vietnamese agricultural products with other countries in the world.

Along with agricultural production in accordance with VietGAP and GlobalGAP standards, the classification and packaging of products that meet export criteria is also one of the important factors to help improve the competitiveness of Vietnamese agricultural products. In recent years, there have been several great developments in the field of science and engineering such as robotics,[1-3] artificial intelligence (AI)[4,5] and machine learning.[3,6] We can make use of these achievements of science and technology to build labor-saving, high-precision, high-productivity agricultural product sorting systems.

Our country has many types of agricultural products that need to be classified and packaged for export such as tomatoes, mangoes, green-skinned pomelos, litchi, dragon fruit, etc. In this article, agricultural products need to be classified as tomatoes after is harvested. The classification criteria are the degree of ripeness of the fruit, the size of the fruit and the shape of the fruit.

Today, there have been many studies on the use of image processing technology to classify tomato products after harvest, but most of them only study the classification of tomatoes based on one or a few classification criteria

**Corresponding author.*
Email: bvvu@ftt.edu.vn

https://doi.org/10.52111/qnjs.2021.15502

such as classification of tomatoes based on fruit color,[7,8] classification based on fruit shape criterion,[9] or classification of fruit based on 2 criteria of shape and color[10] without giving a complete classification system. This paper applies and updates existing scientific achievements in desig-ning an automatic tomato sorting system based on all 3 criteria of fruit shape, fruit size and fruit ripeness in order to replace for manual classifica-tion in Vietnam.

In this paper, image processing techniques are embedded in Raspberry for image processing. The color identification algorithm[13,14] would be used in combination with the K-Nearest Neighbors (K-Nearest Neighbors) algorithm[6,11,12] to classify tomatoes according to the following criteria: fruit ripeness, size fruit and fruit shape (fruit distortion). Then, the processing signals from the Raspberry are transmitted to the PLC (Programmable Logic Controller) to perform the classification stage. Contents related to the design of the control, monitoring and data acquisition (SCADA) system of the classification are also presented in the paper.

KNN algorithm is an algorithm used in machine learning.[3,6] Despite a simple algorithm, it has a relatively high accuracy[15] and a fast processing time.[6] These characteristics allow it to be embedded in an embedded computer (Raspberry) easily.

The image processing signals from the Raspberry would be transmitted to the Mitsubishi PLC (FX2N 128MR), and then the PLC controls the actuators to perform the classification. Besides, aiming to build a convenient, intuitive and modern classification system, the authors also built a control, monitoring and data acquisition system (SCADA) for the classification system.

2. CLASSIFICATION PROCESS

2.1. Classification algorithm

2.1.1. Determining fruit shape and size

In image processing techniques, there are many algorithms to determine shape and size in tomato classification such as: KNN,[6,11,12] Naive Bayes,[12] SVM,[6,11] etc. KNN has the advantages such as fast processing time, simple algorithm easily embedded in the Raspberry embedded computer and highly accurate, therefore, this algorithm is chosen to determine the shape and size of the fruit in this paper.

The KNN algorithm consists of two stages: the training phase and the classification phase.[16] In the training phase, the training samples are vectors (each vector has a label). In this stage, the feature vectors and labels of the training samples are stored. In the classification phase, the input query point or feature vector is compared with the reference vector library, and the query point is labeled.

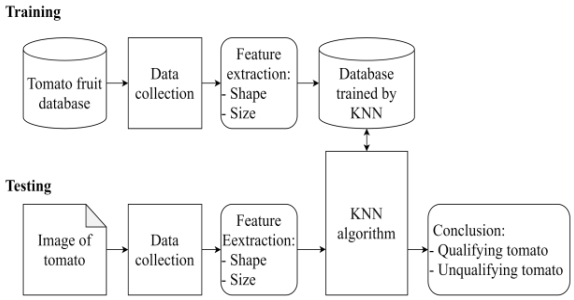

Figure 1. KNN algorithm

The process of classifying tomato shape and size is shown in Figure 1. The first step is to create a data library. This gallery includes images of 2500 tomatoes selected based on fruit shape and size characteristics. These samples are then labeled and put into a classification system for identification. Then the constant K is determined. K is the number of sample data points with the closest distance (nearest neighbor) to the data point of the unclassified tomato. The empirical method is used to determine the coefficient K in the KNN algorithm. Specifically, 300 tomato sample data were included in the identification, showing that when K > 5, the accuracy of the classification system does not seem to change, but the time to classify a tomato product increases proportionally to the magnitude of K. This means the system's productivity would decrease as K is larger. Therefore, K = 5 is chosen.

The distance between feature vectors of the object to be classified with all training data is determined by Euclidean formula.[17] Suppose that we have two given data matrices with 1 row and n columns as follows: $X = [x_1, x_2,\ldots, x_n]$ and $Y = [y_1, y_2,\ldots, y_n]$ then the distance between the vectors x and y is calculated as Euclidean formula (1).

$$d = \sqrt{\sum_{i=1}^{n}(x_i - y_i)^2} \quad (1)$$

Then, this calculation result is sorted in ascending order and the K closest neighbors to the data of the tomato to be classified are determined and finally concluded.

2.1.2. Determining the color of the fruit

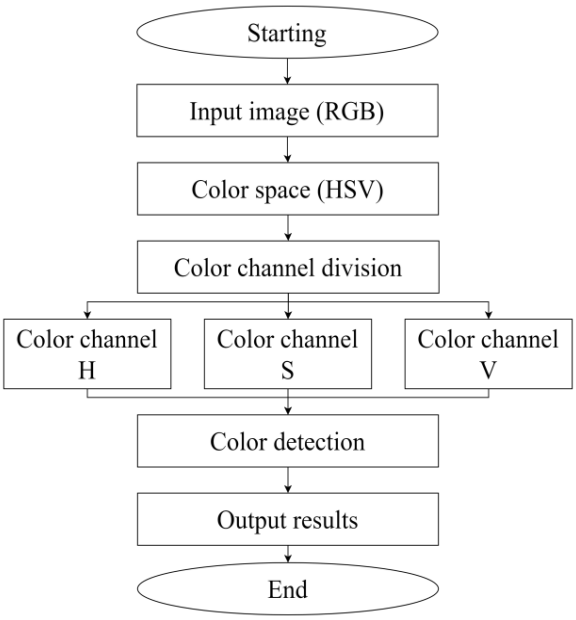

Figure 2. Algorithm to detect color (ripeness) of fruit.

The process of detecting the color (ripeness) of the fruit is shown in Figure 2.

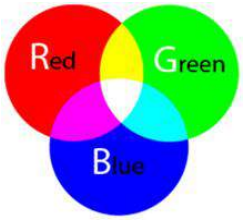

Figure 3. RGB color space.

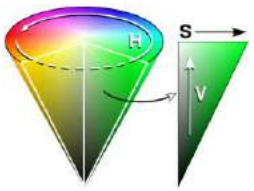

Figure 4. HSV color space.

The process of detecting the color (ripeness) of the fruit is shown in Figure 2.

To determine the color (ripeness) of the tomato, the system relies on images taken from the camera. At this point, the tomato image belonging to the RGB color space (Figure 3) would be converted to the HSV color space (Figure 4).

To convert from RGB color space to HSV color space, formula 2 [18,19,20] is used.

$$\begin{cases} H = \arccos\left(\dfrac{\frac{1}{2}(2R - G - B)}{\sqrt{(R-G)^2 - (R-G)(G-B)}}\right) \\ S = \dfrac{\max(R,B,G) - \min(R,B,G)}{\max(R,B,G)} \\ V = \dfrac{\max(R,B,G)}{255} \end{cases} \quad (2)$$

Once the value of the color channels is calculated, the number of pixels in the tomato image to be classified, the number of pixels of white and the number of pixels of black are determined. Based on that, the degree of ripeness of the fruit is found.

2.2. Building experimental system

Figure 5 is a general block diagram of the classification system. The equipment used in the experimental model is shown in Figure 6. In it, the camera block is used to collect and transmit image data of the tomato to the Raspberry. The sensor block is used to send an electrical signal to the Raspberry when the tomato reaches the camera position. The processing block consists of Raspberry and PLC (Programmable Logic Controller). In it, Raspberry receives image data from the camera, executes image processing, and sends the processing results in the form of electrical signals to the PLC so that the PLC controls the actuators (motors, pneumatic cylinders,…). The display block is used to display the results of tomato image processing.

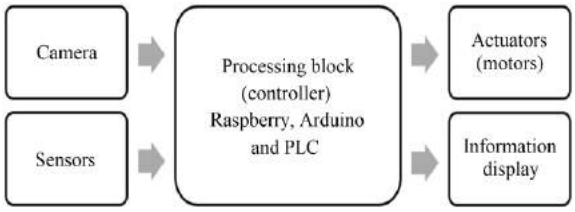

Figure 5. Image of blocks in the classification system.

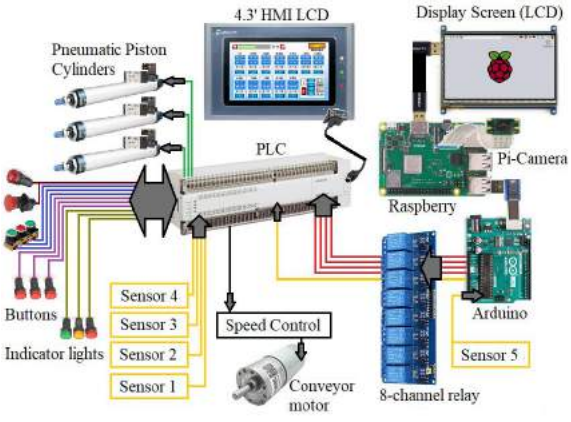

Figure 6. Images of devices in the experimental model.

The working process of the classification system is shown in Figure 7.

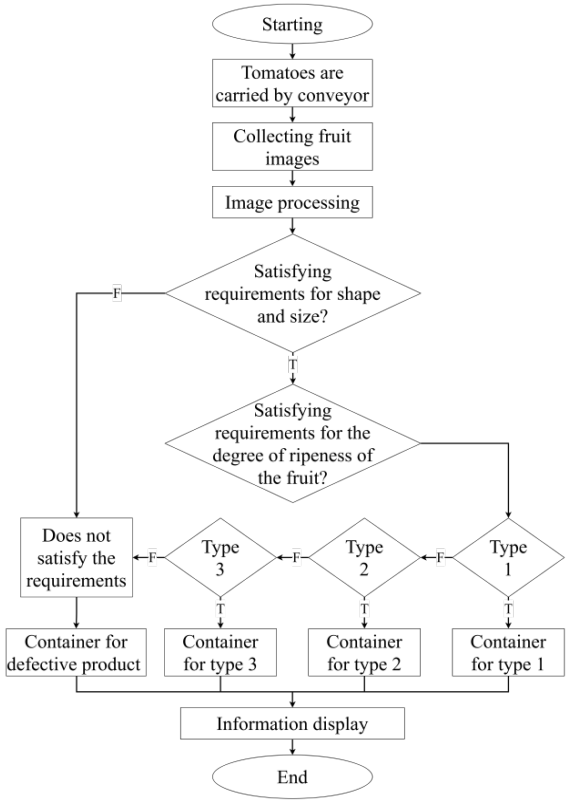

Figure 7. The working process of the classification system.

Figure 8. Experimental model of the classification system.

Figure 8 is an experimental model image of the automatic tomato classifying system.

The operating process of the system is as follows: When starting the system, the cylinder pushes the tomatoes into the conveyor, the tomatoes would be brought to the camera position. When the sensor detects the fruit has reached the camera position, a picture of the tomato is taken. Raspberry would take the image signal of the object and process the image.

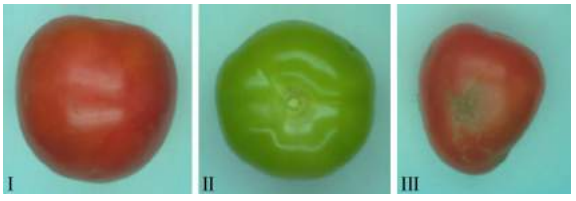

Figure 9. The images collected from the camera.

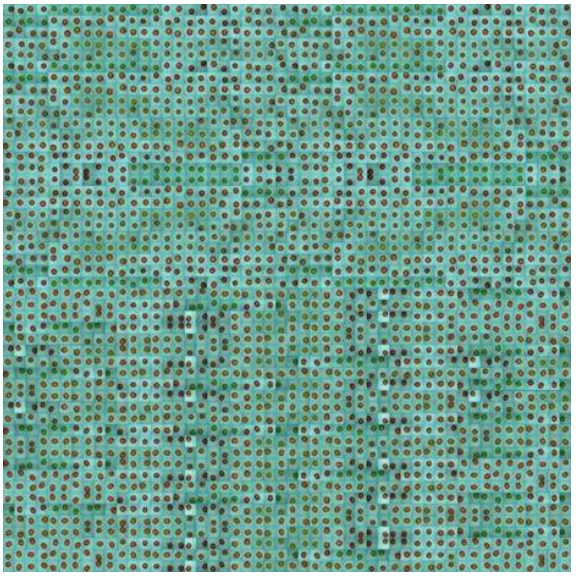

Figure 10. Sample database

The shape and size of the tomatoes that need to be classified were compared with a library of 2500 sample tomatoes for classification. A library of 2500 sample tomatoes is shown in Figure 10.

Figure 11 shows the result of the tomato sorting process displayed on the system notification screen. As seen, the images of fruit I and fruit II are satisfactory in terms of fruit size and fruit shape, while fruit III is unsatisfactory in shape (distorted fruit).

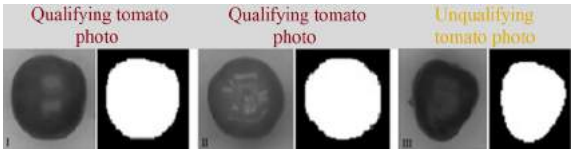

Figure 11. Classification results based on the criteria of fruit size and fruit shape (fruit distortion).

If any fruit does not meet the standard in shape and size, Raspberry would send a signal to PLC Mitsubishi to proceed to put the fruit into the container of the defective product.

The fruits that meet the standards in shape and size would be further classified by the system according to the degree of ripeness of the fruit based on the color classification algorithm mentioned in Subsection 2.1.2. Figure 12 is the result of the level of ripeness grading of the fruit displayed on the notification screen. For fruits with different degrees of ripeness, the PLC sends signals to the actuators to put them in the corresponding containers. Finally, the sorting results would be displayed on the LCD screen for the operator to easily monitor the sorting process. In this step, information about the ripeness, shape and size of the fruit (satisfy or not) is displayed on the screen (see Figure 13).

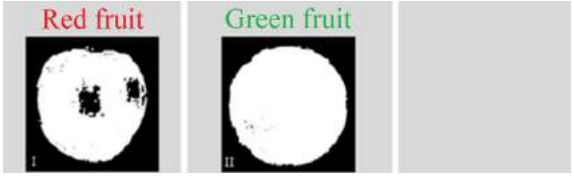

Figure 12. Classification of fruit ripeness.

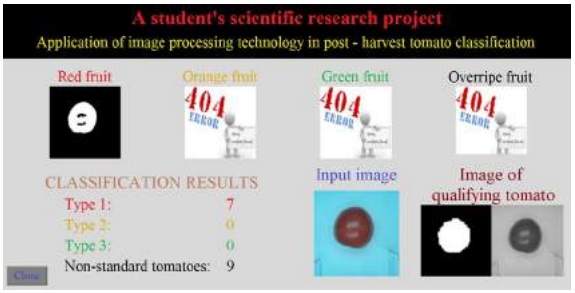

Figure 13. Screen showing classification result information.

SCADA system for automatic tomato sorting system was also built by the authors. The operator can control the system, monitor its operation and collect system data on the Samkoon HMI screen (see Figures 14 and 15). In which, Figure 14 is the system control interface.

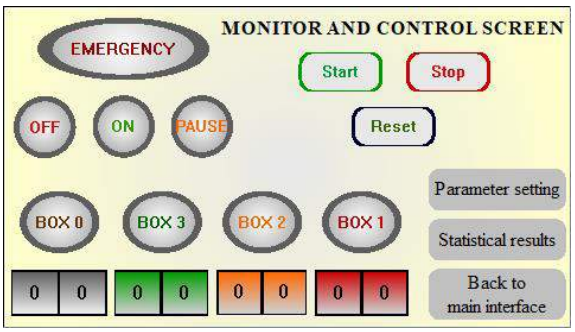

Figure 14. The HMI screen shows the monitoring – control interface of the classification system.

Figure 15 is the screen to monitor the number of tomatoes that meet the standards of classes I, II, III and those that do not meet the requirements.

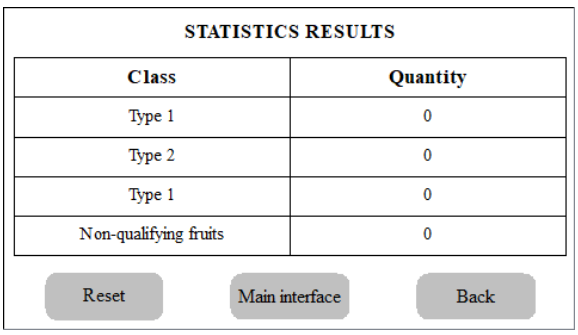

Figure 15. The screen monitoring the number of tomatoes that meet the standards of classes I, II, III and those that do not meet the requirements.

2.3. Experimental results

The author carried out the experimental process on 300 tomato samples. Figure 16 shows

https://doi.org/10.52111/qnjs.2021.15502

the accuracy of the system when classifying according to the standard of fruit distortion. Of the 300 tested fruits, 71.5% of the fruits did not meet the shape criterion, labeled as failing, and 28.5% of the fruits met the shape criterion, labeled as meeting the requirement. The result of the system's classification revealed that 69% of the tested fruits were unsatisfactory and 31% satisfactory. Therefore, the accuracy of the system in classification according to the criterion of shape (distortion) of fruit is 95.87%.

The process of evaluating the accuracy of the system according to the criteria of fruit size and fruit color was also done similarly. Figure 17 demonstrates the result of the system's classification according to fruit size criteria. The system could classify according to this criterion with an accuracy of 95.87%.

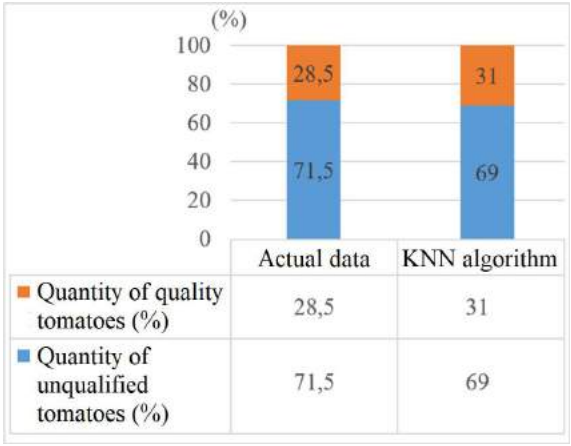

Figure 16. Classification results according to the criteria of fruit shape.

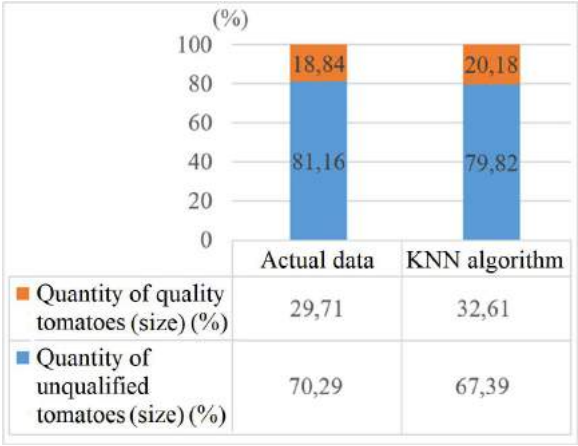

Figure 17. Results of classification according to fruit size criteria.

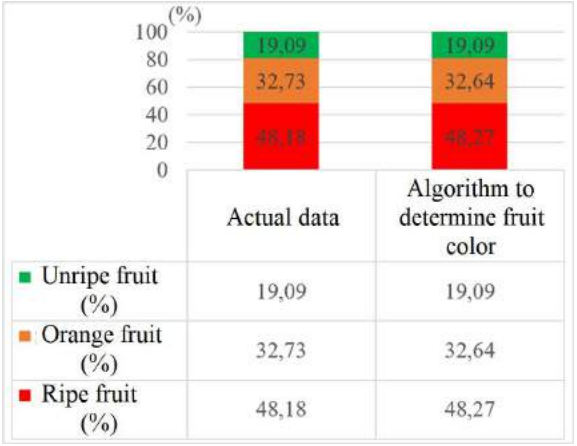

Figure 18. Classification results according to the degree of ripeness of the fruit (fruit color).

As can be seen from Figure 18 which shows the result of the system's classification according to fruit color criteria (ripeness), the system had an accuracy of approximately 99%.

The reason for errors in the product classification of the system is due to the resolution of the captured images and the location of the camera installation. When the shooting angle is different, it is more or less affects the results of the fruit's shape and size classification. The resolution of the image affects the fruit's ripeness classification results. The higher the resolution of the image, the better the accuracy of the classification process. However, too high image resolution affects the recognition speed and reduces the classification performance of the system.

Besides, the experimental results also show that the time to classify a tomato product from the time of image collection to the time when the classification process results are displayed was small, approximately 1.2 seconds.

3. CONCLUSION

In this paper, the author used Mitsubishi PLC (FX2N 128MR) and Raspberry embedded computer to design a tomato grading system. Besides, the author has also successfully design a monitoring, control and data collection system for an automatic tomato classification system. The experimental results show that the system had high stability and fast sorting speed (1.2 seconds for 1 tomato product). Experiment with 300 samples gave accurate results of 95.87% in

terms of shape and size standards and 99% in terms of maturity standards. This system can be applied in practice.

REFERENCES

1. M. Bergerman et al. Robot Farmers. Autonomous orchard vehicles help tree fruit production, *IEEE Robotics & Automation Magazine*, **2015**, *22*, 54-63.
2. D. Mengoli, R. Tazzari and L. Marconi. *Autonomous robotic platform for precision orchard management: Architecture and software perspective*, 2020 IEEE International Workshop on Metrology for Agriculture and Forestry (MetroAgriFor), Trento, Italy, 2020, 303-308.
3. M. Kulbacki et al. *Survey of drones for agriculture automation from planting to harvest*, 2018 IEEE 22nd International Conference on Intelligent Engineering Systems (INES), Las Palmas de Gran Canaria, Spain, 2018, 353-358.
4. W. Dong, T. Wu, Y. Sun and J. Luo. *Digital mapping of soil available phosphorus supported by AI technology for precision agriculture*, 2018 7th International Conference on Agro-geoinformatics (Agro-geoinformatics), Hangzhou, China, 2018, 1-5.
5. L. Deng. Artificial intelligence in the rising wave of deep learning: the historical path and future outlook [perspectives], *IEEE Signal Processing Magazine*, **2018**, *35*, 180-177.
6. I. A. Sabilla & C. Fatichah. The tomatoes and chilies type classifications by using machine learning methods, *Journal of Development Research*, **2020,** *4*(1), 1-6.
7. Villaseñor-Aguilar, M. J., Botello-Álvarez, J. E., Pérez-Pinal, F. J., Cano-Lara, M., León-Galván, M. F., Bravo-Sánchez, M. G., & Barranco-Gutierrez, A. I. Fuzzy classification of the maturity of the tomato using a vision system, *Journal of Sensors*, **2019**, 2019(1-12).
8. A. Taofik, N. Ismail, Y. A. Gerhana, K. Komarujaman & M. A. Ramdhani. *Design of smart system to detect ripeness of tomato and chili with new approach in data acquisition*, In IOP Conference Series: Materials Science and Engineering, IOP Publishing, 2018.
9. D. Ireri, E. Belal, C. Okinda, N. Makange & C. Ji. A computer vision system for defect discrimination and grading in tomatoes using machine learning and image processing, *Artificial Intelligence in Agriculture*, **2019**, *2*, 28-37.
10. M. Rokunuzzaman & H. P. W. Jayasuriya. Development of a low cost machine vision system for sorting of tomatoes, *Agricultural Engineering International: CIGR Journal*, **2013**, *15*(1), 173-180.
11. V. Pavithra, R. Pounroja and B. S. Bama. *Machine vision based automatic sorting of cherry tomatoes*, 2015 2nd International Conference on Electronics and Communication Systems (ICECS), Coimbatore, India, 2015, 271-275.
12. P. Boonyopakorn and P. Bualeard. *Applying neuro fuzzy system to analyze durian minerals within soil for precision agriculture*, 2020 17th International Conference on Electrical Engineering/Electronics, Computer, Telecommunications and Information Technology (ECTI-CON), Phuket, Thailand, 2020, 135-138.
13. T. Mehra, V. Kumar and P. Gupta. *Maturity and disease detection in tomato using computer vision*, 2016 Fourth International Conference on Parallel, Distributed and Grid Computing (PDGC), Waknaghat, India, 2016, 399-403.
14. R. R. Mhaski, P. B. Chopade and M. P. Dale. *Determination of ripeness and grading of tomato using image analysis on Raspberry Pi*, 2015 Communication, Control and Intelligent Systems (CCIS), Mathura, India, 2015, 214-220.
15. R. G. De Luna, E. P. Dadios, A. A. Bandala & R. R. P. Vicerra. Size classification of tomato fruit using thresholding, machine learning, and deep learning techniques, *Journal of Agricultural Science*, **2019,** *41*(3), 586-596.
16. TMin-Ling Zhang and Zhi-Hua Zhou. *A k-nearest neighbor based algorithm for multi-label classification*, 2005 IEEE International Conference on Granular Computing, 2005, 2, 718 - 721.
17. I. Saini, D. Singh & A. Khosla. QRS detection using K-Nearest Neighbor algorithm (KNN) and evaluation on standard ECG databases, *Journal of Advanced Research*, **2013,** *4*(4), 331-344.
18. L. Peng, H. Yong and Y. Kunlun. *Multi-algorithm fusion of RGB and HSV color spaces for image enhancement*, Proceedings of the International Conference on 37th Chinese Control Conference (CCC), China, 2018, 9584-9589.
19. K. N. Plantaniotis and A. N. Ventsanopoulos. *Color image processing and applications,* Springer, 2000.
20. Nguyen Truong Duy, Tran Dinh Huy Duc, Bui Van Vu, Do Van Can. Applying of image processing technology in classifying tomatoes after harvest, *Journal of Science - Quy Nhon University*, **2020**, *14*(5), 60-67.

https://doi.org/10.52111/qnjs.2021.15502

TẠP CHÍ KHOA HỌC
TRƯỜNG ĐẠI HỌC QUY NHƠN

Phân tích quá trình điện từ của máy biến áp khi đóng vào lưới điện bằng phần mềm Ansys Maxwell

Đoàn Thanh Bảo[1,*], Hà Huỳnh Huy Vũ[2]

[1]Khoa Kỹ thuật và Công nghệ, Trường Đại học Quy Nhơn, Việt Nam
[2]Ban quản lý cấp và thoát nước huyện Tây Sơn, tỉnh Bình Định, Việt Nam

Ngày nhận bài: 20/08/2020; Ngày nhận đăng: 20/09/2020

TÓM TẮT

Máy biến áp khi đóng vào lưới điện, sinh ra dòng điện cao trong cuộn dây và từ thông trong mạch từ tăng lên gây bão hòa mạch từ. Thời gian bão hòa mạch từ xảy ra có thể lên đến vài chu kỳ dòng điện. Đồng thời, dạng sóng dòng điện sơ cấp chứa thành phần sóng hài và có thể gây ra sự tác động nhầm cho các thiết bị rơle hoặc ảnh hưởng đến sự làm việc cho các thiết bị điện xung quanh khác. Bài báo đã xây dựng một mô hình Máy biến áp có công suất 250kVA bằng phần mềm Ansys Maxwell 3D để tính dòng điện đóng vào lưới điện trong trường hợp định mức và không tải. Kết quả về các giá trị dòng điện, điện áp và từ cảm của máy lần lượt được phân tích. Từ đó giúp cho các kỹ sư thiết kế, chế tạo và vận hành, lựa chọn phương án phù hợp trong trường hợp máy biến áp đóng điện vào lưới điện.

Từ khóa: *Ansys Maxwell, máy biến áp, từ cảm, bão hòa mạch từ, dòng điện không tải.*

**Tác giả liên hệ chính.*
Email: dtbao@ftt.edu.vn

https://doi.org/10.52111/qnjs.2021.15503

JOURNAL OF SCIENCE
QUY NHON UNIVERSITY

Analysis of electromagnetic on transformer due to inrush power system by Ansys Maxwell

Doan Thanh Bao[1,*], Ha Huynh Huy Vu[2]

[1]Faculty of Engineering and Technology, Quy Nhon University, Vietnam
[2]Water Supply and Drainage Management Board, Tay Son District, Binh Dinh Province, Vietnam

Received: 20/08/2020; Accepted: 20/09/2020

ABSTRACT

A current in the winding and a flux in the magnetic circuit increase very high when a transformer is connected to the grid. This is the cause of the magnetic circuit saturation. The time of magnetic circuit saturation can occur up to some the frequency of alternating electric current. At the same time, the primary current waveform contains a harmonic component and may cause malfunction of relay devices or impair operation of other surrounding electrical equipment. The paper has built a simulation model using Ansys Maxwell 3D to calculate the transformer inrush current with a power of 250 kVA to the grid in the case of load and no load. The results of the current, voltage and inductance values of the machine which are analyzed one after another help engineers to design, manufacture and operate, choose the appropriate plan in case the transformer is connected to the grid.

Keywords: *Ansys Maxwell, transformer, self-induction, magnetic circuit saturation, no-load current,*

1. INTRODUCTION

When the transformer is working, there is a sudden change in the working mode of the machine. It is a transient process in the transformer. Actions occur when the transformer to the mains is closed, when the load changes or when a sudden short circuit occurs, etc. The transient process consists of two main phenomena called overcurrent, surge current and overvoltage, surge voltage. These transients occur in a very short time. It causes the circuit from the transformer to saturate, or large currents, high voltages to appear suddenly, which damage the windings of the transformer.[1,2]

In transformers, the relationship between the magnetic flux in the magnetic circuit and the no-load current is one of the nonlinear magnetization curve relationships. When the transformer is connected to the grid at no-load, the no-load current increases tens of times higher than the rated current in microseconds and the magnetic flux in the magnetic circuit will reach its maximum value. Even the flux saturation value reaches to 2 Tesla.[1,3-5]

In this paper,[6] the author proposed an approach to calculate the closing current to the grid of a three-phase transformer. Nonlinear inductance is used to simulate core saturation. This article has used electrical and magnetic circuit models. The author performed by using both experiments and simulations. Experimental and simulation results show the current waveforms closed to the grid and methods to reduce this current. Then, the author uses the magnetic circuit model proposed in the article.

**Corresponding author.*
Email: dtbao@ftt.edu.vn

https://doi.org/10.52111/qnjs.2021.15503

The paper also makes recommendations in this way to reduce the cost of designing and manufacturing three-phase transformers.

Article[7] discussed digital models of common single-phase transformers. The addition of mathematical relationships helps to determine the closing current to the grid and the working current in different processes. The article calculates and compares the waveforms and pulses of the inrush current of the transformer. In addition, the article also calculates the heat released in the transformer windings.

This paper implements a transformer of closing to the grid with a capacity of 250 kVA using the finite element method with Ansys Maxwell 3D software. First, the transformer to the grid in the case of rated load to check the correctness of the theoretical model. Then executing the model in the case of no-load transformer. Model analysis results in current, voltage and inductance values. Since then, the study of using this method for the overvoltage or overheating phenomena of transformers creates an alternative approach for further research.

2. CONTENT

2.1. Current and magnetic flux when energizing a single-phase power transformer

Under no load operation, the current flowing in the transformer (I_0) has a small value and may not exceed 10% of the rated current. But in the transient period when energizing a power transformer, the inrush current will have an excessive high value, and (???) multiple times of the rated current.[1,2,3]

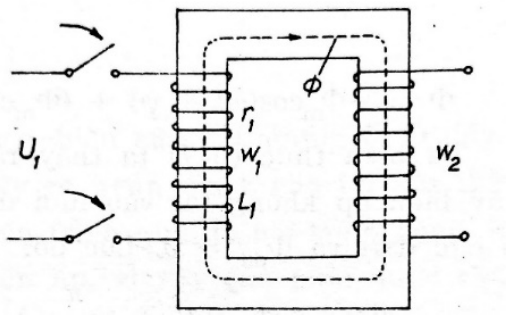

Figure 1. Energizing circuit of a single-phase transformer

In Figure 1, when applying a sinusoidal voltage to one of the transformer's windings, based on the Kirchhoff Voltage Law, we have:

$$U_{1m}\sin(\omega t+\psi)=i_0 r_1+\omega_1\frac{d\Phi}{dt} \quad (1)$$

Where

ψ: voltage phase angle, rad

ω: the velocity angle of the input voltage, rad/s

i_0: the instantaneous value of the no load current, A

r_1: resistor of transformer winding, Ω

W_1: number of turns of the winding

Φ: linkage flux

The relationship between Φ and i_0 is based on the magnetization curve of the transformer, which means (1) is a non-linear derivative equation. For simplification, we assume that the linkage flux proportional to the no load current by the following equation:

$$i_0=\frac{\omega_1\Phi}{L_1} \quad (2)$$

Inductance of the primary winding (L_1) is constant, from Equation (2) and Equation (1), we have:

$$\frac{U_{1m}}{W_1}\sin(\omega t+\psi)=\frac{r_1}{L_1}\Phi+\frac{d\Phi}{dt} \quad (3)$$

Using the classic integration method or Laplace operator method to obtain the linkage flux Φ of the transformer. The resulting flux includes two terms which are the steady state term and the transient term:

$$\Phi=\Phi_{xl}+\Phi_{td} \quad (4)$$

The steady state term of the flux is calculated as:

$$\Phi_{xl}=\Phi_m\sin(\omega t+\psi-\frac{\pi}{2})=-\Phi_m\cos(\omega t+\psi) \quad (5)$$

with: $$\Phi_m=\frac{L_1U_{1m}}{W_1\sqrt{r_1^2+(\omega L_1)^2}}$$

And the transient term of the flux is calculated as

$$\Phi_{td} = C.e^{-\eta t/L_1} \quad (6)$$

The integral constant C is determinded by the initial condition (t = 0). In this condition, the transformer core also remains an amount of flux called residual flux ± Φres which means

$$\Phi_{t=0} = \left[\Phi_{xl} + \Phi_{td}\right]_{t=0} = -\Phi_m \cos\psi + C = \pm\Phi_{du}$$

Then: $C = \Phi_m \cos\psi \pm \Phi_{du}$

$$\text{And } \Phi_{td} = (\Phi_m \cos\psi \pm \Phi_{du}).e^{-\eta t/L_1} \quad (7)$$

From Equations (4), (5) and (7), we have:

$$\Phi = \Phi_{xl} + \Phi_{td} = - \Phi_m \cos(\omega t + \psi) + (\Phi_m \cos\psi \pm \Phi_{du}).e^{-\eta t/L_1} \quad (8)$$

From Equation (8), the optimum condition to energize the transformer is when the initial phase angle of the applied voltage ψ equals π/2 and the residual flux is zero (Φ_{res} = 0). Then the transformer linkage flux becomes:

$$\Phi = - \Phi_m \cos(\omega t + \frac{\pi}{2}) = \Phi_m \sin\omega t \quad (9)$$

The flux is purely sinusoid because the transient term has been eliminated, and the steady state operation of the transformer is established immediately.

In contrast, the most undesirable condition to connect a transformer to power grid is when the initial angle of the applied voltage ψ is zero and the residual flux has a positive value. Then the linkage flux becomes:

$$\Phi = - \Phi_m \cos\omega t + (\Phi_m + \Phi_{du}).e^{-\eta t/L_1} \quad (9)$$

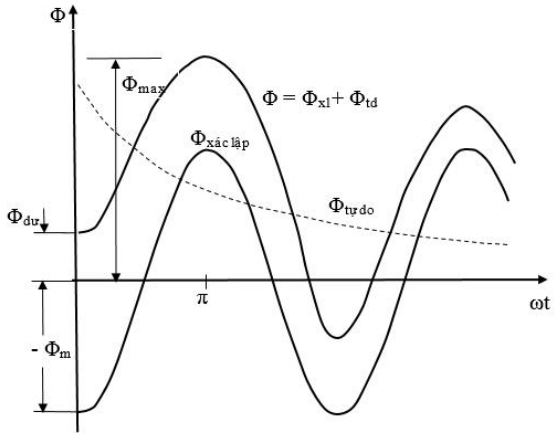

Figure 2. Flux variation Φ=f(ωt) when energizing a power transformer

Figure 2 shows the transformer flux according to angular frequency (ωt) based on Equation (10). As shown in Figure 2, the flux gets its maximum value when the angular frequency equals π (ωt = π), after half cycle.

When $r_1 << \omega L_1$, then:

$$e^{-(r_1/L_1)t} = e^{-(r_1\pi/\omega L_1)} \approx 1$$

The residual flux depends on the construction of the magnetic circuit which is the transformer core construction, and also depends on the type of core laminates. Magnetic circuit having obtuse or perpendicular coupling will get a small residual flux value. In contrast, the alternating construction has a high magnetic residue B = 0.6 ÷ 1.0T.

Therefore, the maximum flux value shown in Figure 2 is double compared with the normal operation value, so the transformer core is strongly saturated and the magnetization current i_0 during the energizing transient will be many times larger than the steady state I_0.[1,2]

2.2. Finite element method using Ansys Maxwell software

2.2.1. Ansys Maxwell software

Ansys Maxwell[8] is a high performance interactive software package that uses finite element analysis to solve electrical and magnetic problems. Maxwell solves electromagnetic problems by solving Maxwell's equations in the limited space domain and implementing Electrostatic, Magnetostatic, Eddy Current and Magnetic Transient solvers.

The process of solving the problem on Ansys Maxwell is summarized in Figure 3:

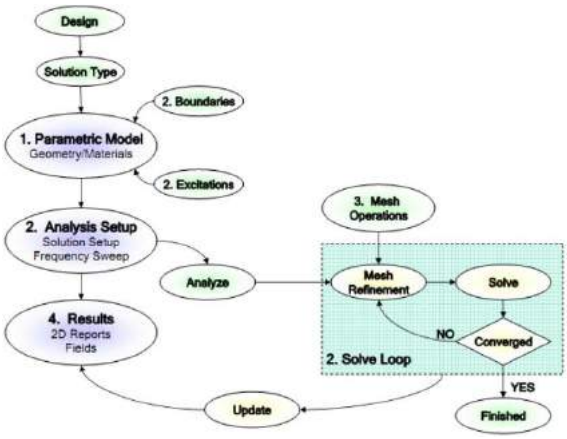

Figure 3. The process of solving the problem using the Finite Element method

https://doi.org/10.52111/qnjs.2021.15503

Ansys Maxwell is a package included in ANSYS Electronics Desktop software V19.R1; copyrighted software (license) at the computational and simulation room of the Faculty of Engineering & Technology, Quy Nhon University.

2.2.2. Transformer using Ansys Maxwell software

Table 1 shows the parameters of a 250 kVA power transformer from SANAKY in Ha Noi. The detailed dimension is obtained from the drawings provided by the manufacturer.

The parameters shown in Table 1 and design dimensions of the transformer will be the input data for Ansys Maxwell software.[8]

Table 1. Transformer parameters

No.	Parameters	Value
1	No. of phase	3
2	Frequency [Hz]	50
3	Rated power [kVA]	250
4	Winding diagram	Y/Y
5	Rated voltages [kV]	35/0.4
6	Number of turns per phase in Primary/Secondary side [turns]	2800/32
7	Rated currents [A]	4.12/361
8	Primary/Secondary winding diameter (mm)	0.8/1.5
9	No load current (%)	2
10	Short circuit voltage u_k (%)	5.7

Figure 4 shows the transformer model used in Ansys Maxwell 3D.

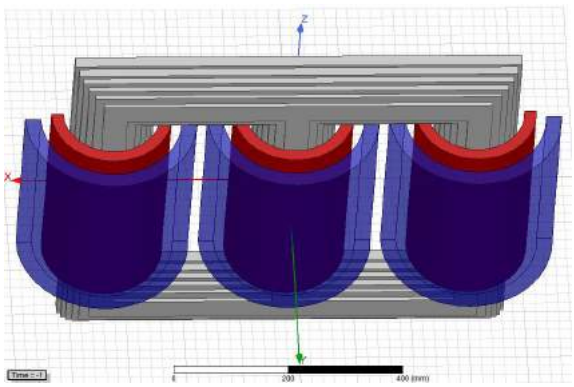

Figure 4. Transformer model used in Ansys Maxwell 3D

2.3. Analysis results in transformer mode with rated load

2.3.1. Voltage value of high voltage (HV) and low voltage (LV) windings

The investigated period in this analysis is up to 500 ms. However, in order to better observe the voltage and current waveforms, in Figures 5 and 6, the 0 ÷ 100 ms time axis has been chosen to be displayed.

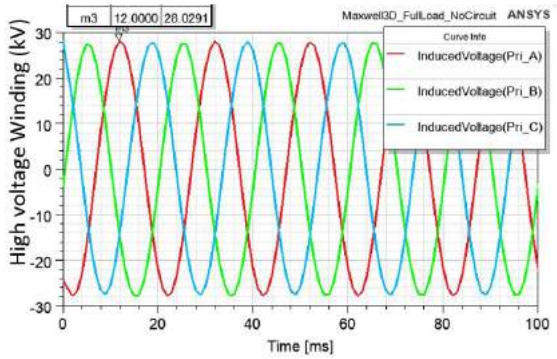

Figure 5. High-voltage winding voltage for a period of 100 ms

As shown in Figure 5, the rms value of the simulated phase voltage is $U_{Pri\text{-}A}$ = 19.82 kV compared with the rated voltage applied in transformer primary side $U_{Pri\text{-}A\text{-}rated}$ = 20.2 kV.

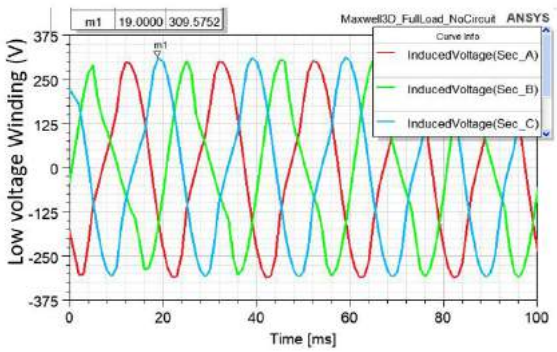

Figure 6. Low-voltage winding voltage for a period of 100ms

Also, in Figure 6 the rated value and simulation result of secondary side phase voltage are 219 V and 220 V, respectively. The error between phase voltages at primary and secondary side is about 2%.

2.3.2. Flux density in transformer core

At time t = 500 ms, when steady state is stable,

the current is equal to the rated max current value I_{HVrate} = 6.0 A. The results of flux density survey at the core of the transformer are shown in Figure 7.

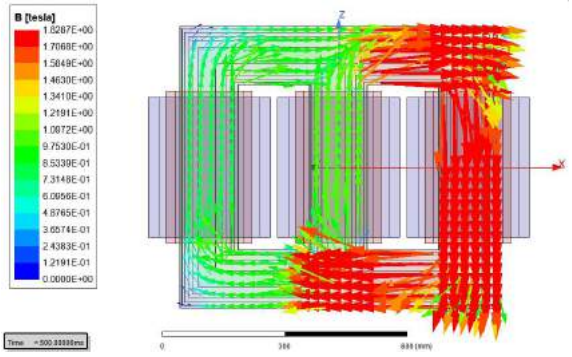

Figure 7. Vector distribution of the flux density at t = 500ms

As a result, at time t = 500 ms, the flux density at the transformer working average B = 1.0 T, but at the corners of the core magnetic circuit the flux density has the greatest value B = 1.8 T.

Analyzing the simulation results, we get the voltage and current values. These simulation results are compared with the calculated values in Table 2.

Table 2. Comparison between simulation and calculation results

No	Parameters	Simulation result	Calculation result	Error %
1	Phase voltage of HV U_1 (kV)	19.82	20.2	1.9
2	Phase voltage of LV U_2 (V)	219	220	0.4
3	Phase current of HV I_1 (A)	4.24	4.12	3.0
4	Phase current of LV I_2 (A)	364.8	361	1.0

2.4. Simulation results in transformer mode closing the high-voltage winding to the grid at no-load

2.4.1. Current result at the time of inrush current

In the case of transformer load at rated, the values of current, voltage, and inductance are compared with the calculation to be completely correct. Since then, this simulation model has been really accurate. Therefore, this model is simulated in the closed field to the grid at no-load of the transformer.

The results of the analysis of the current value when the transformer is connected to the grid and the low voltage side is unloaded are shown in Figure 8.

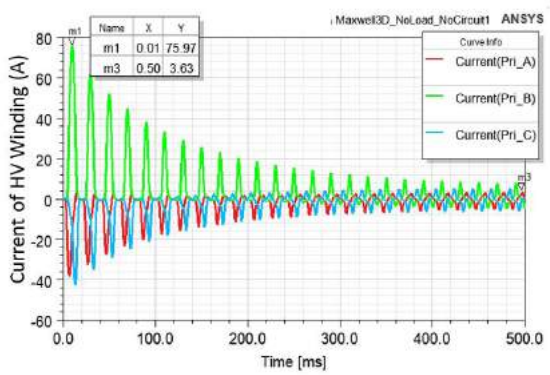

Figure 8. Current of the high-voltage winding no load for a period of 500 ms.

Figure 8 shows three phase currents at the HV winding when connecting the transformer to power grid. The current waveforms are similar to the previous case with the maximum point of the inrush current is $I_{inrush\ current}$ =75.97 A at the period t = 10 ms. In addition, a higher capacity leads to a higher transient time constant which means the current damping is slower and gets its steady state value of no-load I_{0HV} = 2.5 A after t = 500 ms.

In the currents on phase A, B, C, the reason for the current on the high-voltage winding of phase B to reach the greatest value is because at the point t = 10 ms, phase B voltage is zero.

Compared with the high-voltage current in the rated mode I_{HVrate} = 6.0 A, the transformer of the inrush current is 12.6 times higher.

https://doi.org/10.52111/qnjs.2021.15503

2.4.2. Flux density in transformer core at the time of inrush current

Flux density in the transformer core is calculated at t = 10 ms when the primary side current has the maximum magnitude $I_{inrush\ current}$ =75.97 A.

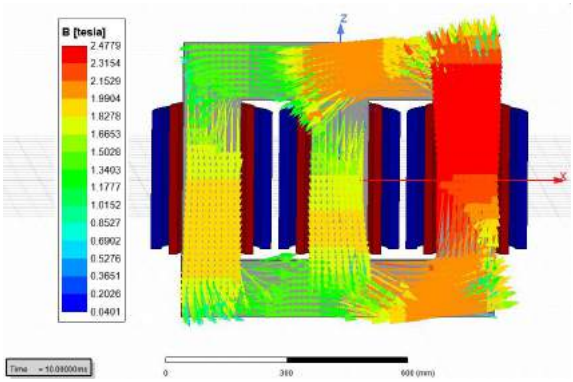

Figure 9. Vector distribution of the flux density at t = 10ms

As shown in Figure 9, at t = 10 ms, the transformer core is highly saturated with the flux density up to 2.48 T. Then, the working magnetic density of steel core B = 1.8 T, showing that the steel core reaches very strong magnetic saturation.

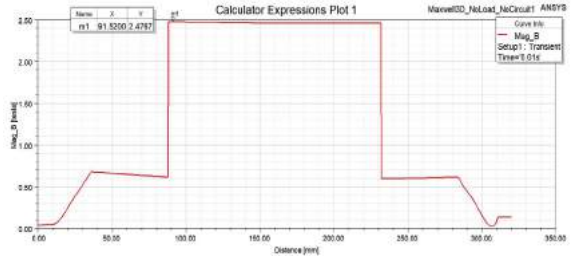

Figure 10. Distance distribution of the flux density magnitude inside transformer core at t = 10 ms.

In Figure 10, we see the results of surveying the magnetic flux density at the core of phase B reaching the maximum B = 2.48 T at time t = 10 ms.

The simulation results of current value, magnetic flux density are summarized in Table 3.

Table 3. The simulation results

Power (kVA)	Rated primary side current $I_{HV\text{-}rated}$ (A)	Maximum inrush current $I_{inrush\text{-}max}$ (A)	Maximum flux density B_{max} (T)	Proportion of the inrush current to the rated primary current (times)
250	6.0	75.97	2.48	12.6

3. CONCLUSION

Through the process of analysis, calculation and simulation, the following results have been achieved:

The Ansys Maxwell software has been applied to simulate the energizing duration of the transformers with capacity of 250 kVA under no load condition.

In the case of transformer load at rated, the values of current, voltage, and inductance are compared with the calculation to be completely correct. Since then, this simulation model has been really accurate. Therefore, this model is simulated in the closed field to the grid at no-load of the transformer.

The current waveforms are similar to the previous case with the maximum point of the inrush current is $I_{inrush\ current}$ =75.97 A at the period t = 10 ms. Compared with the high-voltage current in the rated mode I_{HVrate} = 6.0 A, the transformer of the inrush current is 12.6 times higher and the steel core is saturated with the flux density is B = 2.48 T

After damping gradually in transient period, about 500 ms, the steady-state value of the inrush current is equal to the rated no-load current of the transformer. In addition, the steel core is also saturation free and the flux density returns to the normal operating value from 1.2 T to 1.8 T.

The electromagnetic simulation results of currents, voltages and flux density have given a clear visualization of the extreme (maximum and/or minimum) values of the above quantities. Furthermore, it helps engineers and manufacturers to design, calculate, operate, and choose the appropriate plan/scenario in case a transformer is connected to power grid.

TÀI LIỆU THAM KHẢO

1. Van Binh Pham, Van Doanh Le. *Transformer – Theory – Operation – Maintenance and Testing*, Science & Technology Press, Hanoi, 2011.

2. Gia Hanh Vu, Tu Thu Phan, Khanh Ha Tran. *Electric Machine I*, Science & Technology Press, Hanoi, 2009.

3. Agasti Sanjay Kumar, Nitika Ghosh. *Investigation of various affecting factors and reduction technique of transformer magnetizing inrush current,* International Conference on Computation of Power, Energy Information and Communication (ICCPEIC), 2016, 307–310.

4. Madani Seyed Majid, Student Member, Mehrdad Rostami, Senior Member, Gevork B. Gharehpetian, Senior Member, Lance E. Pope. Inrush current limiting of transformer primary winding with grounded or nongrounded Y-connection using diode bridges, *Canadian Journal of Electrical and Computer Engineering*, **2017**, *40*(3), 229–236.

5. Mitra Joydeep, Xufeng Xu, Mohammed Benidris. Reduction of three-phase transformer inrush currents using controlled switching, *IEEE Transactions on Industry Applications*, **2019**, *56*(1), *890-897.*

6. Mitra Joydeep, Mohammed Benidris. A controlled switching approach to reduction of three-phase transformer inrush currents, *IEEE Industry Applications Society Annual Meeting (IAS)*, **2018**, 1–7.

7. Paweł Surdacki, Leszek Jaroszyński, Łukasz Woźniak. Modeling of the inrush current in superconducting transformers using PSpice, *Applications of Electromagnetics in Modern Engineering and Medicine (PTZE)*, **2019**, 224–227.

8. Electromagnetic and Electromechanical analysis. *Ansys Maxwell 3D* 19, *User's guide - Maxwell 3D,* Advanced Technology Joint Stock Company, 2019.

https://doi.org/10.52111/qnjs.2021.15503

TẠP CHÍ KHOA HỌC
TRƯỜNG ĐẠI HỌC QUY NHƠN

Thiết kế hệ thống điều khiển và giám sát theo hướng thông minh cho đô thị có hệ thống chiếu sáng phân tán

Lê Thái Hiệp*, Đinh Quốc Đạt

Khoa Kỹ thuật và Công nghệ, Trường Đại học Quy Nhơn, Việt Nam

Ngày nhận bài: 25/12/2020; Ngày nhận đăng: 05/04/2021

TÓM TẮT

Hiện nay, các hệ thống chiếu sáng đô thị theo hướng thông minh có thể điều khiển và giám sát đến từng điểm trên nền tản IoT. Nhưng làm như vậy chưa thực sự phù hợp về chi phí với các nước đang phát triển. Bài báo đề xuất giải pháp điều khiển và giám sát cho các dãy đèn trên từng tuyến phố. Nghiên cứu này đã sử dụng cảm biến ánh sáng để phân biệt ngày và đêm, cảm biến hồng ngoại để đếm lưu lượng phương tiện đang lưu thông trên phố. Từ đó điều khiển đèn trên phố phù hợp với lưu lượng giao thông. Bên cạnh đó, tại phòng điều khiển trung tâm các kỹ sư và kỹ thuật viên có thể đặt lệnh điều khiển cụ thể cho các nhóm đèn trên các tuyến phố, nhằm đảm bảo lượng ánh sáng rực rỡ cho một số đường phố trong những ngày hội. Trạng thái của các dãy đèn trên phố, cùng các thông số đo lường được giám sát ở phòng điều khiển. Giải pháp đã đề xuất vẫn đảm bảo điều khiển linh hoạt, thích nghi với lưu lượng phương tiện giao thông và tiết kiệm năng lượng.

Từ khóa: *Chiếu sáng đô thị, chiếu sáng đường phố, điều khiển và giám sát hệ thống chiếu sáng đô thị, chiếu sáng thông minh.*

**Tác giả liên hệ chính.*
Email: lethaihiep@qnu.edu.vn

JOURNAL OF SCIENCE
QUY NHON UNIVERSITY

Design of control and monitoring system for smart distributed urban lighting system

Le Thai Hiep*, Dinh Quoc Dat

Faculty of Engineering and Technology, Quy Nhon University, Vietnam

Received: 25/12/2020; Accepted: 05/04/2021

ABSTRACT

Currently, smart city lighting systems can be controlled and monitored to each light source on an IoT platform. But those systems are not cost-effective for developing countries. This paper proposes a control and monitoring solution for lights on each street. In this research, light sensors are used to detect day or night, and infrared sensors are used to count the traffic volume on each street. On this basis, lights on the street are controlled in accordance with the traffic density. In addition, in order to ensure the high light intensity for some streets during festivals, engineers and technicians can set specific control commands to groups of lights on those streets at the central control room. The on or off state of groups of street lights, and measurement parameters are monitored in the control room. The proposed solution still ensures flexible control, adapts to traffic volume and saves energy.

Keywords: *City lighting, street lighting, control and monitoring of city lighting systems, smart lighting.*

1. INTRODUCTION

Economical and highly efficient use of energy sources, especially electricity are very importantbecause it both saves money and protects the environment through prevention of global warming, ozone depletion, environmental pollution, and natural disasters, etc.

The more developed cities become, the more complete the infrastructure of smart cities is. The public lighting system makes the city brilliant at night, and contributes to ensuring traffic safety, security and order. Hence, the smart public lighting system play an important role in city development.

Although a lighting system has an important role, it is distributed throughout the urban area. Therefore, lighting systems is not easy to manage, control and monitor. So far, only a few cities in Vietnam have applied technology to manage and control of public lighting systems, such as Hanoi, Ho Chi Minh City, etc. However, these systems also have certain limitations. Besides, some parts are not suitable for Industrial Revolution 4.0.[1] Presently, the lighting system is still manually managed in most cities and towns in Vietnam. For example, the public lighting system in Quy Nhon city is currently manually operated. Operators must go to many places, where the control cabinets are located, to set the time to turn on and off lights, monitor and manage the system. Therefore, this system is not operated flexibly, not promptly changed according to the weather, not followed actual needs, so its operation is not saving energy and not economical.

*Corresponding author.
Email: lethaihiep@qnu.edu.vn

https://doi.org/10.52111/qnjs.2021.15504

Nowadays, in the world, the control technology for each light source that is suitable for the presence of vehicles on the road has been researched.[2-6] According to this control method, at each light source there is a control circuit which connects to infrared sensors, a light sensor and connects to a communication module. Moreover, in order to monitor all street lights at the control center, this center connects to each light group via a motherboard connected to all light sources in this group. However, it is not really cost-effective for developing countries like Vietnam in case this control and monitoring method is applied on a large scale.[1]

In Vietnam, Electric and Telecommunications Technologies Corporation has researched and designed a system to control public lighting from the center through a mobile communication network based on the web server, which is tried in Bac Giang in 2016.[7] The system consists of a control center integrated data monitoring software on computers, field cabinets measure the parameters of current, voltage, transmitter receiver devices transmit signals via the mobile communication network (with SIM card) to the control center. At the control center, operators can detect the problem, turn on and off street lights, and switch off alternating phases easily and conveniently. However, this system does not yet contain adaptive control for weather and traffic volume.

Besides, the control urban lighting system had been also researched and designed towards smart and energy saving based on the application of communication techniques via GSM/GPRS/3G wireless network combining microcontroller and electronic power.[8,9] The function of controlling the on/off of the lighting system automatically according to weather forecast or predetermined switching schedule are augmented into monitoring and control system. This urban lighting control system is commanded entirely from the control center. However, this system is not capable of detecting vehicular traffic on the street, where the lights are directly illuminated.

Moreover, the smart public lighting system using LEDs designed by a research team at Ho Chi Minh City University of Technology consists of 3 parts: LED light set, control cabinet combined with gateway, and control center. [10] At lights is also equipped a control circuit and a data transmission device with a connection to a control center, to control and measure the parameters of those lights. A lights group is controlled directly or automatically turns on and off remotely by a control cabinet, which also performs measurements of various parameters in the street lighting grid. At the supervisory - control center, the system allows monitoring overload, voltage, phase error, and the energy consumption during the day and night to be also reported in real time. This system is a type of control to each light source, so its installation cost is not suitable for large-scale deployment in Vietnam.[1]

In general, current studies in Vietnam still have some inappropriate points as mentioned above. Therefore, the goal of this paper is to build up a smart urban lighting system capable of automatically and appropriately with parameters collected such as traffic density, weather, etc. In addition, this system is connected to computers and smartphones through wireless communication. Operators can easily manage the system no matter where they are. Currently, there are many projects that are interested in investing in this field, such as Sapulico Company projects,[11] or Asian Development Bank (ADB) projects,[12] etc.

2. SOLVING PROBLEM

2.1. Research method

This research comes from the fact that the public lighting system in urban areas still have some inappropriate points and less flexibility. This

study has analyzed the technical requirements of public lighting systems. Based on these requirements, this study has proposed the design of a control and monitoring structure for the public lighting system that is flexible and adaptable to actual conditions. The flexibility and adaptability of the proposed system have been verified through experiment.

2.1.1. Technical requirements

An urban lighting system must be automatically turned on and off, and it is able to reducethe number of lights illuminating or the capacity of each light in the off-peak hours when traffic density is low to save energy. This control is done according to preset scenarios applied in most cities today or adapted to the actual conditions just implemented in some cities of developed countries.

The method of alternately turning off lights to reduce the number of lights illuminating is still used mainly in the urban lighting systems. This is done in the lighting control cabinet by two contactors that are controlled by two timer relays (Figure 1). A control cabinet as shown in the diagram in Figure 1 allows turning on or off the lights according to two different branches, thereby the number of lights illuminating is reduced in two different ways.[13]

It is possible to adjust the on and off time of lights by changing the parameters of the timer relayas usually suggested in the following scenario:

+ In the evening from 18h00 to 23h00, and from 4h00 to 6h00: 100% of the lights are turned on;

+ In the late night, from 23h00 to 04h00: a third of the total lights are turned off, and two-thirds of the total lights are turned on;

+ During the day from 06h00 to 18h00: all are completely off.

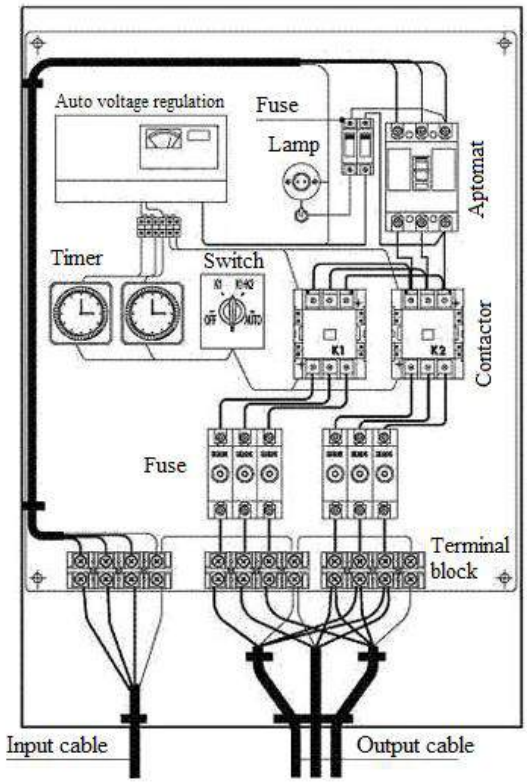

Figure 1. The structure of an ordinary lighting control cabinet.

2.1.2. Proposal of a control and monitoring structure of urban lighting system

Today, with the strong development of automation technology, and combined achievements of microelectronics and information technology, it is possible to create an automation solution in all fields. Automation has become an inevitable trend for all fields in any country and territory. Automation of smart urban lighting system is definitely an inevitable issue.

From the requirement techniques, a smart urban lighting control and monitoring system structure is proposed as can be seen in Figure 2.

At field level, values from the light sensor (the photoresistor sensor used in this study) and the infrared sensor are regularly read by a control circuit (an Arduino UNO circuit is used in this study). Light sensors are used in control cabinets to turn on lights when it is dark, and turn off lights at dawn. Infrared sensors are placed

https://doi.org/10.52111/qnjs.2021.15504

at the entrance points of streets. These sensors provide signals to control cabinets to reduce the number of lights illuminating when there are few people on the street. When the time between two detections of a passing person is far apart:

+ In case there is no traffic in more than 15 minutes, the number of lights illuminating will be reduced by a third;

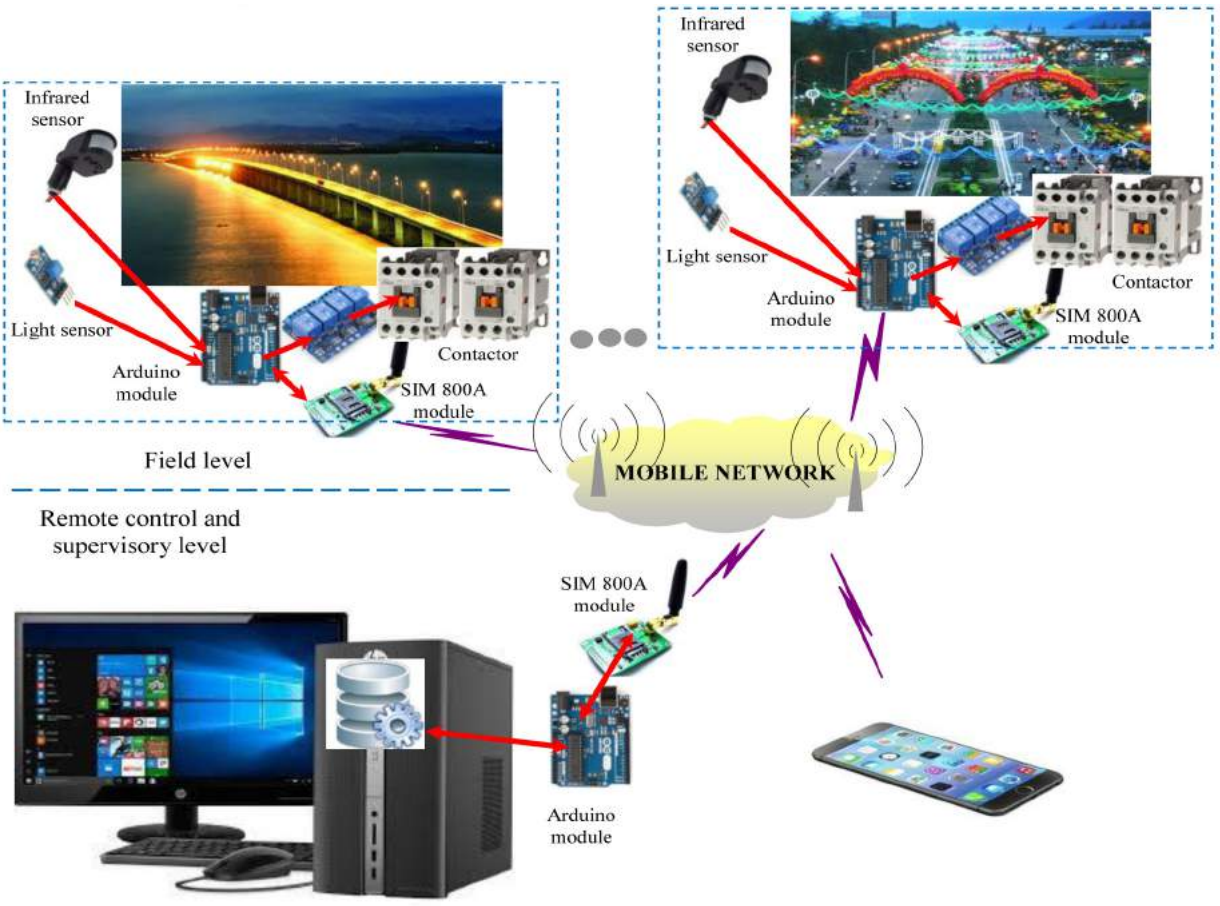

Figure 2. Structure of control and monitoring system for smart distributed urban lighting system.

+ In case this street is with vehicle in the next 15 minutes, the number of lights illuminating will be increased by a third;

+ In case there is no passerby in the next 15 minutes, then two thirds of the total of lights will be turned off.

All control commands and data monitoring of urban lighting system are saved on a server computer. Urban lighting system can be remotely controlled and monitored by smartphones or computers that are connected to data in the server via mobile network or internet. Control commands are set up on a software in smart-phones and computers. Then these commands are sent to control cabinets at the field level. The on or off state of lights and other parameters are collected by control cabinets. Then these signals are transmitted to the control center via the mobile network. Because sending commands and receiving parameters do not need to respond in real time (a delay is still an accepted). Consequently, SIM modules are used to connect wireless communication between the control center and control cabinets at the field level by sending and receiving messages. As a result, communication costs are reduced to a very low rate. The low cost of communication combined with the low cost of equipment in the control system are advantages of the system, making it easily applied on a large scale.

2.2. Research tools

The smart urban lighting control and monitoring system is designed on the basis of using commercially available devices and modules to ensure reliability in use.

The devices for interacting with users are computers and phoneswhich are popular today. Moreover, Arduino UNO R3 circuits, SIM 800A modules, infrared sensor modules, light sensor modules, intermediate relay modules, etc. are used this system. Besides, electrical power equipments are also used in lighting control cabinets, such as electricity meters, aptomat, contactor, etc.

2.2.1. Arduino UNO R3 module

An Arduino board consists of an AVR microcontroller with add-on components that make programming easy. An important feature of the Arduino is its standard connections, which allow users to connect the board's CPU to other modules. So, it is easy to change function and use target item. Expansion modules can communicate with the Arduino board directly via pins, or via serial communication I2C. Multiple modules can be stacked and used in parallel. ATmega series of AVR microcontrollers, especially ATmega8, ATmega168, ATmega328, ATmega1280, and ATmega2560 are usually used for Arduino.

Arduino allows to load program directly from the computer to the module through the USB port without using any other external module. Arduino circuits are programmed via USB thanks to built-in converter such as the FTDI FT232. In addition, some Arduino modules have other ways of connection, such as RS-232, or a detachable serial communication cable, or Bluetooth.

2.2.2. SIM module

GSM/GPRS SIM800A module (upgraded from SIM900A) integrated pulse source with compact design. But, this module still retains the necessary elements for the circuit to operate stably, including: high-current pulse source circuit, RS232 MAX232 communication IC, standard SIM slot and signal LEDs, GSM antenna. The SIM module is used for the purposes of calling, texting SMS GSM, and GPRS.

GSM/GPRS SIM800A modules communicate with the microcontroller circuits via UART serial communication. It is noted that microcontrollers using 5VDC need to add a logic level converter or voltage divider to 3.3VDC to avoid damage SIM modules.

2.2.3. Infrared sensor module

Infrared sensors use PIR technology to detect human movement. When a human movement is detected, its output is immediately activated. This module is connected to the Arduino circuit at the field level.

In particular, the sensitivity and the delay time to keep output's state of infrared sensor modules can be adjusted. Moreover, users can also adjust the sensor to work only at night or all day and night.

2.2.4. Light sensor module

Photoresistor that is used to detect light intensity is a type of light sensor. The value of DO output of the sensor module depends on the light intensity of the environment. When it is bright, the DO output is 0. If it is dark, the DO output is 1. On the sensor module, there is a potentiometer to adjust the sensitivity to light intensity.

2.2.5. Relay module

Output power of Arduino UNO modules are not enough to drive contactors in the dynamic circuit. For this reason, it is necessary to use an intermediate relay as a control bridge.

Relay modules are suitable to convert from DC current to AC current. These modules are used for devices that consume high intensity current. These modules are compact design, with opto and transistor isolation, low level trigger (0V) suitable for all types of microcontrollers.

https://doi.org/10.52111/qnjs.2021.15504

2.3. Design and programming

2.3.1. Hardware design

The hardware of the urban lighting control and monitoring system is designed according to the system structure proposed above (as shown in Figure 2).

The controller and monitor at the field level is designed as demonstrated in Figure 3. Here, an Arduino circuit does the main task, including control, monitoring and communication. The other modules are responsible for supporting this circuit. Specifically, the light sensor module is used to detect whether it is bright or dark; infrared sensor module is used to detect traffic volume; relay module is a control bridge to contactors, that turn on or off lights; the SIM module is used to communicate with control and monitoring center; the DC module supplies power to the modules in this cabinet.

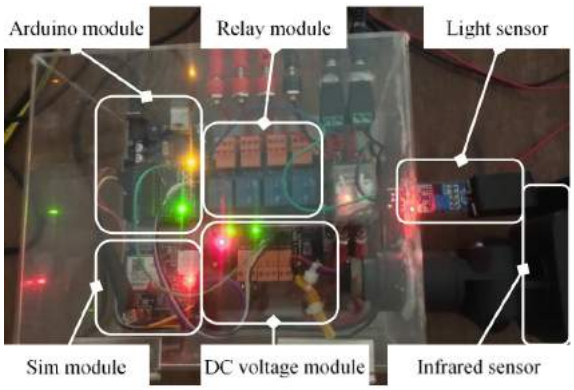

Figure 3. Controller, data collection and communication at field level.

In the control and monitoring center, a data and communication processor system is designed (as shown in Figure 4) to connect wirelessly to control cabinets at the field level. Here, the control commands from the computer are transmitted through an Arduino module, and then they are sent as messages by a SIM module. The data from the field levelsent in the form of messages - is received by the SIM moduleand then is forwarded through the Arduino module to the computer for monitoring.

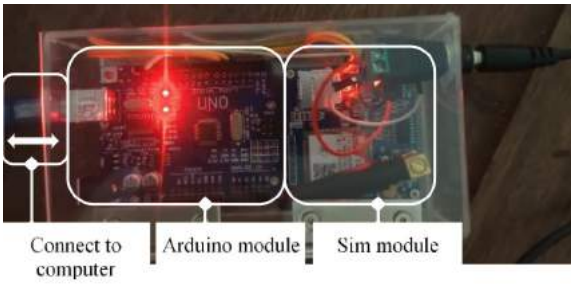

Figure 4. Data processing and communication in the control and monitoring center.

The designed urban lighting control and monitoring system was tested with a road that is a scale model with inside median lights (Figure 5).

Figure 5. Experimental street light model.

2.3.2. Programming

a. Programming for Arduino at field level

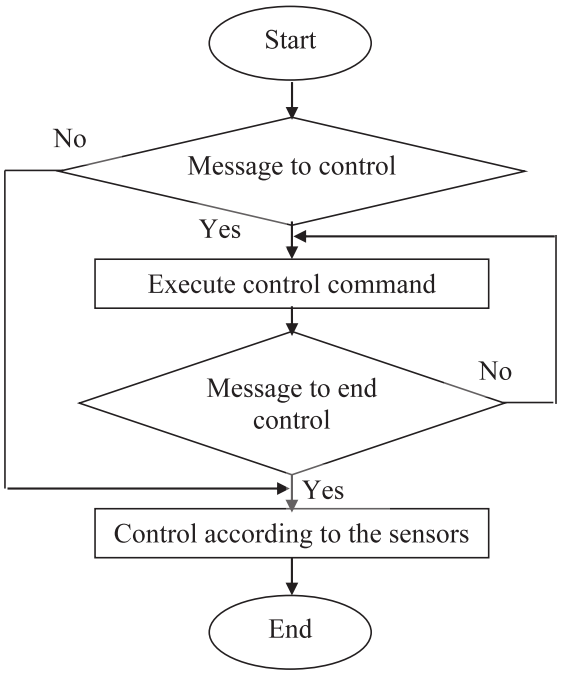

Figure 6. Algorithm flowchart of a program in a loop in Arduino at field level.

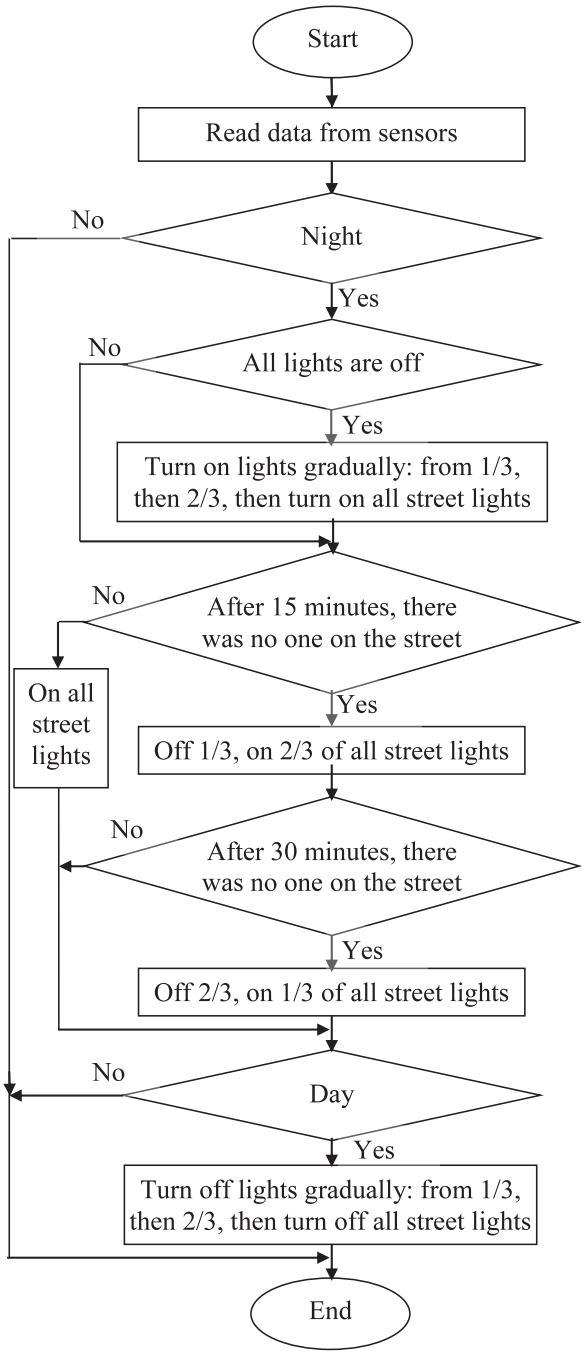

Figure 7. Algorithm flowchart of control program according to sensors in a loop in Arduino at field level.

At the field level, Arduino modules receive the control commands in the form of a message from the control and monitoring center and executes them (as flowchart in Figure 6). The control of the center is only done during holidays and festivals. If there is no control command from the center, the Arduino modules at field level collect information from the streets to control lights (like Figure 6 and Figure 7). The control method according to the collected information from the streets makes the system adaptable to changes of traffic volume and weather.

The Arduino modules at the field level control street lights according to sensors as the algorithm diagram shown in Figure 7. This diagram shows the principle of operation details of this system, which is presented in Section 2.1.2.

b. Programming interfaces for smartphones

The software that allow operators to control and monitor the urban lighting system on the smartphone is programed following the steps below:

Step 1: Create a project: File → New → Default. Then, choose a path to save the file.

Step 2: Create Layout: Click Designer → Open Designer. Code of the objects on the Designer interface are written in the main window.

Step 3: Connect to Leapdroid: Click WYSIWIG → Designer Connect.

c. Programming interfaces for computer

The monitoring console on the computer is programed in Visual C# language.

3. RESULTS AND DISCUSSION

At each control cabinet, the signal of a light sensor is read by an Arduino module. Then, lights are turned on when it is dark and turned off at dawn. Based on signals of infrared sensors, all lights are turned on when the street is crowded, or some lights are turned off when there are few people on the street. When the time between two detections of passing people is far apart, the lights are turned off or turned on according to the principle proposed in Section 2.1.2. The results are shown in Figure 8.

During festivals, operators can use an application written for smartphones and computers to send control commands to the control cabinets at the field level (Figure 9, Figure 10). At the control cabinet, the SIM

https://doi.org/10.52111/qnjs.2021.15504

module receives control commands in message form and transmits it to an Arduino module, then the lights are turned on or off according to these control commands by contactors. Here, data from the sensors are read by an Arduino module, which transfers this data to a SIM module, then it is sent to the server computer in the control center. As a result, the status values of the lights, and many other parameters are monitored on smartphones and computers that access to the server computer (Figure 9, Figure 10).

(a)

(b)

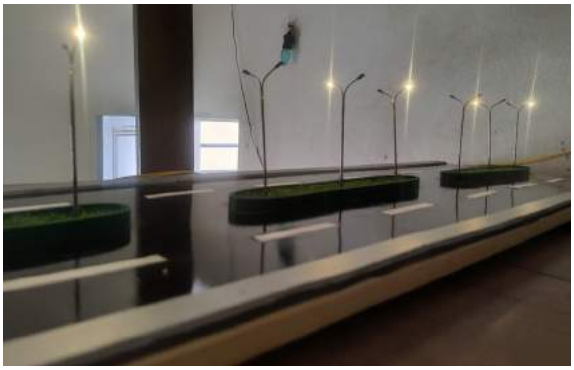

(c)

Figure 8. (a) All street lights are turned on, (b) 2/3 street lights are turned on, (c) 1/3 street lights are turned on.

Figure 9. Control and monitoring application in smartphones.

Figure 10. Control and monitoring application in computer.

4. CONCLUSIONS

This study has designed a smart urban lighting control and monitoring system. The designed system has some following features:

i) Operators can control and monitor the urban lighting system by computers and smartphones connected to the server computer in the control center;

ii) The lights on the streets are automatically turned on when it gets dark, and turned off when the sun shines;

iii) In the evening, the number of street lights turning on and off depends on the traffic volume on each street.

This study is not aimed at controlling each light source because it requires a very large initial investment cost. In terms of lighting quality, the

proposed method in this study is not as good as the control method for each light source. But in terms of flexibility and adaptability, the test results of this study have shown that the urban lighting system is operated adaptively according to the actual traffic volume in each street.

Therefore, the proposed method in this study should be applied to secondary roads in urban areas, where there are control cabinets to turn on and off street lightings. Nevertheless, main roads and national highways need lighting quality even if street lights turn on with power-saving mode, these roads should be invested the control technology for each light source or auto-dimming street lights. This combination not only ensures good lighting quality where needed, but also saves electrical energy, making it suitable for investment because the total length of secondary roads in urban areas is usually much longer than that of main roads and national highways passing through the city.

REFERENCES

1 Le Trung Kien. Management and operation of urban public lighting systems towards smart cities, <https://anhsangvacuocsong.vn/quan-ly-van-hanh-he-thong-chieu-sang-cong-cong-do-thi-huong-toi-do-thi-thong-minh/>, accessed on 12/10/2020.

2. Samir A. Elsagheer Mohamed. Smart street lighting control and monitoring system for electrical power saving by using VANET, *International Journal of Communications, Network and System Sciences*, **2013**, *6*, 351-360.

3. Fabio Leccese, Marco Cagnetti and Daniele Trinca. A smart city application: a fully controlled street lighting isle based on Raspberry-Pi Card, a ZigBee sensor network and WiMAX, *Sensors,* **2014**, *14*, 24408-24424.

4. Sei Ping Lau, Geoff V. Merrett, Alex S. Weddell, Neil M. White. A traffic-aware street lighting scheme for smart cities using autonomous networked sensors, *Computers and Electrical Engineering*, **2015**, *45*, 192–207.

5. Philip Tobianto Daely, Haftu Tasew Reda, Gandeva Bayu Satrya, Jin Woo Kim, and Soo Young Shin. Design of smart LED streetlight system for smart city with web-based management system, *IEEE Sensors Journal*, **2017**, *17*(18), 6100 – 6110.

6. Eveliina Juntunena, Esa-Matti Sarjanoja, Juho Eskeli. Smart and dynamic route lighting control based on movement tracking, *Building and Environment*, **2018**, *142*, 472–483.

7. Electric and Telecommunications Technologies corporation. Research on technological solutions and modernization in the management and operation of public lighting system in Bac Giang city, <https://skhcn.bacgiang.gov.vn>, accessed on 21/10/2020.

8. Tran Phuong Nam. *Studying and designing lighting control system in urban area smart and energy saving oriented,* Subject Code 14799/2018, National Agency for Science and Technology Information, 2018.

9. Tran Phuong Nam, Ngo Viet Song, Nguyen Huu Chuc, Nguyen Van Doai. Studying and designing lighting system in urban area smart and energy saving oriented, *Journal of Science & Technology - Quang Binh University*, **2018**, *15*, 3-10.

10. Ho Chi Minh City University of Technology. Mastering the technology of designing smart public lighting systems, <https://khoahocphattrien.vn>, accessed on 20/10/2020.

11. Huynh Tri Dung, Nguyen Huy Khuong. Operating the lighting system in Ho Chi Minh City towards a smart city, <https://anhsangvacuocsong.vn>, accessed on 12/10/2020.

12. Open direction for smart lighting system investment, <https://baocantho.com.vn>, accessed on 15/10/2020.

13. Dang Van Dao (ed.), Le Van Doanh, Nguyen Ngoc My. *Lighting equipment and systems*, Vietnam education publishing house, Ha Noi, 2008.

https://doi.org/10.52111/qnjs.2021.15504

TẠP CHÍ KHOA HỌC
TRƯỜNG ĐẠI HỌC QUY NHƠN

Phân lớp ảnh điện tâm đồ bằng kỹ thuật học sâu hỗ trợ chẩn đoán bệnh tim mạch

Lê Xuân Vinh[1,*], Lê Xuân Việt[1], Vũ Hoàng Thương[2]

[1]Khoa Công nghệ Thông tin, Trường Đại học Quy Nhơn, Việt Nam
[2]Liên hiệp hội Khoa học Kỹ thuật Bình Định, Việt Nam

Ngày nhận bài: 26/02/2021; Ngày nhận đăng: 12/05/2021

TÓM TẮT

Trong bài báo này, chúng tôi đề xuất mô hình phân lớp ảnh điện tâm đồ để hỗ trợ cho các chuyên gia y tế trong việc chẩn đoán bệnh tim mạch. Mô hình được xây dựng bằng kỹ thuật học sâu, được huấn luyện và kiểm tra bằng dữ liệu MIT-BIH. Cụ thể hơn, mạng nơ-ron tích chập được thiết kế với đầu vào là ảnh lấy từ điện tâm đồ và đầu ra được gắn nhãn là loại rối loạn nhịp tim tương ứng nếu có. Mô hình thu được đáng tin cậy với kết quả thử nghiệm có độ chính xác cao từ 97 - 99%.

Từ khóa: *Phân lớp, học sâu, mô hình, mạng noron tích chập, điện tâm đồ.*

**Tác giả liên hệ chính.*
Email: lexuanvinh@qnu.edu.vn

JOURNAL OF SCIENCE
QUY NHON UNIVERSITY

Classification of ECG images by Deep Learning to support the diagnosis of cardiovascular diseases

Le Xuan Vinh[1,*], Le Xuan Viet[1], Vu Hoang Thuong[2]

[1]*Faculty of Information Technology, Quy Nhon University, Vietnam*
[2]*Binh Dinh Union of Science and Technology Associations, Vietnam*

Received: 26/02/2021; Accepted: 12/05/2021

ABSTRACT

In this paper, we have proposed the electrocardiogram (ECG) classification model to partly support medical professionals. The model is built by deep learning technique with MIT-BIH training data. Specifically, the convolutional neural network (CNN) will be built to take input of images cropped from the ECG images and the output labeled as the corresponding arrhythmia. The obtained model is reliable when the test results have a relatively high accuracy of 97 to 99%.

Keywords: *Classification, deep learning, model, convolution neural network, electrocardiogram.*

1. INTRODUCTION

The electrocardiogram (ECG) is a chart that records changes in electrical current in a person's heart over a given period of time. The heart contracts itself in rhythm thanks to the heart muscle's control of its conduction system. The difference in concentration of Kali, Canxi ions on the two sides of the membrane creates a potential. The electrical current of the heart is as small as a few parts per a thousand volts. But the current is amplified, and its signal is plotted on the paper which is called ECG.

Until now, the ECG is a very popular method of monitoring the electrical activity of the heart. Most clinics, hospitals use the ECG to aid in the diagnosis of heart rhythm problems and structural abnormalities. An ECG analyst can diagnose a patient's cardiovascular disease, which requires many experiences and times from doctors. Computer-oriented approaches can effectively reduce diagnostic time, increase the number of ECG records processed, support to local health facilities where there are not many experienced ECG analysts.

According to that approach, there have been many different studies. Some classification results of ECG signals with typical methods such as frequency analysis,[1] statistical methods,[2] heuristic-based methods,[3] artificial neural networks,[4] support vector machines (SVM),[5] wavelet transform,[6] and hidden Markov models.[7] Artificial neural networks obtained an average accuracy of 90.6% for the classifier of ECG wave into six classes[8] and a feed-forward neural networks was used as a classifier for the detection of four types of arrhythmia classes

**Corresponding author.*
Email: lexuanvinh@qnu.edu.vn

https://doi.org/10.52111/qnjs.2021.15505

and obtained an average accuracy of 96.95%.[9] Most of these results are obtained by using the traditional approach to solving the classification problems on ECG data.

Machine learning has recently developed and become an approach that is able to solve the classification issue effectively in medicine. Deep learning, a subset of machine learning, has a wide range of applications in the prediction and prevention of fatal sicknesses, particularly cardiovascular diseases. A recurrent neural network achieved an average accuracy of 98.06% for detecting four types of arrhythmia.[10] A convolutional neural network model proposed for the classification from a 1-D ECG signal[11] yielded a classification accuracy of 96.72%. Another deeper 1-D CNN model proposed for the classification of ECG dataset[12] obtained an average accuracy of 97.3%. A nine-layer 2-D CNN model proposed for the classification of five different heartbeat arrhythmia types[13] achieved an accuracy of 94.03%.

As mentioned above, building the ECG classification model is an urgent need in practice, which is posed by local medical administrators. The model will be a key component of the software assisting ECG analysts. Therefore, we build the model of ECG signal image classification using deep learning technique with MIT-BIH[14] training data. Specifically, the convolutional neural network (CNN) will be built to take input as cropped images of the ECG image, and the output is labeled as the corresponding arrhythmia.

This paper is organized as follows. Section 2 presents the features of ECG data, image data obtained from the MIT-BIH database. Section 3 then proposes a CNN structure with its components and training methods to build a modeling of ECG classification. Section 4 discusses the training for the model and its accuracy. Finally, the conclusions and comments are in Section 5.

2. CHARACTERISTICS OF ECG DATA

The original data from the MIT-BIH database is one-dimensional data. From this database, the ECG images were reproduced and published on the Kaggle.[15] The ECG images of each type of arhythmia were labeled with the name of the directory in which it resides. We use this image dataset to train and evaluate the model.

Every image is a cycle of ECG. Its characteristics are waves criteria (P, Q, R, S, T, U) and the time interval between them. Several normal and typical ECG cycles are plotted as shown in the Figure 1 below.

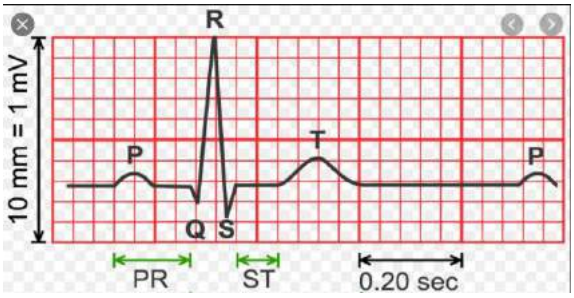

Figure 1. One cycle of ECG

The database includes 15 characteristic morphological types divided into 5 classes: (i) normal beat (N), (ii) supraventricular ectopic beat (S), (iii) ventricular ectopic beat (V), (iv) fusion beat (F), and (v) paced beats or unknown beat (Q). Details of each class are as follows:

(i) Class N consists of

R - Right bundle branch block beat

N - Normal beat

L - Left bundle branch block beat

j - Nodal (junctional) escape beat

e - Atrial escape beat

(ii) Class S consists of

S - Supraventricular premature beat

J - Nodal (junctional) premature beat

a - Aberrated atrial premature beat

A - Atrial premature beat

(iii) Class V consists of

V - Premature ventricular contraction

E - Ventricular escape beat

(iv) Class F consists of

F - Fusion of the ventricular and normal beat

(v) Class Q consists of

Q - Unclassifiable beat

P - Paced beat

f - Fusion of the paced and normal beat

The data are divided into two sets: training and testing. The number of images in each episode is as follows.

Table 1. Number of images in the datasets

Set	F	N	Q	S	V
Training	641	22122	6413	2222	5780
Testing	161	13661	1608	557	1448

Now, we will build a CNN network to classify the dataset just presented above.

3. THE ECG IMAGES CLASSIFIER

We know that ECG signal data has many different representations. There is a suitable treatment for each respective representation. Image data format as shown in the above section, suitable for the classification model using Convolution neural network (CNN) because the CNN has the ability to automatically extract image feature. CNN is a development of a deep neural network (DNN). Its number of parameters is less than that of DNN because it uses share weights. Thanks to this property, local features on the image are extracted, and there is no need to match the entire image, which is consistent with the ECG image's feature when processed.

The structure of CNN was first proposed by Le Cun et al. in 1989[16] and then it was improved.[17] Then, they developed a multi-layer artificial neural network called LeNet-5 which can be trained with the backpropagation algorithm[18]. Since 2006, many methods have been developed to overcome the difficulties encountered in training deep CNNs.[19-21] Most notably, AlexNet[22] is similar to LeNet-5 but with a deeper structure. Then, many studies have been proposed to improve its performance. Among them are four representations studies of ZFNet,[22] VGGNet,[23] GoogleNet[21] and ResNet.[24]

The classifier is built from the VGG16 network architecture. Basically, it consists of three types of layers, namely convolution, pooling, and fully connected layers.

Table 2. Architecture of the classifier

Layer (type)	Output Shape	Param #
input_1 (InputLayer)	[(128, 128, 3)]	0
block1_conv1 (Conv2D)	(128, 128, 64)	1792
block1_conv2 (Conv2D)	(128, 128, 64)	36928
block1_pool (MaxPooling2D)	(64, 64, 64)	0
block2_conv1 (Conv2D)	(64, 64, 128)	73856
block2_conv2 (Conv2D)	(64, 64, 128)	147584
block2_pool (MaxPooling2D)	(32, 32, 128)	0
block3_conv1 (Conv2D)	(32, 32, 256)	295168
block3_conv2 (Conv2D)	(32, 32, 256)	590080
block3_conv3 (Conv2D)	(32, 32, 256)	590080
block3_pool (MaxPooling2D)	(16, 16, 256)	0
block4_conv1 (Conv2D)	(16, 16, 512)	1180160
block4_conv2 (Conv2D)	(16, 16, 512)	2359808
block4_conv3 (Conv2D)	(16, 16, 512)	2359808
block4_pool (MaxPooling2D)	(8, 8, 512)	0
block5_conv1 (Conv2D)	(8, 8, 512)	2359808
block5_conv2 (Conv2D)	(8, 8, 512)	2359808
block5_conv3 (Conv2D)	(8, 8, 512)	2359808
block5_pool (MaxPooling2D)	(4, 4, 512)	0
flatten (Flatten)	(8192)	0
fc1 (Dense)	(4096)	33558528
dropout (Dropout)	(4096)	0
fc2 (Dense)	(4096)	16781312
dropout_1 (Dropout)	(4096)	0
predictions (Dense)	(5)	20485

Total params: 65,075,013

Trainable params: 50,360,325

Non-trainable params: 14,714,688

https://doi.org/10.52111/qnjs.2021.15505

The convolutional layer aims to learn feature of the inputs, including some of the kernels which are used to compute different feature maps. Specifically, each neuron of a feature map is connected to a region of neighbouring neurons in the previous layer. Such a neighbourhood is referred to as the neuron's receptive field in the previous layer. Note that, to generate each feature map, the kernel is shared by all spatial locations of the input. The built CNN contains 5 convolutional blocks. In which, the first 2 blocks, each block has 2 convolution layers and the remaining 3 blocks each block has 3 convolution layers.

The pooling layers are used to reduce the dimensions of the feature maps. Thus, it reduces the number of parameters to learn and the amount of computation performed. It is usually placed between two convolutional layers. Thus, there are five pooling layers and use 2D max-pooling operator.

Finally, two fully connected layers use the Relu function as activation function and Dropout to avoid overfitting. The output layer which has 5 nodes corresponding to 5 classes and softmax function is used here. The model structure is summarized in Table 2.

The classes of this model can be seen in more detail in the similar model of A. Ullah [29]

The data for the input layer are images (128, 128, 3) converted from PNG images (256, 256, 3) in the training dataset by cv2.resize( ).

4. EXPERIMENTS AND RESULTS

The work of evaluating the accuracy of the model involves training the classifier. So in the first part of this section, we will cover that process.

Recall that the data is used from the two training and testing sets as mentioned in Section 2. To make an easier and simpler machine learning model, in this paper we have converted to numerical data in npy style files. The testing data are taken as the validation data during training.

The loss function is a measure of how good the neural network is during training and is represented by the difference between a given training pattern and the network outputs. There are many different types of loss functions, but deep learning often uses cross-entropy function, which is

$$L = -\frac{1}{N}\sum_{i=1}^{N}\left(y_i \ln(a_i) + (1-y_i)\ln(1-a_i)\right) \quad (1)$$

Where N is the number of training data or the batch size, y_i is 0,1 depending on the class label and a_i is an actual value from the output layer. In case of multiple classes, the loss function L is extended from Formula 1.

To minimize the loss function, there are several well-known optimization algorithms such as Adam[25], Adagrad[26], and Adadelta[27]. Here, we choose the Adam algorithm in the training process.

The role of the activation function is to determine the output value of each node based on the input signal composite value. The nonlinear activation is widely used, including rectified linear units (ReLU), leakage rectified linear units (LReLU), and exponential linear units (ELU). Among them, the ReLU function is the most widely used, and is used in this model.

Our programs were implemented in Python programming language, using the framework of Keras. The training environment used is Google Colab. It takes about 0.5 - 1 hours to get results after 100 epochsdepending on the GPU provided by Google. The training of deep learning model could early stop scheme by using validation set. However, to gain experience, we have tried to train up to 200 epochs and found that just 100 epochs is enough to achieve a good model.

Another problem is the dropout during training. Dropout is first introduced by Hinton et al. [28], and it has been proven to be very effective in reducing overfitting. We apply Dropout to the fully connected layers. The dropout with the parameter 0.3 produces a model with good

training accuracy (99.07%), but poor validation accuracy (96.05%). Meanwhile, a dropout with parameter 0.5 results in a model with poor training accuracy (96.95%), but better validation accuracy (97.52%), perhaps avoid overfitting.

With parameters such as the batch-size is 64, dropout is 0.4, we run through 100 epochs on the training data set, the validation data is also the testing data and model accuracy and loss for the model is shown in Figure 2.

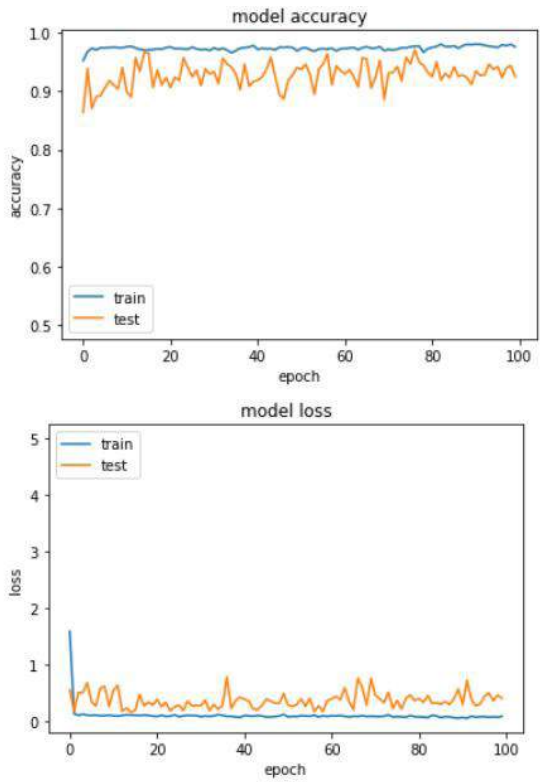

Figure 2. The model accuracy and loss

Performance of the classifier has an accuracy of 97.57% on the testing data set and an accuracy of 99.13% on the training data set.

The confusion matrix of classifier on testing data set is presented in Figure 3. Performance of the classifier has an accuracy of 97.57% .

In Figure 3, the labels of the classes corresponding to 0, 1, 2, 3, 4 are F, N, Q, S, V.

Observing the confusion matrix in Figure 3, we see that the classification performance of the model is of good quality, especially for the S and V classes. Clinically, supraventricular ectopic beats (S) and ventricular ectopic beats (V) are two critically abnormal and serious heartbeats, and the performance of the model in the test for S and V classes is very high.

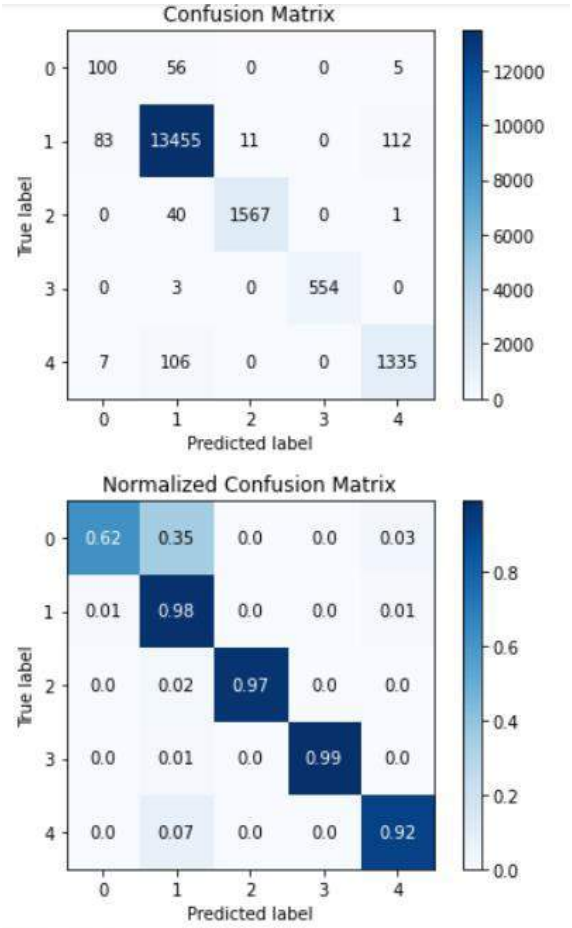

Figure 3. Confusion Matrix for testing data

Training data are also collected from patients, and we get it from the MIT-BIH database. We present more predictive results of the model on the training data set in Figure 4 for your reference. Of course, the model's classification performance on this data set is higher. Performance of the classifier has an accuracy of 99.13%.

5. CONCLUSIONS

In this paper, we have proposed the building of an ECG image classifier using deep learning techniques. The model is obtained by training a 2D-CNN on a preprocessing image set from the MIT-BIH database which has been evaluated

https://doi.org/10.52111/qnjs.2021.15505

on test data and obtained a quite high accuracy, especially the classification of abnormal and serious heartbeats. More importantly, we propose a method to build the ECG image classifier including the CNN structure and the training and testing procedure for the model when we have a new data set. This classification model will be an important component in the ECG analysis support software for physicians, medical professionals diagnosing cardiovascular disease, an urgent requirement of local health facilities.

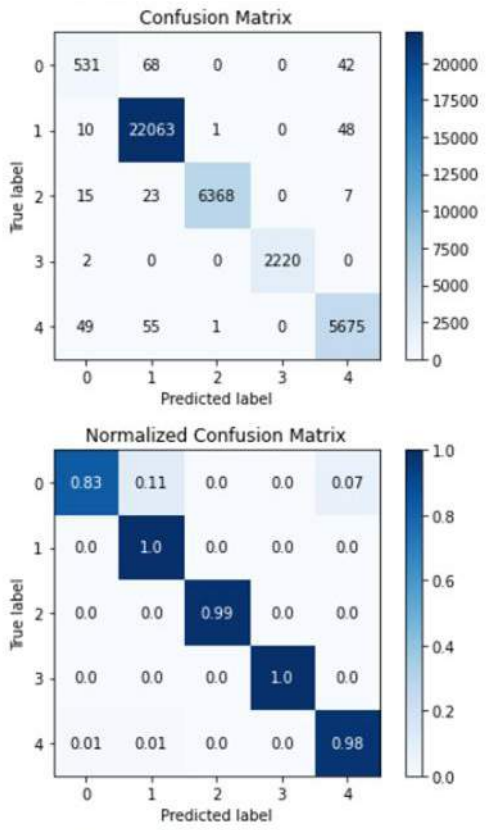

Figure 4. Confusion Matrix for training data

REFERENCES

1. K. I. Minami, H. Nakajima, T. Toyoshima. Real-time discrimination of ventricular tachyarrhythmia with Fourier-transform neural network, *IEEE Transaction on Bio-medical Engineering,* **1999**, 46, 179–185.

2. J. L. Willems, E. Lesaffre. Comparison of multigroup logistic and linear discriminant ecg and vcg classification, *Journal of Electrocardiology,* **1987**, 20, 83–92.

3. S. Osowski, L.T. Hoai, T. Markiewicz. Support vector machine based expert system for reliable heartbeat recognition, *IEEE Transaction on Bio-medical Engineering,* **2004**, 51, 582–589

4. R. Ceylan, Y. Ozbay. Comparison of FCM, PCA and WT techniques for classification ECG arrhythmias using artificial neural network. *Expert System and Applications*, **2007**, 33, 286–295.

5. A. Mustaqeem, S. M. Anwar, M. Majid. Multiclass classification of cardiac arrhythmia using improved feature selection and SVM invariants, *Computatinal and Mathematical Methods in Medicine,* **2018,** 1**,** 1-10.

6. O. T. Inan, L. Giovangrandi, G. T. Kovacs. Robust neural-network-based classification of premature ventricular contractions using wavelet transform and timing interval features, *IEEE Transaction on Bio-medical Engineering,* **2006**, 53, 2507–2515.

7. D. A. Coast, R. M. M. Stern, G. G. Cano, S. A. Briller, An approach to cardiac arrhythmia analysis using hidden markov models, *IEEE Transaction on Bio-medical Engineering,* **1990**, 37, 826–836.

8. L. Dehan, X. U. Guanggui, Z. Yuhua, H. G. Hosseini. Novel ECG diagnosis model based on multi-stage artificial neural networks, *Chinese Journal Science Instruments,* **2008**, 29, 27-38.

9. R. Ceylan, Y. Ozbay. Comparison of FCM, PCA and WT techniques for classification ECG arrhythmias using artificial neural network. *Expert System and Applications,* **2007**, 33, 286–295.

10. C. Salvatore, A. Cerasa, P. Battista, M. C. Gilardi, A. Quattrone, I. Castiglioni. Magnetic resonance imaging biomarkers for the early diagnosis of Alzheimer's disease: A machine learning approach, *Frontiers in Neuroscience,* **2015**, 9, 307-319.

11. S. Kiranyaz, T. Ince, M. Gabbouj. Real-time patient-specific ECG classification by 1-D convolutional neural networks, *IEEE Transaction on Bio-medical Engineering*, **2015**, 63, 664–675.

12. P. Rajpurkar, A. Y. Hannun, Haghpanahi. Cardiologist-level arrhythmia detection and classification in ambulatory electrocardiograms using a deep neural network, *Nature Medicine,* **2019**, 25, 65-69.

13. U. R. Acharya, S. L. Oh, Y. Hagiwara, J. H. Tan, M. Adam, A. Gertych, R. San Tan. A deep convolutional neural network model to classify heartbeats, *Computatinal and Mathematical Methods in Medicine,* **2017**, 89, 389–396.

14. G. B. Moody and R. G. Mark. The impact of the MIT-BIH arrhythmia database, *IEEE Engineering in Medicine and Biology Magazine*, **2001**, 20 (3), 45–50.

15. Kaggle, <https://www.kaggle.com/analiviafr/ecg-images?select=ecg_img>, Retrieved January 27, 2021.

16. B. B. Le Cun, J. S. Denker, D. Henderson, R. E. Howard, W. Hubbard, L. D. Jackel, *Handwritten digit recognition with a back-propagation network*, Proceedings of the Advances in Neural Information Processing Systems (NIPS), 1989, 396–404.

17. Y. LeCun, L. Bottou, Y. Bengio, P. Haffner. *Gradient-based learning applied to document recognition*, in: Proceedings of IEEE, 1998, 2278–2324.

18. R. Hecht-Nielsen. Theory of the backpropagation neural network, *Neural Networks 1* (Supplement-1), **1988**, 445–448.

19. X.-X. Niu, C. Y. Suen. A novel hybrid cnn–svm classifier for recognizing handwritten digits, *Pattern Recognition,* **2012,** *45*(4), 1318–1325.

20. O. Russakovsky, J. Deng, H. Su, J. Krause, S. Satheesh, S. Ma, Z. Huang, A. Karpathy, A. Khosla, M. Bernstein, et al. Imagenet large scale visual recognition challenge, *International Journal of Conflict and Violence* (IJCV), **2015**, *115*(3), 211–252.

21. C. Szegedy, W. Liu, Y. Jia, P. Sermanet, S. Reed, D. Anguelov, D. Erhan, V. Vanhoucke, A. Rabinovich. *Going deeper with convolutions*, in: Proceedings of the IEEE Conference on Computer Vision and Pattern Recognition (CVPR), 2015, 1–9.

22. M. D. Zeiler, R. Fergus. *Visualizing and understanding convolutional networks*, in: Proceedings of the European Conference on Computer Vision (ECCV), 2014, 818–833.

23. O. Russakovsky, J. Deng. ImageNet Large Scale Visual Recognition Challenge. *International Journal of Computer Vision,* **2015,** 115, 21-252.

24. K. He, X. Zhang, S. Ren, J. Sun. *Deep residual learning for image recognition*, Proceedings of the IEEE Conference on Computer Vision and Pattern Recognition (CVPR), 2016, 770–778.

25. A. Emelogu, S. Chowdhury, M. Marufuzzaman. An enhanced sample average approximation method for stochastic optimization, *International Journal of Production Economics,* **2016**, 182, 230-252.

26. J. Duchi, E. Hazan, Y. Singer. Adaptive subgradient methods for online learning and stochastic optimization, *Journal of Machine Learning Research*, **2011**, 12, 2121-2159.

27. R. Zhang, W. Gong, V. Grzeda, A. Yaworski. An adaptive learning rate method for improving adaptability of background models, *IEEE Signal Processing Letters*, **2013**, 20, 1266–1269.

28. K. Nguyen, C. Fookes. *Improving deep convolutional neural networks with unsupervised feature learning*, in: proceding of IEEE International Conference on Image Processing, 2015, 2270-2274.

29. A. Ullah, S.M. Anwar, M. Bilal, R.M. Mehmood. Classification of Arrhythmia by Using Deep Learning with 2-D ECG Spectral Image Representation, *Remote Sensing,* **2020**, *12*(10), 1685-1699.

https://doi.org/10.52111/qnjs.2021.15505

TẠP CHÍ KHOA HỌC
TRƯỜNG ĐẠI HỌC QUY NHƠN

Nghiên cứu lý thuyết sự hấp phụ sulfamethoxazole trên bề mặt rutile-TiO_2 (110) bằng phương pháp hóa học lượng tử

Nguyễn Ngọc Trí*, Nguyễn Tiến Trung

Phòng thí nghiệm Hóa học tính toán và Mô phỏng, Khoa Khoa học Tự nhiên, Trường Đại học Quy Nhơn, Việt Nam

Ngày nhận bài: 24/05/2021; Ngày nhận đăng: 20/07/2021

TÓM TẮT

Sự hấp phụ sulfamethoxazole (SMX) trên bề mặt rutile-TiO_2 (110) (r-TiO_2) được khảo sát bằng các tính toán hóa học lượng tử. Quá trình này được đánh giá là hấp phụ hóa học với năng lượng tương ứng khoảng 20 kcal.mol^{-1} cùng với sự hình thành các tương tác tĩnh điện O···Ti_{5f}. Các cấu trúc bền hình thành trong quá trình sắp xếp phân tử SMX lên trên bề mặt r-TiO_2 được phân tích chi tiết. Sự tồn tại và vai trò của các tương tác bề mặt trong quá trình tạo phức được làm rõ dựa trên các phân tích AIM và NBO. Đáng chú ý, sự tương tác khá mạnh giữa phân tử SMX với bề mặt r-TiO_2 tập trung tại nhóm >S=O và các vị trí Ti_{5f}. Các liên kết hydro kiểu N/C-H···O đóng vai trò bổ trợ trong việc làm bền các phức thu được.

Từ khóa: *Thuyết phiếm hàm mật độ, sulfamethoxazole, rutile-TiO_2 (110), bề mặt vật liệu.*

**Tác giả liên hệ chính.*
Email: nguyenngoctri@qnu.edu.vn

JOURNAL OF SCIENCE
QUY NHON UNIVERSITY

Theoretical study on adsorption of sulfamethoxazole on rutile-TiO_2 (110) surface using quantum chemical method

Nguyen Ngoc Tri*, Nguyen Tien Trung

Laboratory of Computational Chemistry and Modelling (LCCM), Faculty of Natural Sciences, Quy Nhon University

Received: 24/05/2021; Accepted: 20/07/2021

ABSTRACT

The adsorption of sulfamethoxazole (SMX) molecule on rutile-TiO_2 (110) surface (r-TiO_2) is examined by using quantum chemical computations. This process is evaluated as chemisorption with associated energies *ca.* 20 kcal.mol^{-1} and determined mainly by O···Ti_{5f} electrostatic interactions. The stable configurations are observed in detail following the arrangement of SMX on r-TiO_2. The existence and role of surface interactions are clarified by AIM and NBO analyses upon complexation. It is noticeable that the stable interactions between SMX and r-TiO_2 are mainly focused on >S=O groups and Ti_{5f} sites. The hydrogen bonds of the N/C-H···O_b type play an additional role in the stabilization of complexes.

Keywords: *DFT, sulfamethoxazole, rutile-TiO_2 (110), material surface.*

1. INTRODUCTION

Sulfamethoxazole (SMX) is one of the sulfonamide antibiotics and is widely used for bacterial infections. The overuse of SMX affected aquatic environments such as low quality and pollution because of their deposition, which can cause genetic mutations and the growth of organisms.[1-3] Many previous studies were performed with the aim to remove SMX and polluted compounds.[4-10] It is noted that nanomaterials based on chemical oxidation were remarkably applied in many cases, such as energy, health, and life sciences.[6] Recently, photocatalytic technologies have emerged as an efficient solution for water treatment. The semiconductor photocatalysts are primarily low-cost, non-toxic, and considered the most promising environmental protection materials.[6-8] Remarkably, TiO_2, regarded as one of the potential candidates, has been commonly used for many fields of photocatalysis and the environment. Among the phase surfaces of TiO_2, rutile-TiO_2 (110) (denoted by r-TiO_2) is the most stable surface and investigated widely on the removal of organic pollutants because of its exciting properties.[11-13] In previous reports, materials based on TiO_2 such as TiO_2-Fe, Bi_2O_3-TiO_2, TiO_2-zeolite were investigated for the removal of sulfonamides.[4-6] However, the formation and role of surface interactions between compounds containing > S=O functional groups such as SMX with material surfaces, especially TiO_2, have not yet been examined in detail. Moreover, investigations on the adsorption mechanism of

**Corresponding author.*
Email: nguyenngoctri@qnu.edu.vn

https://doi.org/10.52111/qnjs.2021.15506

substances on the r-TiO_2 have recently been of considerable interest because of their importance to understanding surface phenomena.[12-16] Hence, it is necessary to investigate the interaction between the SMX molecule and the r-TiO_2 to clarify intermolecular forces and their contributions to the adsorption process. This work provides a basic understanding of surface phenomena and the removal ability of SMX antibiotics by using semiconductor materials, especially TiO_2. Besides, quantum chemistry calculation is emerging as a highly efficient approach for evaluating the adsorption process as well as an understanding of characteristics of surface interactions.[12] In the present work, we use density functional theory (DFT) calculations to observe the adsorption of SMX on r-TiO_2.

2. COMPUTATIONAL METHOD

The structures of SMX and r-TiO_2 are considered from experimental data and then optimized by using the VASP program.[17] The stable configurations of adsorption of SMX on r-TiO_2 are obtained from density functional theory (DFT) calculations at PBE functional by VASP. The cut-off energy is considered at 500 eV with *2 x 2 x 1* k-points at the Gamma-centered grids. The force constant on the atoms and ions is set up at 0.01 meV for geometry optimization and energetic aspects computation. The unit cell is designed with dimensions size of *14.85 x 13.15 x 25.00* Å. The valence electron configurations used in the calculation are Ti $3d^24s^2$, O $2s^22p^4$, S $3s^23p^4$, N $2s^22p^5$, C $2s^22p^2$, H $1s^1$ implemented in the PAW pseudopotentials, respectively. The adsorption energy (E_{ads}), interaction energy (E_{int}), and deformation energies ($E_{def\text{-}mol}$, $E_{def\text{-}surf}$) are calculated as follows:

$$E_{ads} = E_{comp} - E_{mol} - E_{surf}; E_{int} = E_{comp} - E_{mol}^{\#} - E_{surf}^{\#}; E_{def\text{-}mol} = E_{mol}^{\#} - E_{mol}; E_{def\text{-}surf} = E_{surf}^{\#} - E_{surf}.$$

Where E_{comp}, E_{mol}, E_{surf} are energy values of optimized structures for complexes, SMX molecule, and r-TiO_2, respectively. The $E_{mol}^{\#}$, $E_{surf}^{\#}$ are the single-point energy values of molecule and surface part from the optimized complex. In addition, the formation of surface interactions and their role in the stability of complexes are analyzed using the atoms-in-molecules (AIM) and the natural bond orbital (NBO) approach. Topological geometries of stable structures are observed by the AIM2000 program at the B3LYP/6-31G(d,p) level of theory.[19] The electron density transfers between SMX and r-TiO_2 in complexes are calculated by the NBO5.G package integrated into Gaussian 03 program at the B3LYP/6-31G(d,p) level.[18,20]

3. RESULTS AND DISCUSSION

3.1. Geometrical structures

Using DFT calculations, four stable structures of the adsorbent-surface complexes between SMX and r-TiO_2 are observed, as displayed in Figure 1. The stability of complexes is mainly due to the interactions between functional groups, including > S=O, C/N-H in SMX and Ti_{5f} and O_b sites on the surface of r-TiO_2. This result is consistent with the trend of forming intermolecular interactions for adsorption of organic molecules on TiO_2 surfaces in previous studies.[12-16] Besides, the selected parameters for the formation of interactions upon complexation are listed in Table 1.

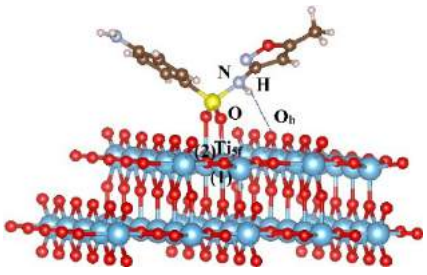

P1

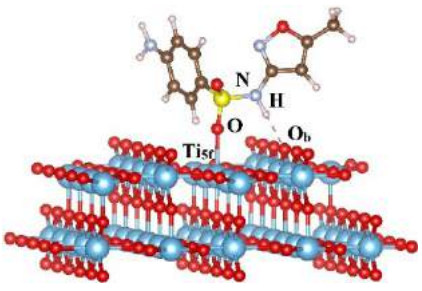

P2

https://doi.org/10.52111/qnjs.2021.15506

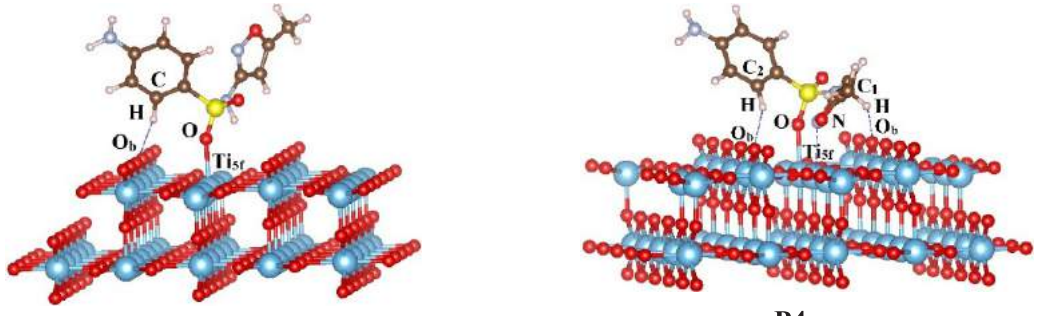

P3 P4

Figure 1. Optimized structures for adsorption of SMZ on r-TiO_2

Table 1. Some selected parameters of stable complexes in Figure 1 (distances (d) and change of bond length (Δr) in Å, angle (α) in °)

	d(Ti···O/N)	d(N/C-H···O)	α(S-O···Ti)	α(N/C-H···O)	Δr(S-O)	Δr(N/C-H)
P1	2.34(1)/2.31(2)	2.70	125.7-126.4	150.8	0.017-0.027	0.008
P2	2.25	1.87(3)/2.69(4)	171.4	177.1(3)/146.6(4)	0.023	0.017(3)/0.002(4)
P3	2.28	2.15(4)	160.2	155.4(4)	0.024	0.001(4)
P4	2.29(1)/3.38-3.10(2)	2.49-2.65(4)	164.8	112.1;103.3(4)	0.017	0.002-0.004(4)

((1), (2), (3), (4) for Ti···O, Ti···N, N-H (N-H···O), and C-H (C-H···O), respectively)

The calculated results show that the distances of Ti_{5f}···O, Ti_{5f}···N intermolecular interactions in the complexes are in the range of 2.25-2.34 Å and *ca.* 3.10 Å (Table 1), respectively. The Ti_{5f}···O contacts are close to the length of Ti-O bonds in the rutile phase (1.8-2.1 Å).[21] Besides, the H···O_b distances in complexes are *ca.* 1.87-2.70 Å, smaller than the total van der Waals radii of the H and O atoms (2.72 Å). Accordingly, the Ti_{5f}···O and H···O_b contacts are suggested in the adsorption configurations. Moreover, the change in length of S-O bonds of 0.017-0.027 Å is larger than that of C/N-H bonds (ca. 0.001-0.017 Å) upon complexation. The angles of S-O···Ti_{5f} and C/N-H···O_b following the interaction range from 125.7° to 164.8° and from 103.3° to 177.1°, respectively. The interaction distances and the changes in bond length as well as the contact angle in the configurations, are similar to previous studies on adsorption of organic molecules, antibiotics onto r-TiO_2.[12,13,22] Noticeably, the electrostatic interactions focus on > S=O and Ti_{5f} sites in the horizontal arrangement of SMX on r-TiO_2 as found in *ref. 22*. Furthermore, the elongation of > S=O bonds of 0.017-0.027 Å is slightly smaller than that of > C=O in the antibiotic molecules upon the adsorption process.[12,13,22] This result is due to the larger polarizability of > C=O compared to the > S=O group. Moreover, the calculated angles of S-O···Ti_{5f} range from 126 to 171°, slightly larger than that of C-O···Ti_{5f} (ca. 134-163°) upon complexation.[22]

3.2. Energetic aspects of the adsorption process

The energy components upon the adsorption of SMX on r-TiO_2 are calculated and gathered in Table 2. The adsorption energies (E_{ads}) of the complexes are quite negative, in the range of -12.8 to -20.4 kcal.mol^{-1} and increase in the ordering of **P1** < **P4** < **P2** < **P3**. In addition, the interaction energies of the complexes tend to change in the same order with E_{ads} values. Hence, **P1** is evaluated as the most stable configuration of adsorption of SMX on r-TiO_2, and the least stable one is **P3**. It can be found that two electrostatic interactions of Ti_{5f}···O (**P1**) or Ti_{5f}···O and Ti_{5f}···N (**P4**) are formed and contribute mainly to the stabilization of configurations. For the **P2**

https://doi.org/10.52111/qnjs.2021.15506

or **P3**, only one Ti_{5f}···O electrostatic interaction exists upon complexation. As a consequence, the electrostatic interactions such as Ti_{5f}···O and Ti_{5f}···N play an essential role in the significant strength of **P1**, **P4**. Besides, the adsorption of SMX on r-TiO_2 is slightly weaker than that for antibiotic molecules, which contain > C=O, -COOH groups.[12,22]

Table 2. Adsorption energy (E_{ads}), interaction energy (E_{int}), and deformation energies for molecule ($E_{d\text{-}mol}$), for surface ($E_{d\text{-}surf}$) following adsorption process (all in kcal.mol^{-1})

	P1	P2	P3	P4
E_{ads}	-20.4	-16.3	-12.8	-18.1
E_{int}	-29.8	-22.3	-18.0	-24.7
$E_{d\text{-}mol}$	3.3	1.1	1.1	1.9
$E_{d\text{-}surf}$	6.1	4.9	4.1	4.7

Deformation energy of molecule and material surface in adsorption process is an important factor in considering interaction ability and separation of the molecule on the material surface. As shown in Table 2, the deformation energy values for r-TiO_2 and SMX in the investigated configurations are in turn in the range of 4.1-6.1 kcal.mol^{-1}, and 1.1-3.3 kcal.mol^{-1}. This result indicates a stronger distortion of r-TiO_2 in comparison to SMX. The energy values in this work are slightly smaller than those in the configurations for the adsorption of molecules containing > C=O, -COOH, -NH_2, -OH functional groups on r-TiO_2.[12,13,22] As a result, the adsorption of SMX on the surface of r-TiO_2 causes smaller changes of the isolated geometries than in previous investigations.[12,13,22]

3.3. Topological geometry and electron density transfer

In order to have deep insight into the characteristics of surface interactions in the adsorption process, we performed calculations on topological geometry based on AIM theory and electron density transfers from the NBO approach. In these computations, the first layered structures of the configurations are considered due to the changes of geometrical, electronic structures, as well as their properties are mainly focused on the first layer of r-TiO_2.[12,13,22] The topological geometries for the investigated structures are displayed in Figure 2. The selected results of AIM analyses and the electron density transfers are given in Table 3.

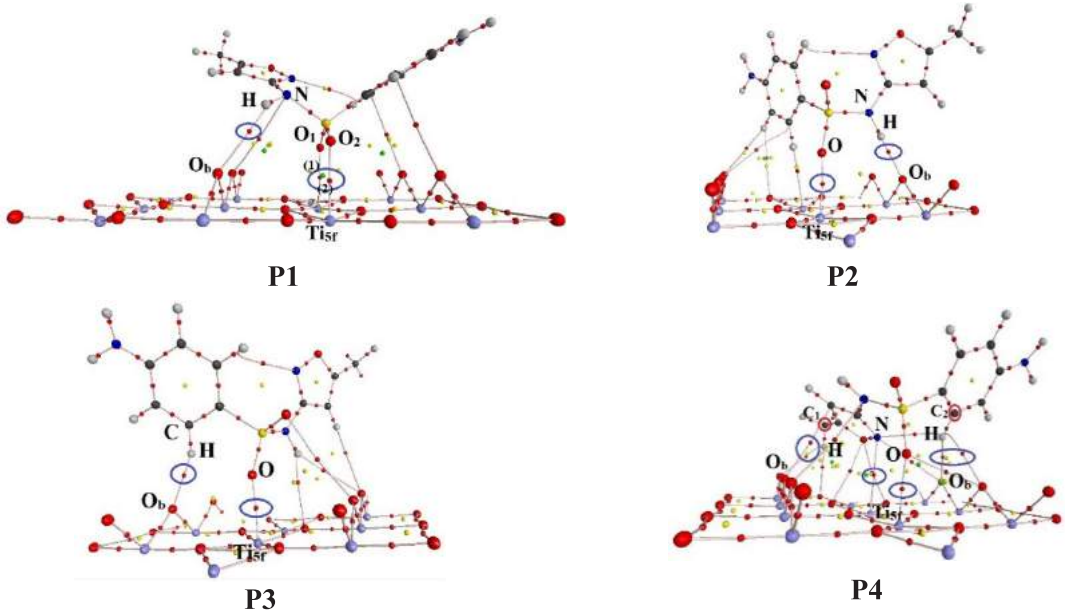

Figure 2. Topological geometries of the first-layered structures of the complexes

Table 3. Electron density (ρ(r), au), Laplacian (∇(ρ(r)), au), total electron density energy (H(r), au) at bond critical points (BCPs) and electron density transfers (EDT, e), intermolecular hyper-conjugative energy (E^2, kcal.mol^{-1}) in the first-layered structures of complexes

	BCPs	ρ(r)	∇(ρ(r))	H(r)	EDT	Transfers	E^2
P1	O···$Ti_{5f(1)}$	0.034	-0.041	0.004	0.21	n(O) → LP*(Ti), BD*(Ti-O)	11.68
	O···$Ti_{5f(2)}$	0.041	-0.056	0.001		n(O) → LP*(Ti), BD*(Ti-O)	19.55
	N-H···O_b	0.005	-0.005	0.001		n(O) → BD*(N-H)	0.87
P2	O···Ti_{5f}	0.043	-0.062	0.003	0.29	n(O) → LP*(Ti), BD*(Ti-O)	26.13
	N-H···O_b	0.029	-0.039	-0.001		n(O) → BD*(N-H)	10.55
P3	O···Ti_{5f}	0.040	-0.054	0.003	0.22	n(O) → LP*(Ti), BD*(Ti-O)	22.34
	C-H···O_b	0.018	-0.020	0.001		n(O) → BD*(C-H)	3.46
P4	O···Ti_{5f}	0.039	-0.053	0.003	0.26	n(O) → LP*(Ti), BD*(Ti-O)	21.85
	N···Ti_{5f}	0.012	-0.010	0.000		n(N) → LP*(Ti), BD*(Ti-O)	2.27
	C_1-H···O_b	0.010	-0.009	0.002		n(O) → BD*(C-H)	0.83
	C_2-H···O_b	0.011	-0.010	0.002		n(O) → BD*(C-H)	0.63

($^{(1),(2)}$ as shown in Figures 1 and 2)

Table 3 implies that the values of electron density (ρ(r)) at the bond critical points (BCPs) of Ti_{5f}···O, Ti_{5f}···N, H···O_b contacts range from 0.034 to 0.043 au, *ca.* 0.012 au and from 0.005 to 0.029 au, respectively. All values are within the range of non-covalent interactions.[19] Hence, these intermolecular interactions have non-covalent in nature. The slightly positive values of H(r) at the Ti_{5f}···O, Ti_{5f}···N, H···O_b BCPs imply further the non-covalent properties of these contacts, except for the H···O_b contact in **P2**. It is noteworthy that the Ti_{5f}···O/N interactions in the complexes have quite large ρ(r) values, implying their remarkable stability, and contribute considerably to the strength of complexes. Consequently, the **P1** and **P4** complexes are more stable than the **P2** and **P3** ones. The addition of the N-H···O_b hydrogen bond in the **P2** complex induces its higher stability relative to **P3**. These obtained results are in good agreement with the data taken from Table 2 and similar to the previous studies.[12,13,22] Moreover, the calculated results indicate that the ρ(r) values at O···Ti BCPs in **P1** are smaller than those in complexes of AP, AX, TC in *ref.22*. It is noted that in AP, AX, and TC systems, the important addition of O-H···O hydrogen bonds leads to the high stability the of complexes. As a result, the adsorption ability of SMZ on TiO_2 is weaker than that for AP, AX, TC.

The total electron density transfer (EDT) in the complexes is a characteristic for forming intermolecular interactions. As presented in Table 3, the EDT values are positive, implying the stronger electron density transfers from SMX to r-TiO_2 compared to the reverse transfers from r-TiO_2 to SMX. It is noted that the electron density transfers from the lone pairs of O in SMX (n(O) to the unoccupied lone pairs of Ti (n*(Ti)) and the anti-bonding orbitals (σ*(Ti-O)) are quite strong with the large hyper-conjugated energies (E^2) in the range of 12-26 kcal.mol^{-1}. These transfers are much stronger than the reverse ones from n(O) (in r-TiO_2) to σ*(N/C-H) (in SMX), which have E^2 values in the range of 1-11 kcal.mol^{-1}. Thus, it affirms that there exist the Ti_{5f}···O and H···O_b intermolecular interactions following complexation. The electron density transfer to form the Ti···N contact in **P4** is found with a small E^2 value of *ca.* 2 kcal.mol^{-1}. Besides, the formation of N-H···O_b hydrogen bond with a large E^2 value implying that it plays a considerably additional role in stabilizing **P2** in comparison

https://doi.org/10.52111/qnjs.2021.15506

to C-H···O in **P3**. The considerable transfers of electron density in **P1** with high values of E^2 lead to stable interactions as compared to that in the rest complexes. These are consistent with the trend of adsorption energy as analyzed above.

4. CONCLUSION

Four stable complexes for adsorption of the SMX molecule on the surface of r-TiO_2 were located at PBE functional. The calculated adsorption energy of the complexes is about 20 kcal.mol^{-1}. The stability of configurations is mainly contributed by the attractive electrostatic forces between the O atom of > S=O group (SMX) and the Ti_{5f} site (r-TiO_2) and an addition of the N/C-H···O hydrogen bonds. AIM analysis indicates that the interactions between > S=O···Ti_{5f} and N/C-H···O have non-covalent in nature. Furthermore, the NBO results show that the electron density transfers occur significantly from SMX to r-TiO_2. The obvious existence and significant importance of Ti_{5f}···O interaction contributing to the complexes' strength are determined by a high hyper-conjugated energy value of 26 kcal.mol^{-1}. The obtained results show that the adsorption process of SMX on the surface of r-TiO_2 is chemical adsorption.

Acknowledgement

This research is conducted within the framework of science and technology projects at the institutional level of Quy Nhon University under the project code T2020.659.07.

REFERENCES

1. K. Kümmerer. Antibiotics in the aquatic environment - A review - Part I, *Chemosphere*, **2009**, *75*, 417-434.
2. I. Michael, L. Rizzo, C. S. McArdell, C. M. Manaia, C. Merlin, T. Schwartz, C. Dagot and D. Fatta-Kassinos. Urban wastewater treatment plants as hotspots for the release of antibiotics in the environment: A review, *Water Research*, **2013**, *47*, 957-995.
3. J. Niu, L. Zhang, Y. Li, J. Zhao, S. Lv and K. Xiao. Effects of environmental factors on sulfamethoxazole photodegradation under simulated sunlight irradiation: Kinetics and mechanism, *Journal of Environmental Sciences*, **2013**, *25*, 1098-1106.
4. M. Ito, S. Fukahori, T. Fujiwara. Adsorptive removal and photocatalytic decomposition of sulfamethazine in secondary effluent using TiO_2–zeolite composites, *Environmental Science and Pollution Research*, **2014**, *21*, 834–842.
5. Y. Ma, K. Zhang, C. Li, T. Zhang and N. Gao. Oxidation of Sulfonamides in Aqueous Solution by UV-TiO_2-Fe(VI), *Hindawi BioMed Research International*, **2015**, *0*, 973942 (1-10).
6. N. Wang, X. Li, Y. Yang, Z. Zhou, Y. Shang, X. Zhuang. Photocatalytic degradation of sulfonamides by Bi_2O_3-TiO_2/PAC ternary composite: Mechanism, degradation pathway, *Journal of Water Process Engineering*, **2020**, *36*, 101335.
7. Y. F. Su, G. B. Wang, D. T. F. Kuo, M. L. Chang, Y. H. Shih. Photoelectrocatalytic degradation of the antibiotic sulfamethoxazole using TiO_2/Ti photoanode, *Applied Catalysis B: Environmental*, **2016**, *186*, 184–192.
8. S. Fukahori, T. Fujiwara. Photocatalytic decomposition behavior and reaction pathway of sulfamethazine antibiotic using TiO_2, *Journal of Environmental Management*, **2015**, *157*, 103–110.
9. A. Rodayan, R. Roy and V. Yargeau. Oxidation products of sulfamethoxazole in ozonated secondary effluent, *Journal of Hazardous Materials*, **2010**, *177*, 237-243.
10. W. Q. Guo, R. L. Yin, X. J. Zhou, J. S. Du, H. O. Cao, S. S. Yang and N. Q. Ren. Sulfamethoxazole degradation by ultrasound/ozone oxidation process in water: Kinetics, mechanisms, and pathways, *Ultrasonics Sonochemistry*, **2015**, *22*, 182-187.
11. C. Deiana et al. On the Simple Complexity of Carbon Monoxide on Oxide Surfaces: Facet-Specific Donation and Backdonation Effects Revealed on TiO_2 Anatase Nanoparticles, *ChemPhysChem*, **2016**, *7*, 1-6.

12. N. N. Tri, H. Q. Dai, N. T. Trung. Chemisorption of enrofloxacin on rutile-TiO_2 (110) surface: a theoretical investigation, *Vietnam Journal of Science and Technology*, **2019**, *57*(4), 449-456.

13. N. N. Tri, H. Q. Dai, N. T. Trung. Insight into the adsorption of organic molecules on rutile TiO_2 (110) surface: A theoretical study, *Vietnam Journal of Chemistry*, **2018**, *56*(6), 751-756.

14. M. Sowmiya and K. Senthilkumar. Adsorption of proline, hydroxyproline and glycine on anatase (001) surface: a first-principle study, *Theoretical Chemistry Accounts*, **2016**, *135*, 12.

15. X. Pan et al. A DFT study of gas molecules adsorption on the anatase (001) nanotube arrays, *Computational Materials Science*, **2013**, *67*, 174-181.

16. S. Manzhos, G. Giorgi and K. Yamashita. A Density Functiconal Tight Binding Study of Acetic acid adsorption on crystalline and amorphous surfaces of Titania, *Molecules*, **2015**, *20*, 3371-3388.

17. J. Hafner. Ab-Initio Simulations of Materials Using VASP: Density-Functional Theory and Beyond, *Journal of Computational Chemistry*, **2008**, *29*, 2044–2078.

18. M. J. Frisch et al. *Gaussian 09 (Revision B.01)*, Wallingford, CT: Gaussian, 2010.

19. R. F. W. Bader. *Atoms in molecules: A quantum theory*, Oxford: Oxford University Press, 1990.

20. F. Weinhold et al. *GenNBO 5.G*, Theoretical Chemistry Institute, University of Wisconsin: Madison, WI, 2001.

21. G. Cabailh, X. Torrelles, R. Lindsay, O. Bikondoa, I. Joumard, J. Zegenhagen, G. Thornton. Geometric structure of TiO_2 (110) (1x1): Achieving experimental consensus, *Physical Review B*, **2007**, *75*, 241403.

22. N. N. Tri, H. Q. Dai, A. J. P. Carvalho, M. T. Nguyen and N. T. Trung. Insights into adsorptive interactions between antibiotic molecules and rutile-TiO_2 (110) surface, *Surface Science*, **2021**, *703*, 121723(1-8).

https://doi.org/10.52111/qnjs.2021.15506

TẠP CHÍ KHOA HỌC
TRƯỜNG ĐẠI HỌC QUY NHƠN

Bài toán ước lượng lỗi H_∞ cho một lớp hệ có trễ sử dụng một phép biến đổi trạng thái mới

Đặng Thị Kiêm Hồng[1], Lê Bá Thông[2], Đinh Công Hướng[3,*]

[1] Khoa Hệ thống thông tin quản lý, Trường Đại học Tài chính - Kế toán, Quảng Ngãi, Việt Nam
[2] Khoa Khoa học Tự nhiên và Công nghệ, Trường Đại học Tây Nguyên, Đắk Lắk, Việt Nam
[3] Khoa Toán và Thống kê, Trường Đại học Quy Nhơn, Bình Định, Việt Nam

Ngày nhận bài: 29/06/2021, Ngày nhận đăng: 06/09/2021

TÓM TẮT

Trong bài báo này, chúng tôi nghiên cứu bài toán ước lượng lỗi H_∞ cho một lớp hệ có trễ với đầu vào không xác định. Đầu tiên, một phép biến đổi trạng thái mới được đề xuất để biến đổi hệ thống có trễ đang xét thành một hệ thống mới trong đó số hạng trễ liên quan đến véc tơ trạng thái được chuyển đến đầu ra và đầu vào của hệ thống. Sau đó, một bộ quan sát mới được thiết kế dựa trên thông tin đầu vào và đầu ra để giải quyết bài toán ước lượng lỗi H_∞. Sử dụng Bổ đề Kalman-Yakubovich-Popov tổng quát, các điều kiện đủ về sự tồn tại bộ quan sát ước lượng lỗi H_∞ được thiết lập và việc giải các ma trận quan sát đạt được quy về việc giải một tập các bất đẳng thức ma trận tuyến tính. Một ví dụ số được đưa ra để minh họa tính hiệu quả của phương pháp được đề xuất.

Từ khóa: *Hệ trễ thời gian, phép biến đổi trạng thái, bổ đề Kalman-Yakubovich-Popov tổng quát, ước lượng lỗi.*

**Tác giả liên hệ chính.*
Email: dinhconghuong@qnu.edu.vn

https://doi.org/10.52111/qnjs.2021.15507

JOURNAL OF SCIENCE
QUY NHON UNIVERSITY

H_∞ fault estimation problem for a class of time-delay systems using a new state transformation

Dang Thi Kiem Hong[1], Le Ba Thong[2], Dinh Cong Huong[3,*]

[1] *Faculty of Management Information Systems, University of Finance and Accounting, Quang Ngai, Vietnam*

[2] *Faculty of Natural Sciences and Technology, Tay Nguyen University, Dak Lak, Vietnam*

[3] *Faculty of Mathematics and Statistics, Quy Nhon University, Binh Dinh, Vietnam*

Received: 29/06/2021; Accepted: 06/09/2021

ABSTRACT

In this paper, we study the problem of H_∞ fault estimation for a class of time-delay systems with unknown inputs. First, a new state transformation is derived to transform the system into new coordinates where the delay term associated with the state vector is injected into the system output and input. Then, an observer-based H_∞ fault estimator with input and output injections is proposed for fault estimation. Based on the Generalized Kalman-Yakubovich-Popov Lemma, sufficient conditions on the existence of the H_∞ fault estimator are derived and a solution to the observer gain matrices is obtained by solving a set of linear matrix inequalities. A numerical example is given to illustrate the effectiveness of the proposed method.

Keywords: *Time-delay systems, state transformations, generalised Kalman-Yakubovich-Popov Lemma, fault estimation.*

1. INTRODUCTION AND MOTIVATIONS

Fault detection and isolation is widely required in various kinds of practical processes for safety purposes and hence has been extensively studied in the past three decades by many authors (see,[1–5] and the references therein).

As well-known, the time-delays are inherent in many real physical systems, such as chemical processes, long transmission lines in pneumatic systems, power and water distribution networks, air pollution systems, econometric systems, hydraulic and rolling mill systems. Since the delayed state is frequently the cause for instability and poor performance of systems,[6] much attention has been paid to the fault detection design problems of the linear state delayed systems and many significant results have been achieved (see, for example,[7–17]). An adaptive observer based fault estimator was used to estimate the abrupt constant fault.[8] An iterative learning observer was designed for fault estimation and accommodation for nonlinear time-delay systems.[12] A new performance index was introduced to design the reference model, and the fault detection filter design problem was formulated as the H_∞ model-matching problem.[13] However, the above-mentioned studies are characterized in the full frequency domain. While, in many practical systems, the faults usually emerge in the low frequency domain, for example, in aerospace-related fields (see, for instance,[18,19] and in industrial processes[20,21]).

The generalised Kalman-Yakubovich- Popov (GKYP) Lemma was established and, based on this, the equivalence between finite frequency domain inequality for a transfer function and a linear matrix inequality (LMI) was built.[22] The authors have proposed a GKYP-Lemma based approach to the fault detection and fault estimation in a finite frequency domain.[23] The robust fault detection problem in low frequency domain for linear time-delay systems was investigated.[24] The H_∞ filtering problem of discrete-time state-delayed systems with finite frequency specifications was considered.[25] Some results on

* *Corresponding author.*
Email: dinhconghuong@qnu.edu.vn

https://doi.org/10.52111/qnjs.2021.15507

H_∞ model reduction for continuous-time linear systems over finite frequency ranges were obtained.[26]

In recent years, the H_∞ problem of time-delay systems has attracted a lot of attention and many results have been reported in the literature (for instance,[27–29]). Based on the state transformation,[30] the authors[31] considered the problem of H_∞ fault estimation for a class of linear time-delay systems. Nevertheless, the existence conditions of the state transformations reported[30] are quite restrictive.[32,33] Thus, when the existence conditions[30] are not fulfilled, the methods reported[31] can not be applied. To support this statement, let us consider the following motivated fourth-order example,

$$\begin{aligned}\dot{x}(t) &= Ax(t)+A_1x(t-\tau_1)+A_2x(t-\tau_2)\\ &\quad +Bu(t)+B_dd(t)+B_ff(t),\ t\geq 0,\end{aligned} \tag{1}$$

$$y(t) = Cx(t)+D_dd(t)+D_ff(t), \tag{2}$$

$$\begin{aligned}x(t) &= \phi(t),\ t\in[-\tau,0),\\ &\quad \tau=\max\{\tau_1,\tau_2\},\end{aligned} \tag{3}$$

where $x(t)$ is the state vector, $u(t)$ is the control input vector, $y(t)$ is the output measurement vector, $\tau_1>0$ and $\tau_2>0$ are known constant time delays, $\phi(t)$ is a continuous initial function, $d(t)$ is the disturbance, $f(t)$ is the potential fault and

$$A=\begin{bmatrix}-1&-1&0&0\\1&1&0&0\\-2&-2&-3&-4\\-5&-5&0&0\end{bmatrix},$$

$$A_1=\begin{bmatrix}-1&-1&-1&-2\\-2&-2&-3&-3\\-4&0&-3&-5\\0&0&0&0\end{bmatrix},$$

$$A_2=\begin{bmatrix}-4&-4&0&0\\1&1&0&0\\-2&-2&3&4\\0&0&0&0\end{bmatrix}, B=\begin{bmatrix}1\\2\\3\\4\end{bmatrix},$$

$$B_d=\begin{bmatrix}0.1\\0.2\\0.3\\0.4\end{bmatrix},\ B_f=\begin{bmatrix}1.1\\1.2\\1.3\\1.4\end{bmatrix},$$

$$D_d=\begin{bmatrix}0.1\\0.2\end{bmatrix}, D_f=\begin{bmatrix}0.3\\0.4\end{bmatrix},$$

$$C=\begin{bmatrix}1&0&0&0\\0&1&0&0\end{bmatrix}.$$

Now, it is not hard to show that for the above example, the condition for the existence of a state transformation[30] (i.e., column unimodular) is not satisfied, and hence, the observer-based H_∞ fault estimator with input and output injections for fault estimation with known frequency range[31] can not be applied.

Motivated by the above discussions, in this paper, we consider the following class of time-delay systems with unknown inputs in finite frequency domain

$$\begin{aligned}\dot{x}(t) &= Ax(t)+\sum_{s=1}^{q}A_sx(t-\tau_s)+Bu(t)\\ &\quad +B_dd(t)+B_ff(t),\ t\geq 0,\end{aligned} \tag{4}$$

$$y(t) = Cx(t)+D_dd(t)+D_ff(t), \tag{5}$$

$$x(t) = \phi(t),\ t\in[-\tau,0),\ \tau=\max_{1\leq s\leq q}\tau_s, \tag{6}$$

where $x(t)\in\mathbb{R}^n$ is the state vector, $u(t)\in\mathbb{R}^m$ is the control input vector, $y(t)\in\mathbb{R}^p$ is the output measurement vector, $\tau_s>0$ $(s=1,2,\ldots,q)$ are known constant time delays, $\phi(t)$ is a continuous initial function, $d(t)\in\mathbb{R}^{n_d}$ is the disturbance, $f(t)\in\mathbb{R}^{n_f}$ is the potential fault, $d(t)$ and $f(t)$ are assumed to be L_2-norm bounded, matrices A, A_s $(s=1,2,\ldots,q)$, B, C, B_d, B_f, D_d and D_f are known constant and of appropriate dimensions.

The remainder of this paper is organized as follows. Section 2 proposes a novel state transformation for system (4)-(6). The problem of H_∞ fault estimation is studied in Section 3. Finally, a numerical example to demonstrate the obtained results is presented in Section 4.

Notations: For integer numbers $m,n,p,\ n>p$

and matrices $G \in \mathbb{R}^{m\times n}$, $H \in \mathbb{R}^{1\times n}$, we have the following notations:

• $n_z = n + p - 1$.

• M^T, M^*, $M^\perp$, M^+ denote the transpose, complex conjugate transpose, orthogonal complement and the Moore-Penrose-inverse, respectively.

• I_n denotes the identity matrix of size n, $0_{m,n}$ denotes the $m \times n$ zero matrix.

• $H = \begin{bmatrix} [H]_L & [H]_R \end{bmatrix}$, where $[H]_L \in \mathbb{R}^{1\times p}$, $[H]_R \in \mathbb{R}^{1\times(n-p)}$.

• $||\cdot||$ denotes the Euclidean vector norm of $(\cdot)$.

• L_2 is the space of square integrable functions over $[0,\infty)$ with $||\cdot||_{L_2} = \left(\int_0^\infty ||\cdot||^2 dt\right)^{\frac{1}{2}}$.

• $\sigma_{\max}(G)$ denotes maximum singular value of the transfer function matrix. H_∞ norm of a transfer function $G(s)$ over a finite frequency range $|w| \leqslant \bar{w}$ is defined as $||G(s)||_\infty^{[-\bar{w},\bar{w}]} = \sup \sigma_{\max}(G(iw))$, $\forall |w| \leqslant \bar{w}$.

2. STATE TRANSFORMATION

Let us assume that matrix C takes the following form

$$C = \begin{bmatrix} C_1 \\ \vdots \\ C_p \end{bmatrix} = \begin{bmatrix} I_p & 0_{p,n-p} \end{bmatrix}$$

and denote

$$\begin{aligned} M_i &= C_i, H_{is} = 0_{1,n},\ i = 1,\dots,p, \\ &\quad s = 1,\dots,q, \end{aligned} \tag{7}$$

$$M_j = M_{j-p}A - \sum_{k=1}^{p} \alpha_j^k M_k, \tag{8}$$

$$H_{js} = M_{j-p}A_s - \sum_{k=1}^{p} \beta_{js}^k M_k, \tag{9}$$

$$M_{i+1} = M_i A - \sum_{k=1}^{p} \alpha_{i+1}^k M_k, \tag{10}$$

$$H_{(i+1)s} = M_i A_s + H_{is}A - \sum_{k=1}^{p} \beta_{(i+1)s}^k M_k, \tag{11}$$

where α_j^k, β_{js}^k $(j = p+1,\dots,2p)$, α_{i+1}^k and $\beta_{(i+1)s}^k$ $(i = 2p,\dots,n_z-1)$ are scalars will be determined. Let us now propose the following change of coordinates:

$$\begin{aligned} z_i(t) &= M_i x(t) + \sum_{s=1}^{q} H_{is}x(t-\tau_s) \\ &\quad + \sum_{s=1}^{q}\Big(\sum_{j=1}^{p} \nu_{is}^j M_j\Big)x(t-2\tau_s), \\ &\quad i = 1,2,\dots,n_z,\ t \geqslant 2\tau, \end{aligned} \tag{12}$$

where $\nu_{is}^j = 0$ are scalars will be determined later.

Theorem 2.1. *For some scalars α_i^j, β_{is}^j, γ_ℓ^m, $\gamma_{n_z}^r$, ν_{ks}^j, $(i = p+1,p+2,\dots,n_z, j = 1,2,\dots,p,\ s = 1,2,\dots,q,\ \ell = p+1,p+2,\dots,2p-1,\ m = 1,2,\dots,2p,\ r = p+1,p+2,\dots,n_z,\ k = 2p+1,2p+2,\dots,n_z)$, if the following equations hold*

$$\Big[M_i A - \sum_{j=p+1}^{2p} \gamma_i^j M_j\Big]_R = 0_{1,n-p}, \tag{13}$$

$$\Big[M_i A_s + H_{is}A - \sum_{j=p+1}^{2p} \gamma_i^j H_{js}\Big]_R = 0_{1,n-p}, \tag{14}$$

$$\Big[H_{is}A_s\Big]_R = 0_{1,n-p}, \tag{15}$$

$$\Big[H_{is}A_s + \Big(\sum_{j=1}^{p} \nu_{is}^j M_j\Big)A\Big]_R = 0_{1,n-p}, \tag{16}$$

$$\Big[H_{it}A_m + H_{im}A_t\Big]_R = 0_{1,n-p}, \tag{17}$$

$$\Big[\Big(\sum_{j=1}^{p} \nu_{is}^j M_j\Big)A_\ell\Big]_R = 0_{1,n-p}, \tag{18}$$

$$\Big[M_{n_z}A - \sum_{j=p+1}^{n_z} \gamma_{n_z}^j M_j\Big]_R = 0_{1,n-p}, \tag{19}$$

$$\Big[M_{n_z}A_s + H_{n_z s}A - \sum_{j=p+1}^{n_z} \gamma_{n_z}^j H_{js}\Big]_R = 0_{1,n-p}, \tag{20}$$

then (12) transforms (4)-(6) into the following form

$$\begin{aligned} \dot{z}(t) &= \mathcal{A}z(t) + \mathcal{B}u(t) + \sum_{s=1}^{q} \mathcal{B}_s^1 u(t-\tau_s) \\ &\quad + \sum_{s=1}^{q} \mathcal{B}_s^2 u(t-2\tau_s) + \mathcal{B}_d d(t) \end{aligned}$$

https://doi.org/10.52111/qnjs.2021.15507

$$
\begin{aligned}
&+ \sum_{s=1}^{q} \mathcal{B}_{d_s}^1 d(t-\tau_s) + \sum_{s=1}^{q} \mathcal{B}_{d_s}^2 d(t-2\tau_s) \\
&+ \mathcal{B}_f f(t) + \sum_{s=1}^{q} \mathcal{B}_{f_s}^1 f(t-\tau_s) \\
&+ \sum_{s=1}^{q} \mathcal{B}_{f_s}^2 f(t-2\tau_s) + \Gamma y(t) \\
&+ \sum_{s=1}^{q} \Gamma_s^1 y(t-\tau_s) + \sum_{s=1}^{q} \Gamma_s^2 y(t-2\tau_s) \\
&+ \sum_{s=1}^{q} \Gamma_s^3 y(t-3\tau_s) + \sum_{s=1}^{q} \sum_{s\neq\ell=1}^{q} \Gamma_{s\ell}^{12} y(t-\tau_s-\tau_\ell) \\
&+ \sum_{s=1}^{q} \sum_{s\neq\ell=1}^{q} \Gamma_{s\ell}^{21} y(t-2\tau_s-\tau_\ell),\ t \geqslant 3\tau, \qquad (21)
\end{aligned}
$$

$$
y(t) = \mathcal{C}z(t) + D_d d(t) + D_f f(t), \qquad (22)
$$

where

$$
\mathcal{A} = \begin{bmatrix} 0_{p,p} & I_p & 0_{p,(n_z-2p)} \\ 0_{p-1,p} & \mathcal{A}_{n_z}^{22} & 0_{p-1,(n_z-2p)} \\ 0_{n_z-2p,p} & 0_{n_z-2p,p} & I_{n_z-2p} \\ 0_{1,p} & \mathcal{A}_{n_z}^{42} & \mathcal{A}_{n_z}^{43} \end{bmatrix},
$$

$$
\mathcal{C} = \begin{bmatrix} I_p & 0_{p,(n_z-p)} \end{bmatrix},
$$

$\mathcal{A}_{n_z}^{22} \in \mathbb{R}^{(p-1)\times p}$, $\mathcal{A}_{n_z}^{42} \in \mathbb{R}^{1\times p}$, $\mathcal{A}_{n_z}^{43} \in \mathbb{R}^{1\times(n_z-2p)}$, $\mathcal{B} \in \mathbb{R}^{n_z\times 1}$, $\mathcal{B}_s^1 \in \mathbb{R}^{n_z\times 1}$, $\mathcal{B}_s^2 \in \mathbb{R}^{n_z\times 1}$, $\mathcal{B}_d \in \mathbb{R}^{n_z\times 1}$, $\mathcal{B}_{d_s}^1 \in \mathbb{R}^{n_z\times 1}$, $\mathcal{B}_{d_s}^2 \in \mathbb{R}^{n_z\times 1}$, $\mathcal{B}_f \in \mathbb{R}^{n_z\times 1}$, $\mathcal{B}_{f_s}^1 \in \mathbb{R}^{n_z\times 1}$, $\mathcal{B}_{f_s}^2 \in \mathbb{R}^{n_z\times 1}$, $\Gamma \in \mathbb{R}^{n_z\times p}$, $\Gamma_s^1 \in \mathbb{R}^{n_z\times p}$, $\Gamma_s^2 \in \mathbb{R}^{n_z\times p}$, $\Gamma_s^3 \in \mathbb{R}^{n_z\times p}$ $(s = 1, 2, \ldots, q)$, $\Gamma_{s\ell}^{12} \in \mathbb{R}^{n_z\times p}$ *and* $\Gamma_{s\ell}^{21} \in \mathbb{R}^{n_z\times p}$ *are defined as below*

$$
\mathcal{A}_{n_z}^{22} = \begin{bmatrix} \gamma_{p+1}^{p+1} & \gamma_{p+1}^{p+2} & \cdots & \gamma_{p+1}^{2p} \\ \gamma_{p+2}^{p+1} & \gamma_{p+2}^{p+2} & \cdots & \gamma_{p+2}^{2p} \\ \vdots & \vdots & \cdots & \vdots \\ \gamma_{2p-1}^{p+1} & \gamma_{2p-1}^{p+2} & \cdots & \gamma_{2p-1}^{2p} \end{bmatrix},
$$

$$
\mathcal{A}_{n_z}^{42} = \begin{bmatrix} \gamma_{n_z}^{p+1} & \gamma_{n_z}^{p+2} & \cdots & \gamma_{n_z}^{2p} \end{bmatrix},
$$

$$
\mathcal{A}_{n_z}^{43} = \begin{bmatrix} \gamma_{n_z}^{2p+1} & \gamma_{n_z}^{2p+2} & \cdots & \gamma_{n_z}^{n_z} \end{bmatrix},
$$

$$
\mathcal{B} = \begin{bmatrix} M_1 B \\ M_2 B \\ M_3 B \\ \vdots \\ M_{n_z} B \end{bmatrix},\ \mathcal{B}_s^1 = \begin{bmatrix} 0_{p,1} \\ H_{(p+1)s} B \\ \vdots \\ H_{(n_z-1)s} B \\ H_{n_z s} B \end{bmatrix},
$$

$$
\mathcal{B}_s^2 = \begin{bmatrix} 0_{2p,1} \\ \left(\sum_{j=1}^{p} \nu_{(2p+1)s}^{j} M_j\right) B \\ \vdots \\ \left(\sum_{j=1}^{p} \nu_{n_z s}^{j} M_j\right) B \end{bmatrix},
$$

$$
\mathcal{B}_d = \begin{bmatrix} M_1 B_d \\ M_2 B_d \\ M_3 B_d \\ \vdots \\ M_{n_z} B_d \end{bmatrix},\ \mathcal{B}_{d_s}^1 = \begin{bmatrix} 0_{p,1} \\ H_{(p+1)s} B_d \\ \vdots \\ H_{(n_z-1)s} B_d \\ H_{n_z s} B_d \end{bmatrix},
$$

$$
\mathcal{B}_{d_s}^2 = \begin{bmatrix} 0_{2p,1} \\ \left(\sum_{j=1}^{p} \nu_{(2p+1)s}^{j} M_j\right) B_d \\ \vdots \\ \left(\sum_{j=1}^{p} \nu_{n_z s}^{j} M_j\right) B_d \end{bmatrix},
$$

$$
\mathcal{B}_f = \begin{bmatrix} M_1 B_f \\ M_2 B_f \\ M_3 B_f \\ \vdots \\ M_{n_z} B_f \end{bmatrix},\ \mathcal{B}_{f_s}^1 = \begin{bmatrix} 0_{p,1} \\ H_{(p+1)s} B_f \\ \vdots \\ H_{(n_z-1)s} B_f \\ H_{n_z s} B_f \end{bmatrix},
$$

$$
\mathcal{B}_{f_s}^2 = \begin{bmatrix} 0_{2p,1} \\ \left(\sum_{j=1}^{p} \nu_{(2p+1)s}^{j} M_j\right) B_f \\ \vdots \\ \left(\sum_{j=1}^{p} \nu_{n_z s}^{j} M_j\right) B_f \end{bmatrix},
$$

$$
\Gamma = \begin{bmatrix} \alpha_{p+1}^1 & \cdots & \alpha_{p+1}^p \\ \vdots & \cdots & \vdots \\ \alpha_{2p}^1 & \cdots & \alpha_{2p}^p \\ \Gamma(p+1,1) & \cdots & \Gamma(p+1,p) \\ \vdots & \cdots & \vdots \\ \Gamma(2p-1,1) & \cdots & \Gamma(2p-1,p) \\ \alpha_{2p+1}^1 & \cdots & \alpha_{2p+1}^p \\ \vdots & \cdots & \vdots \\ \alpha_{n_z}^1 & \cdots & \alpha_{n_z}^p \\ \Gamma(n_z,1) & \cdots & \Gamma(n_z,p) \end{bmatrix},
$$

where

$$
\begin{aligned}
\Gamma(i,j) &= \left[M_i A - \sum_{k=p+1}^{2p} \gamma_i^k M_k\right]_{Lj}, \\
\Gamma(n_z,j) &= \left[M_{n_z} A - \sum_{k=p+1}^{n_z} \gamma_{n_z}^k M_k\right]_{Lj}
\end{aligned}
$$

https://doi.org/10.52111/qnjs.2021.15507

$$\Gamma_s^1 = \begin{bmatrix} \beta^1_{(p+1)s} & \dots & \beta^p_{(p+1)s} \\ \vdots & \vdots & \dots \\ \beta^1_{(2p)s} & \dots & \beta^p_{(2p)s} \\ \Gamma^1_s(p+1,1) & \dots & \Gamma^1_s(p+1,p) \\ \vdots & \vdots & \vdots \\ \Gamma^1_s(2p-1,1) & \dots & \Gamma^1_s(2p-1,p) \\ \beta^1_{(2p+1)s} & \dots & \beta^p_{(2p+1)s} \\ \vdots & \dots & \vdots \\ \beta^1_{n_z s} & \dots & \beta^p_{n_z s} \\ \Gamma^1_s(n_z,1) & \dots & \Gamma^1_s(n_z,p) \end{bmatrix},$$

where

$$\Gamma^1_s(i,j) = \Big[M_i A_s + H_{is}A - \sum_{k=p+1}^{2p} \gamma_i^k H_{ks}\Big]_{Lj},$$

$$\Gamma^1_s(n_z,j) = \Big[M_{n_z} A_s + H_{n_z s}A - \sum_{k=p+1}^{n_z} \gamma_{n_z}^k H_{ks}\Big]_{Lj},$$

$$\Gamma_s^2 = \begin{bmatrix} 0_{p,1} & \dots & 0_{p,1} \\ \Big[H_{(p+1)s}A_s\Big]_{L1} & \dots & \Big[H_{(p+1)s}A_s\Big]_{Lp} \\ \vdots & \dots & \vdots \\ \Big[H_{(2p-1)s}A_s\Big]_{L1} & \dots & \Big[H_{(2p-1)s}A_s\Big]_{Lp} \\ \Gamma^2_s(2p,1) & \dots & \Gamma^2_s(2p,p) \\ \Gamma^2_s(2p+1,1) & \dots & \Gamma^2_s(2p+1,p) \\ \vdots & \dots & \vdots \\ \Gamma^2_s(n_z-1,1) & \dots & \Gamma^2_s(n_z-1,p) \\ \Gamma^2_s(n_z,1) & \dots & \Gamma^2_s(n_z,p) \end{bmatrix},$$

$$\Gamma^2_s(2p,j) = \Big[H_{(2p)s}A_s - \sum_{k=1}^{p} \nu^k_{(2p+1)s} M_k\Big]_{Lj},$$

$$\Gamma^2_s(i,j) = \Big[H_{is}A_s + \Big(\sum_{k=1}^{p} \nu^k_{is} M_k\Big)A - \sum_{k=1}^{p} \nu^k_{(i+1)s} M_k\Big]_{Lj},$$

$$\begin{aligned}\Gamma^2_s(n_z,j) = \Big[&H_{n_z s}A_s + \Big(\textstyle\sum_{k=1}^{p} \nu^k_{n_z s} M_k\Big)A \\ &-\gamma_{n_z}^{2p+1}\Big(\textstyle\sum_{k=1}^{p} \nu^k_{(2p+1)s} M_k\Big) - \dots \\ &-\gamma_{n_z}^{n_z}\Big(\textstyle\sum_{k=1}^{p} \nu^k_{n_z s} M_k\Big)\Big]_{Lj}, \\ &j = 1,2,\dots,p,\end{aligned}$$

$$\Gamma_s^3 = \begin{bmatrix} 0_{2p,1} \\ \Big[\Big(\sum_{k=1}^{p} \nu^k_{(2p+1)s} M_k\Big)A_s\Big]_{Lj} \\ \vdots \\ \Big[\Big(\sum_{k=1}^{p} \nu^k_{n_z s} M_k\Big)A_s\Big]_{Lj} \end{bmatrix}_{j=\overline{1,p}},$$

$$\Gamma^{12}_{s\ell} = \begin{bmatrix} 0_{p,p} \\ \Big[H_{(p+1)s}A_\ell\Big]_L \\ \Big[H_{(p+2)s}A_\ell\Big]_L \\ \vdots \\ \Big[H_{n_z s}A_\ell\Big]_L \end{bmatrix},$$

$$\Gamma^{21}_{s\ell} = \begin{bmatrix} 0_{2p,p} \\ \Big[\Big(\sum_{k=1}^{p} \nu^k_{(2p+1)s} M_k\Big)A_\ell\Big]_L \\ \Big[\Big(\sum_{k=1}^{p} \nu^k_{(2p+2)s} M_k\Big)A_\ell\Big]_L \\ \vdots \\ \Big[\Big(\sum_{k=1}^{p} \nu^k_{n_z s} M_k\Big)A_\ell\Big]_L \end{bmatrix}.$$

Proof. By taking the derivatives of (12), we obtain the following

$$\begin{aligned}
&\dot{z}_i(t) = M_i\dot{x}(t) \\
&= M_i(Ax(t) + \sum_{s=1}^{q} A_s x(t-\tau_s). \\
&+Bu(t) + B_d d(t) + B_f f(t)) \\
&= M_i Ax(t) + M_i \sum_{s=1}^{q} A_s x(t-\tau_s) \\
&+M_i Bu(t) + M_i B_d d(t) + M_i B_f f(t) \\
&= z_{i+p}(t) + \sum_{j=1}^{p} \alpha^j_{i+p} y_j(t) + \\
&+\sum_{s=1}^{q}\sum_{j=1}^{p} \beta^j_{(i+p)s} y_j(t-\tau_s) \\
&+M_i Bu(t) + M_i B_d d(t) \\
&+M_i B_f f(t), i = 1,\dots,p,
\end{aligned} \tag{23}$$

$$\begin{aligned}
&\dot{z}_i(t) = M_i\dot{x}(t) + \sum_{s=1}^{q} H_{is}\dot{x}(t-\tau_s) \\
&= M_i Ax(t) + \sum_{s=1}^{q}(M_i A_s + H_{is}A) \\
&\times x(t-\tau_s) + M_i Bu(t) \\
&+M_i B_d d(t) + M_i B_f f(t) \\
&+\sum_{s=1}^{q} H_{is}A_s x(t-2\tau_s) \\
&+\sum_{s=1}^{q} H_{is}\Big[\sum_{s\neq\ell=1}^{q} A_\ell x(t-\tau_s-\tau_\ell)\Big]
\end{aligned}$$

https://doi.org/10.52111/qnjs.2021.15507

$$+\sum_{s=1}^{q} H_{is}Bu(t-\tau_s)$$
$$+\sum_{s=1}^{q} H_{is}B_d d(t-\tau_s)+\sum_{s=1}^{q} H_{is}B_f f(t-\tau_s)$$
$$=\sum_{j=p+1}^{2p}\gamma_i^j z_j(t)+\Big[M_iA-\sum_{j=p+1}^{2p}\gamma_i^j M_j\Big]_L$$
$$\times[y_1(t)\quad y_2(t)\quad\dots\quad y_p(t)]^T$$
$$+\Big[\sum_{s=1}^{q} M_iA_s+H_{is}A-\sum_{j=p+1}^{2p}\gamma_i^j H_{js}\Big]_L$$
$$\times[y_1(t-\tau_s)\quad\dots\quad y_p(t-\tau_s)]^T$$
$$+\Big[\sum_{s=1}^{q} H_{is}A_s\Big]_L[y_1(t-2\tau_s)\dots\ y_p(t-2\tau_s)]^T$$
$$+\Big[\sum_{s=1}^{q}\sum_{s\neq\ell=1}^{q} H_{is}A_\ell\Big]_L[y_1(t-\tau_s-\tau_\ell)$$
$$y_2(t-\tau_s-\tau_\ell)\quad\dots\quad y_p(t-\tau_s-\tau_\ell)]^T$$
$$+M_iBu(t)+M_iB_dd(t)+M_iB_ff(t)$$
$$+\sum_{s=1}^{q} H_{is}Bu(t-\tau_s)+\sum_{s=1}^{q} H_{is}B_dd(t-\tau_s)$$
$$+\sum_{s=1}^{q} H_{is}B_ff(t-\tau_s),$$
$$i=p+1,\dots,2p-1, \tag{24}$$

$$\dot z_{2p}(t)=M_{2p}\dot x(t)+\sum_{s=1}^{q} H_{(2p)s}\dot x(t-\tau_s)$$
$$=z_{2p+1}(t)+\sum_{j=1}^{p}\alpha_{2p+1}^j y_j(t)$$
$$+\sum_{s=1}^{q}\sum_{j=1}^{p}\beta_{(2p+1)s}^j y_j(t-\tau_s)$$
$$+\Big[\sum_{s=1}^{q} H_{(2p)s}A_s-\Big(\sum_{j=1}^{p}\nu_{(2p+1)s}^j M_j\Big)\Big]_L$$
$$\times[y_1(t-2\tau_s)\ \dots\ y_p(t-2\tau_s)]^T$$
$$+\Big[\sum_{s=1}^{q}\sum_{s\neq\ell=1}^{q} H_{(2p)s}A_\ell\Big]_L[y_1(t-\tau_s-\tau_\ell)$$
$$\dots y_p(t-\tau_s-\tau_\ell)]^T$$
$$+M_{2p}Bu(t)+M_{2p}B_dd(t)+M_{2p}B_ff(t)$$
$$+\sum_{s=1}^{q} H_{(2p)s}Bu(t-\tau_s)$$
$$+\sum_{s=1}^{q} H_{(2p)s}B_dd(t-\tau_s)$$
$$+\sum_{s=1}^{q} H_{(2p)s}B_ff(t-\tau_s), \tag{25}$$

$$\dot z_i(t)=M_i\dot x(t)+\sum_{s=1}^{q} H_{is}\dot x(t-\tau_s)$$
$$+\sum_{s=1}^{q}\Big(\sum_{j=1}^{p}\nu_{is}^j M_j\Big)\dot x(t-2\tau_s)$$
$$=M_iAx(t)+\sum_{s=1}^{q}(M_iA_s+H_{is}A)x(t-\tau_s)$$
$$+\sum_{s=1}^{q}(H_{is}A_s+\sum_{j=1}^{p}\nu_{is}^j M_j)Ax(t-2\tau_s)$$
$$+\sum_{s=1}^{q}\Big(\sum_{j=1}^{p}\nu_{is}^j M_j\Big)A_sx(t-3\tau_s)$$
$$+\sum_{s=1}^{q} H_{is}\Big[\sum_{s\neq\ell=1}^{q} A_\ell x(t-\tau_s-\tau_\ell)\Big]$$
$$+\sum_{s=1}^{q}\Big(\sum_{j=1}^{p}\nu_{is}^j M_j\Big)\Big[\sum_{s\neq\ell=1}^{q} A_\ell x(t-2\tau_s-\tau_\ell)\Big]$$
$$+M_iBu(t)+M_iB_dd(t)+M_iB_ff(t)$$
$$+\sum_{s=1}^{q} H_{is}Bu(t-\tau_s)$$
$$+\sum_{s=1}^{q} H_{is}B_dd(t-\tau_s)$$
$$+\sum_{s=1}^{q} H_{is}B_ff(t-\tau_s)$$
$$+\sum_{s=1}^{q}\Big(\sum_{j=1}^{p}\nu_{is}^j M_j\Big)Bu(t-2\tau_s)$$
$$+\sum_{s=1}^{q}\Big(\sum_{j=1}^{p}\nu_{is}^j M_j\Big)B_dd(t-2\tau_s)$$
$$+\sum_{s=1}^{q}\Big(\sum_{j=1}^{p}\nu_{is}^j M_j\Big)B_ff(t-2\tau_s). \tag{26}$$

From (10)-(11), we have for $i=2p,\ 2p+1,\dots,n_z-1$,

$$M_iAx(t)=M_{i+1}x(t)+\sum_{j=1}^{p}\alpha_{i+1}^j y_j(t), \tag{27}$$

$$(M_iA_s + H_{is}A)x(t-\tau_s) = H_{(i+1)s}x(t-\tau_s) + \sum_{j=1}^{p}\beta^j_{(j+1)s}y_j(t-\tau_s),\ s=1,2,\dots,q. \quad (28)$$

Substituting (27)-(28) into (26) and using (15) - (18), we obtain

$$\begin{aligned}
\dot{z}_i(t) &= z_{i+1}(t) + \sum_{j=1}^{p}\alpha^j_{i+1}y_j(t) \\
&+ \sum_{s=1}^{q}\sum_{j=1}^{p}\beta^j_{(i+1)s}y_j(t-\tau_s) + \Bigg[\sum_{s=1}^{q}H_{is}A_s \\
&+ \Big(\sum_{j=1}^{p}\nu^j_{is}M_j\Big)A - \Big(\sum_{j=1}^{p}\nu^j_{(i+1)s}M_j\Big)\Bigg]_L \\
&[y_1(t-2\tau_s) \quad \dots \quad y_p(t-2\tau_s)]^T \\
&+\Big[\sum_{s=1}^{q}\Big(\sum_{j=1}^{p}\nu^j_{is}M_j\Big)A_s\Big]_L[y_1(t-3\tau_s) \\
&y_2(t-3\tau_s) \quad \dots \quad y_p(t-3\tau_s)]^T \\
&+\Big[\sum_{s=1}^{q}\sum_{s\neq\ell=1}^{q}H_{is}A_\ell\Big]_L[y_1(t-\tau_s-\tau_\ell) \\
&\ y_2(t-\tau_s-\tau_\ell) \quad \dots \quad y_p(t-\tau_s-\tau_\ell)]^T \\
&+\Big[\sum_{s=1}^{q}\sum_{s\neq\ell=1}^{q}\Big(\sum_{j=1}^{p}\nu^j_{is}M_j\Big)A_\ell\Big]_L \\
&\times[y_1(t-2\tau_s-\tau_\ell) \ \dots \ y_p(t-2\tau_s-\tau_\ell)]^T \\
&+M_iBu(t) + M_iB_dd(t) + M_iB_ff(t) \\
&+\sum_{s=1}^{q}H_{is}Bu(t-\tau_s) + \sum_{s=1}^{q}H_{is}B_dd(t-\tau_s) \\
&+\sum_{s=1}^{q}H_{is}B_ff(t-\tau_s) + \sum_{s=1}^{q}\Big(\sum_{j=1}^{p}\nu^j_{is}M_j\Big) \\
&Bu(t-2\tau_s) + \sum_{s=1}^{q}\Big(\sum_{j=1}^{p}\nu^j_{is}M_j\Big)B_dd(t-2\tau_s) \\
&+\sum_{s=1}^{q}\Big(\sum_{j=1}^{p}\nu^j_{is}M_j\Big)B_ff(t-2\tau_s), \\
&i = 2p+1,\dots,n_z-1. \qquad (29)
\end{aligned}$$

From (26), we have

$$\begin{aligned}
\dot{z}_{n_z}(t) &= M_{n_z}Ax(t) \\
&+\sum_{s=1}^{q}(M_{n_z}A_s + H_{n_zs}A)x(t-\tau_s) \\
&+\sum_{s=1}^{q}(H_{n_zs}A_s + \sum_{j=1}^{p}\nu^j_{n_zs}M_j)A)x(t-2\tau_s) \\
&+\sum_{s=1}^{q}\Big(\sum_{j=1}^{p}\nu^j_{n_zs}M_j\Big)A_sx(t-3\tau_s) \\
&+\sum_{s=1}^{q}H_{n_zs}\Big[\sum_{s\neq\ell=1}^{q}A_\ell x(t-\tau_s-\tau_\ell)\Big] \\
&+\sum_{s=1}^{q}\Big(\sum_{j=1}^{p}\nu^j_{n_zs}M_j\Big)\Big[\sum_{s\neq\ell=1}^{q}A_\ell x(t-2\tau_s-\tau_\ell)\Big] \\
&+M_{n_z}Bu(t) + M_{n_z}B_dd(t) + M_{n_z}B_ff(t) \\
&+\sum_{s=1}^{q}H_{n_zs}Bu(t-\tau_s) + \sum_{s=1}^{q}H_{n_zs}B_dd(t-\tau_s) \\
&+\sum_{s=1}^{q}H_{n_zs}B_ff(t-\tau_s) \\
&+\sum_{s=1}^{q}\Big(\sum_{j=1}^{p}\nu^j_{n_zs}M_j\Big)Bu(t-2\tau_s) \\
&+\sum_{s=1}^{q}\Big(\sum_{j=1}^{p}\nu^j_{n_zs}M_j\Big)B_dd(t-2\tau_s) \\
&+\sum_{s=1}^{q}\Big(\sum_{j=1}^{p}\nu^j_{n_zs}M_j\Big)B_ff(t-2\tau_s). \qquad (30)
\end{aligned}$$

From conditions (19)- (20), equation (30) becomes

$$\begin{aligned}
\dot{z}_{n_z}(t) &= \sum_{j=p+1}^{n_z}\gamma^j_{n_z}z_j(t) + M_{n_z}Bu(t) \\
&+M_{n_z}B_dd(t) + M_{n_z}B_ff(t) \\
&+\sum_{s=1}^{q}H_{n_zs}Bu(t-\tau_s) \\
&+\sum_{s=1}^{q}H_{n_zs}B_dd(t-\tau_s) \\
&+\sum_{s=1}^{q}H_{n_zs}B_ff(t-\tau_s) \\
&+\sum_{s=1}^{q}\Big(\sum_{j=1}^{p}\nu^j_{n_zs}M_j\Big)Bu(t-2\tau_s) \\
&+\sum_{s=1}^{q}\Big(\sum_{j=1}^{p}\nu^j_{n_zs}M_j\Big)B_dd(t-2\tau_s) \\
&+\sum_{s=1}^{q}\Big(\sum_{j=1}^{p}\nu^j_{n_zs}M_j\Big)B_ff(t-2\tau_s)
\end{aligned}$$

https://doi.org/10.52111/qnjs.2021.15507

$$
\begin{aligned}
&+\Big[M_{n_z}A-\sum_{j=p+1}^{n_z}\gamma_{n_z}^{j}M_j\Big]_L[y_1(t)\quad\dots\quad y_p(t)]^T\\
&+\Big[\sum_{s=1}^{q}M_{n_z}A_s+H_{n_zs}A-\sum_{j=p+1}^{n_z}\gamma_{n_z}^{j}H_{js}\Big]_L\\
&[y_1(t-\tau_s)\quad y_2(t-\tau_s)\quad\dots\quad y_p(t-\tau_s)]^T\\
&+\Bigg[\sum_{s=1}^{q}H_{n_zs}A_s+\Big(\sum_{j=1}^{p}\nu_{n_zs}^{j}M_j\Big)A\\
&-\sum_{j=p+1}^{n_z}\gamma_{n_z}^{j}\Big(\sum_{k=1}^{p}\nu_{js}^{k}M_k\Big)\Bigg]_L\\
&\times[y_1(t-2\tau_s)\quad\dots\quad y_p(t-2\tau_s)]^T\\
&+\Big[\sum_{s=1}^{q}\Big(\sum_{j=1}^{p}\nu_{n_zs}^{j}M_j\Big)A_s\Big]_L[y_1(t-3\tau_s)\\
&\dots\quad y_p(t-3\tau_s)]^T\\
&+\Big[\sum_{s=1}^{q}\sum_{s\neq\ell=1}^{q}H_{n_zs}A_\ell\Big]_L[y_1(t-\tau_s-\tau_\ell)\\
&y_2(t-\tau_s-\tau_\ell)\dots\quad y_p(t-\tau_s-\tau_\ell)]^T\\
&+\Big[\sum_{s=1}^{q}\sum_{s\neq\ell=1}^{q}\Big(\sum_{j=1}^{p}\nu_{n_zs}^{j}M_j\Big)A_\ell\Big]_L\\
&[y_1(t-2\tau_s-\tau_\ell)\quad\dots\quad y_p(t-2\tau_s-\tau_\ell)]^T.
\end{aligned}
$$

Finally, (23)-(25), (29) and (31) can now be expressed in the form (21)-(22). This completes the proof of Theorem 2.1.

In the following, we will solve unknowns in Theorem 2.1. For this, we first express (13)-(18) into the following compact form:

$$\chi_{n_z}X_{n_z}=Y_{n_z},\tag{31}$$

where

$$
\begin{aligned}
\chi_{n_z}&=\begin{bmatrix}\chi_{n_z}^{1}&\chi_{n_z}^{2}&\dots&\chi_{n_z}^{p+2}\end{bmatrix},\\
X_{n_z}&=\begin{bmatrix}X_{n_z}^{1}&X_{n_z}^{2}&\dots&X_{n_z}^{p+2}\end{bmatrix}^T,\\
Y_{n_z}&=\begin{bmatrix}Y_{n_z}^{1}&\dots&Y_{n_z}^{p+q-1}&Y_{n_z}^{p+q}\end{bmatrix},
\end{aligned}
$$

where, $\chi_{n_z}^{i}$, $X_{n_z}^{i}$ $(i=1,2,\dots,p+2)$ are as defined below

$$\chi_{n_z}^{1}=\begin{bmatrix}\chi_{n_z}^{11}&\chi_{n_z}^{12}\end{bmatrix},\tag{32}$$

$$
\begin{aligned}
\chi_{n_z}^{11}&=\begin{bmatrix}\alpha_{p+1}^{1}&\dots&\alpha_{p+1}^{p}\\ \gamma_{p+1}^{p+1}&\dots&\gamma_{p+1}^{2p}\end{bmatrix},\\
\chi_{n_z}^{12}&=\begin{bmatrix}\beta_{(p+1)1}^{1}&\dots&\beta_{(p+1)1}^{p}&\beta_{(p+1)2}^{1}&\dots\\ \beta_{(p+1)2}^{p}\dots&\beta_{(p+1)q}^{1}&\dots&\beta_{(p+1)q}^{p}\end{bmatrix},\\
\chi_{n_z}^{2}&=\begin{bmatrix}\chi_{n_z}^{21}&\chi_{n_z}^{22}\end{bmatrix},
\end{aligned}\tag{33}
$$

$$
\begin{aligned}
\chi_{n_z}^{21}&=\begin{bmatrix}\alpha_{p+2}^{1}&\dots&\alpha_{p+2}^{p}\\ \dots&\gamma_{p+2}^{p+1}&\dots&\gamma_{p+2}^{2p}\end{bmatrix},\\
\chi_{n_z}^{12}&=\begin{bmatrix}\beta_{(p+2)1}^{1}&\dots&\beta_{(p+2)1}^{p}&\dots\\ \beta_{(p+2)q}^{1}&\dots&\beta_{(p+2)q}^{p}\end{bmatrix},\\
&\vdots\\
\chi_{n_z}^{p-1}&=\begin{bmatrix}\chi_{n_z}^{(p-1)1}&\chi_{n_z}^{(p-1)2}\end{bmatrix},
\end{aligned}\tag{34}
$$

$$
\begin{aligned}
\chi_{n_z}^{(p-1)1}&=\begin{bmatrix}\alpha_{2p-1}^{1}&\dots&\alpha_{2p-1}^{p}\\ \gamma_{2p-1}^{p+1}&\dots&\gamma_{2p-1}^{2p}\end{bmatrix},\\
\chi_{n_z}^{(p-1)2}&=\begin{bmatrix}\beta_{(2p-1)1}^{1}&\dots&\beta_{(2p-1)1}^{p}\\ \dots&&\beta_{(2p-1)q}^{1}\\ \dots&\beta_{(2p-1)q}^{p}&\end{bmatrix},
\end{aligned}
$$

$$\chi_{n_z}^{p}=\begin{bmatrix}\chi_{n_z}^{p(2p)}&\chi_{n_z}^{p(2p+1)}&\dots&\chi_{n_z}^{pn_z}\end{bmatrix},\tag{35}$$

$$
\begin{aligned}
\chi_{n_z}^{p(2p)}&=\begin{bmatrix}\beta_{(2p)1}^{1}&\dots&\beta_{(2p)1}^{p}\\ \dots&\beta_{(2p)q}^{1}&\\ \dots&\beta_{(2p)q}^{p}&\end{bmatrix},\\
\chi_{n_z}^{p(2p+1)}&=\begin{bmatrix}\beta_{(2p+1)1}^{1}&\dots&\\ \beta_{(2p+1)1}^{p}&&\\ \dots&\beta_{(2p+1)q}^{1}\dots&\\ \beta_{(2p+1)q}^{p}&&\end{bmatrix},\\
&\vdots\\
\chi_{n_z}^{pn_z}&=\begin{bmatrix}\beta_{n_z1}^{1}&\dots&\beta_{n_z1}^{p}&\\ &\dots&\beta_{n_zq}^{1}&\dots&\beta_{n_zq}^{p}\end{bmatrix},
\end{aligned}
$$

$$
\chi_{n_z}^{p+1}=\begin{bmatrix}\alpha_{2p}^{1}&\alpha_{2p}^{2}&\dots\\ \alpha_{2p}^{p}&\dots&\alpha_{n_z-1}^{1}\\ \alpha_{n_z-1}^{2}&\dots&\alpha_{n_z-1}^{p}\end{bmatrix},\tag{36}
$$

$$
\chi_{n_z}^{p+2}=\begin{bmatrix}\chi_{n_z(2p+1)}^{p+2}&&\\ \chi_{n_z(2p+2)}^{p+2}&\dots&\chi_{n_zn_z}^{p+2}\end{bmatrix},\tag{37}
$$

$$\chi^{p+2}_{n_z(2p+1)} = \begin{bmatrix} \nu^1_{(2p+1)1} & \nu^2_{(2p+1)1} \\ \cdots & \nu^1_{(2p+1)q} \\ \cdots & \nu^p_{(2p+1)q} \end{bmatrix},$$

$$\chi^{p+2}_{n_z(2p+2)} = \begin{bmatrix} \nu^1_{(2p+2)1} & \nu^2_{(2p+2)1} \\ \cdots & \nu^p_{(2p+2)1} \\ \cdots & \nu^1_{(2p+2)q} \\ \cdots & \nu^p_{(2p+2)q} \end{bmatrix},$$

$$\vdots$$

$$\chi^{p+2}_{n_z n_z} = \begin{bmatrix} \nu^1_{n_z 1} & \nu^2_{n_z 1} & \cdots & \nu^p_{n_z 1} & \cdots \\ \nu^1_{n_z q} & \nu^2_{n_z q} & \cdots & \nu^p_{n_z q} \end{bmatrix},$$

$$X^1_{n_z} = \begin{bmatrix} X^1_{n_z 1} & X^1_{n_z 2} \end{bmatrix}, \tag{38}$$

$$X^1_{n_z 1} = \begin{bmatrix} X^{11}_{n_z} & 0_{p(q+2),\frac{(q+2)(q+1)}{2}(n-p)} \\ \cdots & 0_{p(q+2),\frac{(q+2)(q+1)}{2}(n-p)} \end{bmatrix},$$

$$X^1_{n_z 2} = \begin{bmatrix} X^{11}_{n_z 2} & X^{12_2}_{n_z 2} & \cdots & X^{12_q}_{n_z 2} \\ 0_{p(q+2),(n_z-2p)q^2(n-p)} \end{bmatrix},$$

$$X^{11}_{n_z 2} = 0_{p(q+2),(n_z-2p+1)q(n-p)},$$

$$X^{12_2}_{n_z 2} = 0_{p(q+2),(n_z-2p+1)(q-1)(n-p)},$$

$$\ldots,$$

$$X^{12_q}_{n_z 2} = 0_{p(q+2),(n_z-2p+1)(n-p)},$$

$$\vdots$$

$$X^{p-1}_{n_z} = \begin{bmatrix} X^{p-1}_{n_z 1} & X^{p-1}_{n_z 2} \end{bmatrix}, \tag{39}$$

$$X^{p-1}_{n_z 1} = \begin{bmatrix} 0_{p(q+2),\frac{(q+2)(q+1)}{2}(n-p)} \\ 0_{p(q+2),\frac{(q+2)(q+1)}{2}(n-p)} & \cdots & X^{11}_{n_z} \end{bmatrix},$$

$$X^{p-1}_{n_z 2} = \begin{bmatrix} X^{(p-1)1}_{n_z 2} & X^{(p-1)2_2}_{n_z 2} & \cdots \\ X^{(p-1)2_q}_{n_z 2} & 0_{p(q+2),(n_z-2p)q^2(n-p)} \end{bmatrix},$$

$$X^{(p-1)1}_{n_z 2} = 0_{p(q+2),(n_z-2p+1)q(n-p)},$$

$$X^{(p-1)2_2}_{n_z 2} = 0_{p(q+2),(n_z-2p+1)(q-1)(n-p)},$$

$$\ldots,$$

$$X^{(p-1)2_q}_{n_z 2} = 0_{p(q+2),(n_z-2p+1)(n-p)},$$

$$X^p_{n_z} = \begin{bmatrix} X^p_{n_z 1} & X^p_{n_z 2} \end{bmatrix}, \tag{40}$$

$$X^p_{n_z 1} = \begin{bmatrix} 0_{(n_z-2p+1)pq,\frac{(q+2)(q+1)}{2}(n-p)} \\ 0_{(n_z-2p+1)pq,\frac{(q+2)(q+1)}{2}(n-p)} & \cdots \\ 0_{(n_z-2p+1)pq,\frac{(q+2)(q+1)}{2}(n-p)} \end{bmatrix},$$

$$X^p_{n_z 2} = \begin{bmatrix} X^{pp}_{n_z} & X^{p(p+1)_2}_{n_z} & \cdots & X^{p(p+1)_q}_{n_z} \\ 0_{(n_z-2p+1)pq,(n_z-2p)q^2(n-p)} \end{bmatrix},$$

$$X^{p+1}_{n_z} = \begin{bmatrix} X^{p+1}_{n_z 1} & X^{p+1}_{n_z 2} \end{bmatrix}, \tag{41}$$

$$X^{p+1}_{n_z 1} = \begin{bmatrix} 0_{(n_z-2p)p,\frac{(q+2)(q+1)}{2}(n-p)} & \cdots \\ 0_{(n_z-2p)p,\frac{(q+2)(q+1)}{2}(n-p)} \end{bmatrix},$$

$$X^{p+1}_{n_z 2} = \begin{bmatrix} X^{(p+1)p}_{n_z} & X^{(p+1)(p+1)_2}_{n_z} & \cdots \\ X^{(p+1)(p+1)_q}_{n_z} & 0_{(n_z-2p)p,(n_z-2p)q^2(n-p)} \end{bmatrix},$$

$$X^{p+2}_{n_z} = \begin{bmatrix} X^{p+2}_{n_z(2p+1)1} & X^{p+2}_{n_z(2p+1)2} \\ X^{p+2}_{n_z(2p+2)1} & X^{p+2}_{n_z(2p+2)2} \\ \vdots & \vdots \\ X^{p+2}_{n_z n_z 1} & X^{p+2}_{n_z n_z 2} \end{bmatrix}, \tag{42}$$

$$X^{p+2}_{n_z(2p+1)1} = \begin{bmatrix} 0_{pq,\frac{(q+2)(q+1)}{2}(n-p)} \\ \cdots & 0_{pq,\frac{(q+2)(q+1)}{2}(n-p)} \end{bmatrix},$$

$$\vdots$$

$$X^{p+2}_{n_z n_z 1} = \begin{bmatrix} 0_{pq,\frac{(q+2)(q+1)}{2}(n-p)} & , \\ \cdots & 0_{pq,\frac{(q+2)(q+1)}{2}(n-p)} \end{bmatrix},$$

$$X^{p+2}_{n_z(2p+1)2} = \begin{bmatrix} X^{(p+2)p}_{n_z(2p+1)2} & , \\ \cdots & X^{(p+2)(p+1)_q}_{n_z(2p+1)2} \quad X^{(p+2)(p+2)}_{n_z(2p+1)2} \end{bmatrix},$$

$$X^{p+2}_{n_z(2p+2)2} = \begin{bmatrix} X^{(p+3)p}_{n_z(2p+2)2} & X^{(p+3)(p+1)_2}_{n_z(2p+2)2} \\ \cdots & X^{(p+3)(p+1)_q}_{n_z(2p+2)2} \quad X^{(p+3)(p+2)}_{n_z(2p+2)2} \end{bmatrix},$$

$$\vdots$$

$$X^{p+2}_{n_z n_z 2} = \begin{bmatrix} X^{np}_{n_z n_z 2} & X^{n(p+1)_2}_{n_z n_z 2} & , \\ \cdots & X^{n(p+1)_q}_{n_z n_z 2} \quad X^{n(p+2)}_{n_z n_z 2} \end{bmatrix},$$

where

$$X^{11}_{n_z} \in \mathbb{R}^{p(q+2)\times\frac{(q+2)(q+1)}{2}(n-p)},$$

$$X^{i(p+1)_\ell}_{n_z j 2} = 0_{pq,(n_z-2p+1)(q-\ell+1)(n-p)},$$

$$i = p+2,\ldots,n,\ j = 2p+1,\ldots,n_z,$$

$$\ell = 2,3,\ldots,q,$$

https://doi.org/10.52111/qnjs.2021.15507

$$X_{n_z}^{pp} \in \mathbb{R}^{(n_z-2p+1)pq\times(n_z-2p+1)q(n-p)},$$
$$X_{n_z}^{p(p+1)_\ell} \in \mathbb{R}^{(n_z-2p+1)pq\times(n_z-2p+1)(q-\ell+1)(n-p)},$$
$$\ell = 2,3,\ldots,q,$$
$$X_{n_z}^{(p+1)(p+1)_\ell} \in \mathbb{R}^{(n_z-2p)p\times(n_z-2p+1)(q-\ell+1)(n-p)},$$
$$\ell = 2,3,\ldots,q,$$
$$X_{n_z}^{(p+1)p} \in \mathbb{R}^{(n_z-2p)p\times(n_z-2p+1)q(n-p)},$$
$$X_{n_zj2}^{ip} \in \mathbb{R}^{pq\times(n_z-2p+1)q(n-p)},$$
$$i = p+2,\ldots,n,\ j = 2p+1,\ldots,n_z,$$
$$X_{n_zj2}^{i(p+2)} \in \mathbb{R}^{pq\times(n_z-2p)q^2(n-p)},$$
$$i = p+2,\ldots,n,\ j = 2p+1,\ldots,n_z$$

are defined as below

$$X_{n_z}^{11} = \begin{bmatrix} X_{n_z1}^{11} & X_{n_z2}^{11} \end{bmatrix}, \quad (43)$$

where

$$X_{n_z1}^{11} = \begin{bmatrix} \sum & 0_{2p,q(n-p)} & 0_{2p,(q-1)(n-p)} \\ \Delta & \Omega^1 & \Phi_1^1 \end{bmatrix},$$

$$X_{n_z2}^{11} = \begin{bmatrix} 0_{2p,(q-2)(n-p)} & \cdots & 0_{2p,n-p} \\ \Phi_2^1 & \cdots & \Phi_{q-1}^1 \end{bmatrix}$$

$$X_{n_z}^{pp} = \begin{bmatrix} X_{n_z1}^{pp} & X_{n_z2}^{pp} \end{bmatrix}, \quad (44)$$

where

$$X_{n_z1}^{pp} = \begin{bmatrix} \Omega^1 & \Omega^2 \\ 0_{pq,q(n-p)} & \Omega^1 \\ 0_{pq,q(n-p)} & 0_{pq,q(n-p)} \\ \vdots & \vdots \\ 0_{pq,q(n-p)} & 0_{pq,q(n-p)} \end{bmatrix},$$

$$X_{n_z2}^{pp} = \begin{bmatrix} \Omega^3 & \ldots & \Omega^{n_z-2p+1} \\ \Omega^2 & \ldots & \Omega^{n_z-2p} \\ \Omega^1 & \ldots & \Omega^{n_z-2p-1} \\ \vdots & \ddots & \vdots \\ 0_{pq,q(n-p)} & \ldots & \Omega^1 \end{bmatrix},$$

$$X_{n_z}^{p(p+1)_l} = \begin{bmatrix} X_{n_z1}^{p(p+1)_l} & X_{n_z2}^{p(p+1)_l} \end{bmatrix}, \quad (45)$$

where

$$X_{n_z1}^{p(p+1)_l} = \begin{bmatrix} \Phi_{\ell-1}^1 & \Phi_{\ell-1}^2 \\ 0_{pq,(q-\ell+1)(n-p)} & \Phi_{\ell-1}^1 \\ 0_{pq,(q-\ell+1)(n-p)} & 0_{pq,(q-\ell+1)(n-p)} \\ \vdots & \vdots \\ 0_{pq,(q-\ell+1)(n-p)} & 0_{pq,(q-\ell+1)(n-p)} \end{bmatrix},$$

$$X_{n_z2}^{p(p+1)_l} = \begin{bmatrix} \Phi_{\ell-1}^3 & \ldots & \Phi_{\ell-1}^{n_z-2p+1} \\ \Phi_{\ell-1}^2 & \ldots & \Phi_{\ell-1}^{n_z-2p} \\ \Phi_{\ell-1}^1 & \ldots & \Phi_{\ell-1}^{n_z-2p-1} \\ \vdots & \ddots & \vdots \\ 0_{pq,(q-\ell+1)(n-p)} & \ldots & \Phi_{\ell-1}^1 \end{bmatrix},$$

$$X_{n_z}^{(p+1)p} = \begin{bmatrix} X_{n_z1}^{(p+1)p} & X_{n_z2}^{(p+1)p} \end{bmatrix}, \quad (46)$$

where

$$X_{n_z1}^{(p+1)p} = \begin{bmatrix} 0_{p,q(n-p)} & \Xi^1 \\ 0_{p,q(n-p)} & 0_{p,q(n-p)} \\ \vdots & \vdots \\ 0_{p,q(n-p)} & 0_{p,q(n-p)} \end{bmatrix},$$

$$X_{n_z2}^{(p+1)p} = \begin{bmatrix} \Xi^2 & \ldots & \Xi^{n_z-2p} \\ \Xi^1 & \ldots & \Xi^{n_z-2p-1} \\ \vdots & \ddots & \vdots \\ 0_{p,q(n-p)} & \ldots & \Xi^1 \end{bmatrix},$$

$$X_{n_z}^{(p+1)(p+1)} = \begin{bmatrix} X_{n_z1}^{(p+1)(p+1)} & X_{n_z2}^{(p+1)(p+1)} \end{bmatrix}, \quad (47)$$

where

$$X_{n_z1}^{(p+1)(p+1)} = \begin{bmatrix} 0_{p,(q-\ell+1)(n-p)} & \Psi_{\ell-1}^1 \\ 0_{p,(q-\ell+1)(n-p)} & 0_{p,(q-\ell+1)(n-p)} \\ \vdots & \vdots \\ 0_{p,(q-\ell+1)(n-p)} & 0_{p,(q-\ell+1)(n-p)} \end{bmatrix},$$

$$X_{n_z2}^{(p+1)(p+1)} = \begin{bmatrix} \Psi_{\ell-1}^2 & \ldots & \Psi_{\ell-1}^{n_z-2p} \\ \Psi_{\ell-1}^1 & \ldots & \Psi_{\ell-1}^{n_z-2p-1} \\ \vdots & \ddots & \vdots \\ 0_{p,(q-\ell+1)(n-p)} & \ldots & \Psi_{\ell-1}^1 \end{bmatrix},$$

https://doi.org/10.52111/qnjs.2021.15507

$$X_{n_z}^{(p+2)p} = \left[\begin{array}{cc} X_{n_z1}^{(p+2)p} & X_{n_z2}^{(p+2)p} \end{array}\right], \quad (48)$$

where

$$X_{n_z}^{(p+2)p} = \left[\begin{array}{c} X_{n_z(2p+1)2}^{(p+2)p} \\ X_{n_z(2p+2)2}^{(p+3)p} \\ \vdots \\ X_{n_zn_z2}^{np} \end{array}\right]$$

$$X_{n_z1}^{(p+2)p} = \left[\begin{array}{cc} 0_{pq,q(n-p)} & \nabla \\ 0_{pq,q(n-p)} & 0_{pq,q(n-p)} \\ \vdots & \vdots \\ 0_{pq,q(n-p)} & 0_{pq,q(n-p)} \end{array}\right],$$

$$X_{n_z2}^{(p+2)p} = \left[\begin{array}{ccc} 0_{pq,q(n-p)} & \cdots & 0_{pq,q(n-p)} \\ \nabla & \cdots & 0_{pq,q(n-p)} \\ \vdots & \ddots & \vdots \\ 0_{pq,q(n-p)} & \cdots & \nabla \end{array}\right],$$

$$X_{n_z}^{(p+2)(p+2)} = \left[\begin{array}{cc} X_{n_z1}^{(p+2)(p+2)} & X_{n_z2}^{(p+2)(p+2)} \end{array}\right], \quad (49)$$

$$X_{n_z}^{(p+2)(p+2)} = \left[\begin{array}{c} X_{n_z(2p+1)2}^{(p+2)(p+2)} \\ X_{n_z(2p+2)2}^{(p+3)(p+2)} \\ \vdots \\ X_{n_zn_z2}^{n(p+2)} \end{array}\right],$$

$$X_{n_z1}^{(p+2)(p+2)} = \left[\begin{array}{cc} \Pi & 0_{pq,q^2(n-p)} \\ 0_{pq,q^2(n-p)} & \Pi \\ \vdots & \vdots \\ 0_{pq,q^2(n-p)} & 0_{pq,q^2(n-p)} \end{array}\right],$$

$$X_{n_z2}^{(p+2)(p+2)} = \left[\begin{array}{cc} \cdots & 0_{pq,q^2(n-p)} \\ \cdots & 0_{pq,q^2(n-p)} \\ \ddots & \vdots \\ \cdots & \Pi \end{array}\right].$$

In (32), $Y_{n_z}^i \in \mathbb{R}^{1\times(2q+1+\frac{q(q-1)}{2})(n-p)}$ $(i = 1,2,\ldots,p-1)$, $Y_{n_z}^p \in \mathbb{R}^{1\times((n-p)^2q}$, $Y_{n_z}^{p+1} \in \mathbb{R}^{1\times(n-p)^2(q-1)}$, $Y_{n_z}^{p+2} \in \mathbb{R}^{1\times(n-p)^2(q-2)}$, ..., $Y_{n_z}^{(p+q-1)} \in \mathbb{R}^{1\times(n-p)^2}$, $Y_{n_z}^{p+q} = 0_{1,q^2(n_z-2p)(n-p)}$ are defined as follows

$$Y_{n_z}^i = \left[\begin{array}{cc} Y_{n_z1}^i & Y_{n_z2}^i \end{array}\right], \quad (50)$$

where

$$Y_{n_z1}^i = \left[\begin{array}{cccc} X_i^2 & \bar{Y}_{i1}^1 & \ldots & \bar{Y}_{iq}^1 \\ Y_{i1}^1 & \ldots & Y_{iq}^1 & \end{array}\right]$$

$$Y_{n_z2}^i = \left[\begin{array}{ccc} Z_{i,12}^1 & \cdots & Z_{i,1q}^1 \\ Z_{i,23}^1 & \ldots & Z_{i,(q-1)q}^1 \end{array}\right],$$

for $i = 1,2,\ldots,p-1$,

$$Y_{n_z}^p = \left[\begin{array}{cccc} Y_{n_z}^{p1} & Y_{n_z}^{p2} & \ldots & Y_{n_z}^{p(n-p)} \end{array}\right], \quad (51)$$

$$Y_{n_z}^{p1} = \left[\begin{array}{cccc} Y_{p1}^1 & Y_{p2}^1 & \ldots & Y_{pq}^1 \end{array}\right],$$

$$Y_{n_z}^{p2} = \left[\begin{array}{cccc} Y_{p1}^2 & Y_{p2}^2 & \ldots & Y_{pq}^2 \end{array}\right],$$

$$\vdots$$

$$Y_{n_z}^{p(n-p)} = \left[\begin{array}{cccc} Y_{p1}^{n-p} & Y_{p2}^{n-p} & \ldots & Y_{pq}^{n-p} \end{array}\right],$$

$$Y_{n_z}^{p+1} = \left[\begin{array}{cccc} Y_{n_z}^{(p+1)1} & \ldots & Y_{n_z}^{(p+1)(n-p)} \end{array}\right], \quad (52)$$

$$Y_{n_z}^{(p+1)1} = \left[\begin{array}{ccc} Z_{p,12}^1 & \cdots & Z_{p,1q}^1 \end{array}\right],$$

$$Y_{n_z}^{(p+1)2} = \left[\begin{array}{ccc} Z_{p,12}^2 & \cdots & Z_{p,1q}^2 \end{array}\right],$$

$$\vdots$$

$$Y_{n_z}^{(p+1)(n-p)} = \left[\begin{array}{ccc} Z_{p,12}^{n-p} & \cdots & Z_{p,1q}^{n-p} \end{array}\right],$$

$$Y_{n_z}^{p+2} = \left[\begin{array}{cccc} Y_{n_z}^{(p+2)1} & \ldots & Y_{n_z}^{(p+2)(n-p)} \end{array}\right], \quad (53)$$

$$Y_{n_z}^{(p+2)1} = \left[\begin{array}{cccc} Z_{p,23}^1 & Z_{p,24}^1 & \cdots & Z_{p,2q}^1 \end{array}\right],$$

$$\vdots$$

$$Y_{n_z}^{(p+2)(n-p)} = \left[\begin{array}{ccc} Z_{p,23}^{n-p} & \cdots & Z_{p,2q}^{n-p} \end{array}\right],$$

$$\vdots$$

$$Y_{n_z}^{p+q-1} = \left[\begin{array}{cccc} Y_{n_z}^{(p+q-1)1} & \ldots & Y_{n_z}^{(p+q-1)(n-p)} \end{array}\right], \quad (54)$$

$$Y_{n_z}^{(p+q-1)1} = Z_{p,(q-1)q}^1,$$

$$Y_{n_z}^{(p+q-1)2} = Z_{p,(q-1)q}^2,$$

$$\vdots$$

$$Y_{n_z}^{(p+q-1)(n-p)} = Z_{p,(q-1)q}^{n-p}.$$

https://doi.org/10.52111/qnjs.2021.15507

From (31), a solution for χ_{n_z} exists if and only if

$$\text{rank}\begin{bmatrix} X_{n_z} \\ Y_{n_z} \end{bmatrix} = \text{rank}\begin{bmatrix} X_{n_z} \end{bmatrix}. \tag{55}$$

Next, we express (19)-(20) into the following form

$$\zeta_{n_z} Z_{n_z} = T_{n_z}, \tag{56}$$

where

$$\zeta_{n_z} = \begin{bmatrix} \alpha_{n_z}^1 & \dots & \alpha_{n_z}^p & \gamma_{n_z}^{p+1} & \dots & \gamma_{n_z}^{n_z} \end{bmatrix}, \tag{57}$$

$$Z_{n_z} = \begin{bmatrix} Z_{n_z1} & Z_{n_z2} & Z_{nz3} & \dots & Z_{nz4} \end{bmatrix}, \tag{58}$$

$$Z_{n_z1} = \begin{bmatrix} \mathcal{X} \\ \mathcal{X} \\ Z_{n_z}^1(2p+1, n-p) \\ Z_{n_z}^1(2p+2, n-p) \\ \vdots \\ Z_{n_z}^1(n_z-1, n-p) \\ Z_{n_z}^1(n_z, n-p) \end{bmatrix},$$

$$Z_{n_z2} = \begin{bmatrix} \overline{\mathcal{X}}_1^1 \\ \overline{\mathcal{X}}_1^1 \\ Z_{n_z}^2(2p+1, n-p) \\ Z_{n_z}^2(2p+2, n-p) \\ \vdots \\ Z_{n_z}^2(n_z-1, n-p) \\ Z_{n_z}^2(n_z, n-p) \end{bmatrix},$$

$$Z_{n_z3} = \begin{bmatrix} \overline{\mathcal{X}}_2^1 \\ \overline{\mathcal{X}}_2^1 \\ Z_{n_z}^3(2p+1, n-p) \\ Z_{n_z}^3(2p+2, n-p) \\ \vdots \\ Z_{n_z}^3(n_z-1, n-p) \\ Z_{n_z}^3(n_z, n-p) \end{bmatrix},$$

$$Z_{n_z4} = \begin{bmatrix} \overline{\mathcal{X}}_q^1 \\ \overline{\mathcal{X}}_q^1 \\ Z_{n_z}^{q+1}(2p+1, n-p) \\ Z_{n_z}^{q+1}(2p+2, n-p) \\ \vdots \\ Z_{n_z}^{q+1}(n_z-1, n-p) \\ Z_{n_z}^{q+1}(n_z, n-p) \end{bmatrix},$$

$$T_{n_z} = \begin{bmatrix} T_{n_z}^1 & T_{n_z}^2 & T_{n_z}^3 & \dots & T_{n_z}^{q+1} \end{bmatrix}. \tag{59}$$

In (58)-(59), $T_{n_z}^s$ and $Z_{n_z}^s(k, n-1)$ $(s = 2, 3, \dots, q+1)$, $(k = 2p+1, 2p+2, \dots, n_z)$ are defined as follows

$$T_{n_z}^1 = X_p^{n_z-2p+2} - \sum_{j=1}^{p}\Big(\alpha_{2p}^j X_j^{n_z-2p+1} + \alpha_{2p+1}^j X_j^{n_z-2p} + \dots + \alpha_{n_z-2}^j X_j^3 + \alpha_{n_z-1}^j X_j^2\Big), \tag{60}$$

$$T_{n_z}^s = \bar{Y}_{p(s-1)}^{n_z-2p+1} - \sum_{j=1}^{p}\Big(\alpha_{2p}^j \bar{Y}_{j(s-1)}^{n_z-2p} + \alpha_{2p+1}^j \bar{Y}_{j(s-1)}^{n_z-2p-1} + \dots + \alpha_{n_z-1}^j \bar{Y}_{j(s-1)}^1 + \beta_{(2p+1)(s-1)}^j X_j^{n_z-2p} + \dots + \beta_{n_z(s-1)}^j X_j^1\Big), \tag{61}$$

$$Z_{n_z}^1(k, n-p) = X_p^{k-2p+1} - \sum_{j=1}^{p}\Big(\alpha_{2p}^j X_j^{k-2p} + \alpha_{2p+1}^j X_j^{k-2p-1} + \dots + \alpha_{k-1}^j X_j^1\Big), \tag{62}$$

$$Z_{n_z}^s(k, n-p) = \bar{Y}_{p(s-1)}^{k-2p} - \sum_{j=1}^{p}\Big(\alpha_{2p}^j \bar{Y}_{j(s-1)}^{k-2p-1} + \alpha_{2p+1}^j \bar{Y}_{j(s-1)}^{k-2p-2} + \dots + \alpha_{k-1}^j \bar{X}_{j(s-1)}^1 + \beta_{(2p+1)(s-1)}^j X_j^{k-2p-1} + \dots + \beta_{(k-1)(s-1)}^j X_j^1\Big). \tag{63}$$

Since Z_{n_z} and T_{n_z} are two known constant matrices, it follows form (56) that, a solution for

ζ_{n_z} always exists if and only if

$$\text{rank}\begin{bmatrix} Z_{n_z} \\ T_{n_z} \end{bmatrix} = \text{rank}\begin{bmatrix} Z_{n_z} \end{bmatrix}. \quad (64)$$

Algorithm 1

Step 1: Check if condition (55) is satisfied or not. If so, obtain $\chi_{n_z} = Y_{n_z} X_{n_z}^{+}$.

Step 2: Substitute β_{ks}^{j} and α_{ℓ}^{j} into (58)-(59) and obtain Z_{n_z} and T_{n_z}. Check if condition (64) is satisfied or not. If so, obtain $\zeta_{n_z} = T_{n_z} Z_{n_z}^{+}$.

Step 4: From (7)-(11), obtain the state transformation (12) and (21)-(22).

3. THE DESIGN OF FAULT ESTIMATOR

Consider the following observer-based fault detection filter

$$\begin{aligned}
\dot{\hat{z}}(t) &= \mathcal{A}\hat{z}(t) + \mathcal{B}u(t) + \sum_{s=1}^{q} \mathcal{B}_s^1 u(t-\tau_s) \\
&+ \sum_{s=1}^{q} \mathcal{B}_s^2 u(t-2\tau_s) + \Gamma y(t) \\
&+ \sum_{s=1}^{q} \Gamma_s^1 y(t-\tau_s) + \sum_{s=1}^{q} \Gamma_s^2 y(t-2\tau_s) \\
&+ \sum_{s=1}^{q} \Gamma_s^3 y(t-3\tau_s) \\
&+ \sum_{s=1}^{q} \sum_{s\neq\ell=1}^{q} \Gamma_{s\ell}^{12} y(t-\tau_s-\tau_\ell) \\
&+ \sum_{s=1}^{q} \sum_{s\neq\ell=1}^{q} \Gamma_{s\ell}^{21} y(t-2\tau_s-\tau_\ell) \\
&+ L(y(t)-\hat{y}(t)),\ t \geqslant 3\tau, \quad (65) \\
\hat{y}(t) &= \mathcal{C}\hat{z}(t), \quad (66) \\
\hat{f}(t) &= V(y(t)-\hat{y}(t)), \quad (67)
\end{aligned}$$

where $\hat{z}(t) \in \mathbb{R}^{n_z}$, $\hat{y}(t) \in \mathbb{R}^{p}$, $\hat{f}(t) \in \mathbb{R}^{n_f}$ are the state, output and fault estimation vectors, respectively; L and V are observer gain matrices to be determined. Define

$$e(t) = z(t) - \hat{z}(t),\ r(t) = \hat{f}(t) - f(t).$$

We have the following estimation error system

$$\begin{aligned}
\dot{e}(t) &= (\mathcal{A}-L\mathcal{C})e(t) + \mathcal{B}_d d(t) \\
&+ \sum_{s=1}^{q} \mathcal{B}_{d_s}^1 d(t-\tau_s) + \sum_{s=1}^{q} \mathcal{B}_{d_s}^2 d(t-2\tau_s) \\
&+ \mathcal{B}_f f(t) + \sum_{s=1}^{q} \mathcal{B}_{f_s}^1 f(t-\tau_s) \\
&+ \sum_{s=1}^{q} \mathcal{B}_{f_s}^2 f(t-2\tau_s) \\
&- LD_d d(t) - LD_f f(t), \quad (68) \\
r(t) &= V\mathcal{C}e(t) + VD_d d(t) \\
&+ (VD_f - I)f(t). \quad (69)
\end{aligned}$$

Let us now denote

$$\begin{aligned}
&\tilde{A} = \mathcal{A} - L\mathcal{C},\ \tilde{C} = V\mathcal{C}, \\
&\overline{B}_d = \begin{bmatrix} \mathcal{B}_d & \mathcal{B}_{d_1}^1 & \dots & \mathcal{B}_{d_q}^1 & \mathcal{B}_{d_1}^2 & \dots & \mathcal{B}_{d_q}^2 \end{bmatrix}, \\
&\overline{B}_f = \begin{bmatrix} \mathcal{B}_f & \mathcal{B}_{f_1}^1 & \dots & \mathcal{B}_{f_q}^1 & \mathcal{B}_{f_1}^2 & \dots & \mathcal{B}_{f_q}^2 \end{bmatrix}, \\
&\overline{I}_f = \begin{bmatrix} I & 0 & \dots & 0 \end{bmatrix}, \\
&\overline{D}_d = \begin{bmatrix} D_d & 0 & \dots & 0 \end{bmatrix}, \\
&\overline{D}_f = \begin{bmatrix} D_f & 0 & \dots & 0 \end{bmatrix}, \\
&\tilde{B}_d = \overline{B}_d - L\overline{D}_d, \tilde{B}_f = \overline{B}_f - L\overline{D}_f, \\
&\tilde{D}_d = V\overline{D}_d, \tilde{D}_f = V\overline{D}_f - \overline{I}_f, \\
&\bar{d}(t) = \begin{bmatrix} d(t) & d(t-\tau_1) & \dots & d(t-\tau_q) \\ & d(t-2\tau_1) & \dots & d(t-2\tau_q) \end{bmatrix}^T \\
&\bar{f}(t) = \begin{bmatrix} f(t) & f(t-\tau_1) & \dots & f(t-\tau_q) \\ & f(t-2\tau_1) & \dots & f(t-2\tau_q) \end{bmatrix}^T
\end{aligned}$$

Then we can rewrite system (68)-(69) as

$$\begin{aligned}
\dot{e}(t) &= \tilde{A}e(t) + \tilde{B}_d\bar{d}(t) + \tilde{B}_f\bar{f}(t), \quad (70) \\
r(t) &= \tilde{C}e(t) + \tilde{D}_d\bar{d}(t) + \tilde{D}_f\bar{f}(t). \quad (71)
\end{aligned}$$

In the following development, we will design an H_∞ fault estimatior, i.e. to find matrices L and V such that the error system (70)-(71) with $\bar{d}(t) = 0$ and $\bar{f}(t) = 0$ is asymptotically stable and, for given $\gamma > 0$, $\lambda > 0$ the following performance is satisfied

$$\begin{aligned}
||G_{r\bar{f}}||_{\infty}^{[-\bar{w},\bar{w}]} &< \gamma, \quad (72) \\
||G_{r\bar{d}}||_{\infty} &< \lambda, \quad (73)
\end{aligned}$$

https://doi.org/10.52111/qnjs.2021.15507

where $G_{r\bar{f}}(s) = \tilde{C}(sI - \tilde{A})^{-1}\tilde{B}_f + \tilde{D}_f$ and $G_{r\bar{d}}(s) = \tilde{C}(sI - \tilde{A})^{-1}\tilde{B}_d + \tilde{D}_d$. Since $||\bar{d}(t)||_{L_2} = \sqrt{2q+1}||d(t)||_{L_2}$ and $||\bar{f}(t)||_{L_2} = \sqrt{2q+1}||f(t)||_{L_2}$. Note that, $||G_{r\bar{f}}||_\infty^{[-\bar{w},\bar{w}]} = \frac{1}{\sqrt{2q+1}}||G_{rf}||_\infty^{[-\bar{w},\bar{w}]}$ and $||G_{r\bar{d}}||_\infty = \frac{1}{\sqrt{2q+1}}||G_{rd}||_\infty$.

The following lemmas are essential for the proof of our results.

Lemma 3.1. *Consider a transfer function matrix $G(s) = C(sI - A)^{-1}B + D$. Letting a symmetric Π be given, the following statements are equivalent:*

(a) The finite frequency inequality

$$\begin{bmatrix} G(iw) \\ I \end{bmatrix}^* \Pi \begin{bmatrix} G(iw) \\ I \end{bmatrix} < 0, \ \forall |w| \leqslant \bar{w}. \quad (74)$$

(b) There exists Hermitian matrices $Q > 0$, P of appropriate dimmension such that

$$\begin{bmatrix} A & B \\ I & 0 \end{bmatrix}^T \begin{bmatrix} -Q & P \\ P & \bar{w}^2 Q \end{bmatrix} \begin{bmatrix} A & B \\ I & 0 \end{bmatrix} + \begin{bmatrix} C & D \\ 0 & I \end{bmatrix}^T \Pi \begin{bmatrix} C & D \\ 0 & I \end{bmatrix} < 0. \quad (75)$$

Lemma 3.2. *Consider a transfer function matrix $G(s) = C(sI - A)^{-1}B + D$. Letting a symmetric Π be given, the following statements are equivalent:*

(a) The infinite frequency inequality

$$\begin{bmatrix} G(iw) \\ I \end{bmatrix}^* \prod \begin{bmatrix} G(iw) \\ I \end{bmatrix} < 0, \ \forall w \in \mathbb{R}. \quad (76)$$

(b) There exists a Hermitian matrix $P > 0$ of appropriate dimmension such that

$$\begin{bmatrix} A & B \\ I & 0 \end{bmatrix}^T \begin{bmatrix} 0 & P \\ P & 0 \end{bmatrix} \begin{bmatrix} A & B \\ I & 0 \end{bmatrix} + \begin{bmatrix} C & D \\ 0 & I \end{bmatrix}^T \Pi \begin{bmatrix} C & D \\ 0 & I \end{bmatrix} < 0. \quad (77)$$

Lemma 3.3. *Given a symmetric matrix Φ and two matrices Γ and Λ, there exists a decision matrix X, that satisfies*

$$\Phi + \Gamma X \Lambda + (\Gamma X \Lambda)^T < 0 \quad (78)$$

if and only if the following conditions are satisfied

$$\Gamma^\perp \Phi {\Gamma^\perp}^T < 0, \quad {\Gamma^T}^\perp \Phi {\Gamma^T}^{\perp T} < 0. \quad (79)$$

Theorem 3.1. *For given matrix $R = \begin{bmatrix} 0 & I & 0 \end{bmatrix}$, scalars $\gamma > 0$, $\lambda > 0$, $\bar{w} > 0$, the error system (70)-(71) is aymptotically stable and performances (72)-(73) hold if there exist Hermitian matrices $Q > 0$, P, real matrices $W > 0$, X and V with appropriate dimmensions such that the following LMIs hold*

$$\begin{bmatrix} Q_1 & Q_2 \end{bmatrix} < 0 \quad (80)$$

$$\begin{bmatrix} Q_3 & Q_4 \end{bmatrix} < 0 \quad (81)$$

where

$$Q_1 = \begin{bmatrix} -Q & P - W \\ * & \Omega \\ * & * \\ * & * \end{bmatrix},$$

$$\Omega = \bar{w}^2 Q + \mathcal{A}^T W + W\mathcal{A} - \mathcal{C}^T X^T - X\mathcal{C}T$$

$$Q_2 = \begin{bmatrix} 0 & 0 \\ W\overline{B}_f - X\overline{D}_f & \mathcal{C}^T V^T \\ -\gamma^2 I & \overline{D}_f^T V^T - \overline{I}_f^T \\ * & -I \end{bmatrix},$$

$$Q_3 = \begin{bmatrix} \mathcal{A}^T W + W\mathcal{A} - \mathcal{C}^T X^T - X\mathcal{C} \\ * \\ * \end{bmatrix},$$

$$Q_4 = \begin{bmatrix} W\overline{B}_d - X\overline{D}_d & \mathcal{C}^T V^T \\ \overline{D}_d^T V^T & -\lambda^2 I \\ * & -I \end{bmatrix}.$$

Proof. We first prove that performance (72) is satisfied if LMI (80) holds. Applying Lemma 3.1 and letting $\Pi = \begin{bmatrix} I & 0 \\ 0 & -\gamma^2 I \end{bmatrix}$, then inequality (72) becomces

$$G_{r\bar{f}}(iw)^* G_{r\bar{f}}(iw) - \gamma^2 I < 0, \ \forall |w| \leqslant \bar{w}.$$

That means performance (72) is satisfied if and only if there exists $n_z \times n_z$ Hermitian matrices $Q > 0$, P such that

$$\begin{bmatrix} \tilde{A} & \tilde{B}_f \\ I & 0 \end{bmatrix}^T \begin{bmatrix} -Q & P \\ P & \bar{w}^2 Q \end{bmatrix} \begin{bmatrix} \tilde{A} & \tilde{B}_f \\ I & 0 \end{bmatrix} + \begin{bmatrix} \tilde{C} & \tilde{D}_f \\ 0 & I \end{bmatrix}^T \Pi \begin{bmatrix} \tilde{C} & \tilde{D}_f \\ 0 & I \end{bmatrix} < 0. \quad (82)$$

By denoting $Y = \begin{bmatrix} \tilde{A}^T & I & 0 \\ \tilde{B}^T & 0 & I \end{bmatrix}$ and

$$\Phi = \begin{bmatrix} -Q & P & 0 \\ P & \bar{w}^2 Q + \tilde{C}^T \tilde{C} & \tilde{C}^T \tilde{D}_f \\ 0 & \tilde{D}_f^T \tilde{C} & \tilde{D}_f^T \tilde{D}_f - \gamma^2 I \end{bmatrix},$$

(82) can be written as

$$Y \Phi Y^T < 0. \quad (83)$$

On the other hand, by denoting $M = \begin{bmatrix} -I & \tilde{A} & \tilde{B}_f \end{bmatrix}^T$ and $N = \begin{bmatrix} I & 0 & 0 \\ 0 & 0 & I \end{bmatrix}^T$, it can be seen that $Y = M^\perp$ and N is the null space of R. Hence, from Lemma 3.3 we see that (83) and inequality

$$N^T \Phi N < 0 \quad (84)$$

hold, if and only if there exists an $n_z \times n_z$ real matrix $W > 0$ such that

$$\Phi + MWR + (MWR)^T < 0. \quad (85)$$

We can express (85) in the following form

$$\begin{bmatrix} P_1 & P_2 \end{bmatrix} < 0 \quad (86)$$

where

$$P_1 = \begin{bmatrix} -Q & P - W \\ * & \bar{w}^2 Q + \tilde{A}^T W + W \tilde{A} + \tilde{C}^T \tilde{C} \\ * & * \end{bmatrix},$$

$$P_2 = \begin{bmatrix} 0 \\ W \tilde{B}_f + \tilde{C}^T \tilde{D}_f \\ \tilde{D}_f^T \tilde{D}_f - \gamma^2 I \end{bmatrix}.$$

By letting $X = WL$ and using Schur[34], it follows that (86) is equivalent to (80).

Next, we will derive sufficient conditions ensuring the asymptotic stability of the error system (70) - (71) and the performance (73). By applying Lemma 3.2 and letting $\Pi = \begin{bmatrix} I & 0 \\ 0 & -\lambda^2 I \end{bmatrix}$, inequality (73) becomces

$$G_{r\bar{d}}(iw)^* G_{r\bar{d}}(iw) - \lambda^2 I < 0, \ \forall w \in \mathbb{R}.$$

That means performance $||G_{r\bar{d}}||_\infty < \lambda$ is satisfied if and only if there exists a $n_z \times n_z$ real symmetric matrix $W > 0$ such that

$$\begin{bmatrix} \tilde{A} & \tilde{B}_d \\ I & 0 \end{bmatrix}^T \begin{bmatrix} 0 & W \\ W & 0 \end{bmatrix} \begin{bmatrix} \tilde{A} & \tilde{B}_d \\ I & 0 \end{bmatrix} + \begin{bmatrix} \tilde{C} & \tilde{D}_d \\ 0 & I \end{bmatrix}^T \Pi \begin{bmatrix} \tilde{C} & \tilde{D}_d \\ 0 & I \end{bmatrix} < 0, \quad (87)$$

which is equivalent to

$$\begin{bmatrix} \tilde{A}^T W + W \tilde{A} & W \tilde{B}_d & \tilde{C}^T \\ * & -\lambda^2 I & \tilde{D}_d^T \\ * & * & -I \end{bmatrix} < 0. \quad (88)$$

Let $X = WL$, it follows that (88) is equivalent to (81). If (81) holds, then $\tilde{A}^T W + W \tilde{A} < 0$, which implies that system (70)-(71) asymptotically stable. Note that, we can solve the following optimization problem in order to get optimal fault estimation:

$$\min \gamma, \quad s.t. (80), (81). \quad (89)$$

Remark 1. *The results of this paper can be extended to the case where the time delays τ_s $(s = 1, 2, \ldots, q)$ are time varying, that is, $\tau_s(t)$, $\tau_s^- \le \tau_s(t) \le \tau_s^+$ for all $t \ge 0$, where $\tau_s^- > 0$, $\tau_s^+ > 0$. Indeed, we can approximate terms $x_s(t - \tau_s(t))$ by $x_s(t - \tau_s^*)$, where $\tau_s^* = \frac{\tau_s^- + \tau_s^+}{2}$. By this way, systems with time-varying delays can be reduced to systems with time-invariant delays of the form (4)-(6), where $\tau_s(t)$ are replaced by τ_s^* for all $s = 1, 2, \ldots, q$.*

Remark 2. *Let us consider the case where the output vector of system (4)-(6) is delayed, that is, $y(t) = Cx(t) + C_d x(t - \tau) + D_d d(t) + D_f f(t)$. For this case, we introduce an integral output vector $z(t) = \int_0^t y(\theta) d\theta$ such that $\dot{z}(t) = y(t) =$*

https://doi.org/10.52111/qnjs.2021.15507

$Cx(t) + C_d x(t-\tau) + D_d d(t) + D_f f(t)$. By denoting $\zeta(t) = \begin{bmatrix} z(t) \\ x(t) \end{bmatrix}$, we obtain an augmented system of the form (4)-(6), where state variable is $\zeta(t)$ and the output is not delayed. By this way, we can extend the results of this paper to systems with delayed outputs.

4. A NUMERICAL EXAMPLE

Let us consider the motivated fourth-order example in Section 1. According to Step 1 of the Algorithm 1, we obtain matrices X_5 and Y_5 from equations (38)-(54). Since $\text{rank}\begin{bmatrix} X_5 \\ Y_5 \end{bmatrix} = 34 = \text{rank}\begin{bmatrix} X_5 \end{bmatrix}$, condition (55) is satisfied and we get

$$\begin{aligned}
\chi_5 &= \begin{bmatrix} \chi_5^1 & \chi_5^2 & \chi_5^3 & \chi_5^4 \end{bmatrix} \\
&= \begin{bmatrix} \chi_5^{11} & \chi_5^{12} & \chi_5^{25} & \chi_5^{26} & \chi_5^3 & \chi_5^4 \end{bmatrix}, \\
\chi_5^{11} &= \begin{bmatrix} \alpha_3^1 & \alpha_3^2 & \gamma_3^3 & \gamma_4^3 \end{bmatrix} \\
&= \begin{bmatrix} -1 & -0.8333 & -1 & -0.8333 \end{bmatrix}, \\
\chi_5^{12} &= \begin{bmatrix} \beta_{32}^1 & \beta_{32}^2 & \beta_{33}^1 & \beta_{33}^2 \end{bmatrix} \\
&= \begin{bmatrix} -3 & -1.3333 & -3 & -3.3333 \end{bmatrix}, \\
\chi_5^{25} &= \begin{bmatrix} \beta_{41}^1 & \beta_{41}^2 & \beta_{42}^1 & \beta_{42}^2 \end{bmatrix} \\
&= \begin{bmatrix} -8 & -3 & 4 & 3 \end{bmatrix}, \\
\chi_5^{26} &= \begin{bmatrix} \beta_{51}^1 & \beta_{51}^2 & \beta_{52}^1 & \beta_{52}^2 \end{bmatrix} \\
&= \begin{bmatrix} -1.636 & 5.2082 & 0.5657 & -0.8032 \end{bmatrix}, \\
\chi_5^3 &= \begin{bmatrix} \alpha_4^1 & \alpha_4^2 \end{bmatrix} = \begin{bmatrix} -1.0561 & -2.6835 \end{bmatrix}, \\
\chi_5^4 &= \begin{bmatrix} \nu_{51}^1 & \nu_{51}^2 & \nu_{52}^1 & \nu_{52}^2 \end{bmatrix} = 0_{1,4}.
\end{aligned}$$

Next, in Step 2, by substituting β_{41}^1, β_{41}^2, β_{42}^1, β_{42}^2, β_{51}^1, β_{51}^2, β_{52}^1, β_{52}^2, α_4^1 and α_4^2 into (58)-(59) and obtain matrices Z_5 and T_5. Since $\text{rank}\begin{bmatrix} Z_5 \\ T_5 \end{bmatrix} = 2 = \text{rank}\begin{bmatrix} Z_5 \end{bmatrix}$, condition (64) is satisfied. Hence, we obtain $\zeta_5 = \begin{bmatrix} \alpha_5^1 & \alpha_5^2 & \gamma_5^3 & \gamma_5^4 & \gamma_5^5 \end{bmatrix} = \begin{bmatrix} -1.2007 & -0.6244 & -1.2007 & -0.6244 & 0.0823 \end{bmatrix}$. Then according to Step 3, we obtain

$$\begin{aligned}
z_1(t) &= x_1(t), \\
z_2(t) &= x_2(t), \\
z_3(t) &= -0.1667x_2(t) + 2x_1(t-\tau_1) \\
&+ 0.3333x_2(t-\tau_1) - x_3(t-\tau_1) \\
&- 2x_4(t-\tau_1) - x_1(t-\tau_2) - 0.6667x_2(t-\tau_2), \\
z_4(t) &= 2.0561x_1(t) + 3.6835x_2(t) + 6x_1(t-\tau_1) \\
&+ x_2(t-\tau_1) - 3x_3(t-\tau_1) - 3x_4(t-\tau_1) \\
&- x_1(t-\tau_2) - 0.6667x_2(t-\tau_2), \\
z_5(t) &= 2.8281x_1(t) + 2.2518x_2(t) \\
&+ 8.213x_1(t-\tau_1) + 1.3688x_2(t-\tau_1) \\
&- 4.1065x_3(t-\tau_1) - 3.1626x_4(t-\tau_1) \\
&- 4.1065x_1(t-\tau_2) - 2.7377x_2(t-\tau_2).
\end{aligned}$$

And then, a transformed system of the form (21)-(22) is obtained, where $\mathcal{C} = \begin{bmatrix} 1 & 0 & 0 & 0 & 0 \\ 0 & 1 & 0 & 0 & 0 \end{bmatrix}$, $\mathcal{B}_1^2 = \mathcal{B}_2^2 = \mathcal{B}_{d_1}^2 = \mathcal{B}_{d_2}^2 = \mathcal{B}_{f_1}^2 = \mathcal{B}_{f_2}^2 = 0_{5,1}$, $\Gamma_1^3 = \Gamma_2^3 = \Gamma_{12}^{21} = \Gamma_{21}^{21} = 0_{5,2}$ and

$$\begin{aligned}
\mathcal{A} &= \begin{bmatrix} 0 & 0 & 1 & 0 & 0 \\ 0 & 0 & 0 & 1 & 0 \\ 0 & 0 & -1 & -0.8333 & 0 \\ 0 & 0 & 0 & 0 & 1 \\ 0 & 0 & -1.2007 & -0.6244 & 0.0823 \end{bmatrix}, \\
\mathcal{B} &= \begin{bmatrix} 1 \\ 2 \\ -0.3333 \\ 9.4230 \\ 7.3317 \end{bmatrix}, \ \mathcal{B}_1^1 = \begin{bmatrix} 0 \\ 0 \\ -8.3333 \\ -13 \\ -14.019 \end{bmatrix}, \\
\mathcal{B}_2^1 &= \begin{bmatrix} 0 \\ 0 \\ -2.3333 \\ -7 \\ -9.5818 \end{bmatrix}, \mathcal{B}_d = \begin{bmatrix} 0.1 \\ 0.2 \\ -0.0333 \\ 0.9423 \\ 0.7332 \end{bmatrix}, \\
\mathcal{B}_{d_1}^1 &= \begin{bmatrix} 0 \\ 0 \\ -0.8333 \\ -1.3 \\ -1.4019 \end{bmatrix}, \ \mathcal{B}_{d_2}^1 = \begin{bmatrix} 0 \\ 0 \\ -0.2333 \\ -0.7 \\ -0.9582 \end{bmatrix},
\end{aligned}$$

https://doi.org/10.52111/qnjs.2021.15507

$$\mathcal{B}_f = \begin{bmatrix} 1.1 \\ 1.2 \\ -0.2 \\ 6.6818 \\ 5.8131 \end{bmatrix}, \ \mathcal{B}_{f_1}^1 = \begin{bmatrix} 0 \\ 0 \\ -1.5 \\ -0.3 \\ 0.9109 \end{bmatrix},$$

$$\mathcal{B}_{f_2}^1 = \begin{bmatrix} 0 \\ 0 \\ -1.9 \\ -5.7 \\ -7.8023 \end{bmatrix},$$

$$\Gamma = \begin{bmatrix} -1 & -0.8333 \\ -1.0561 & -2.6835 \\ 1.5467 & 2.7362 \\ -1.2007 & -0.6244 \\ 0.4748 & 1.3382 \end{bmatrix},$$

$$\Gamma_1^1 = \begin{bmatrix} -3 & -1.3333 \\ -8 & -3 \\ 17.6667 & 11.8333 \\ -1.636 & 5.2082 \\ 15.322 & 10.7619 \end{bmatrix},$$

$$\Gamma_2^1 = \begin{bmatrix} -3 & -3.3333 \\ 4 & 3 \\ -3.3333 & -2.1667 \\ 0.5657 & -0.8032 \\ -10.4279 & -9.5159 \end{bmatrix},$$

$$\Gamma_1^2 = \begin{bmatrix} 0 & 0 \\ 0 & 0 \\ 1.3333 & -2.6667 \\ 4 & -8 \\ 5.4753 & -10.9506 \end{bmatrix},$$

$$\Gamma_2^2 = \begin{bmatrix} 0 & 0 \\ 0 & 0 \\ 3.3333 & 3.3333 \\ 10 & 10 \\ 13.6883 & 13.6883 \end{bmatrix},$$

$$\Gamma_{12}^{11} = \begin{bmatrix} 0 & 0 \\ 0 & 0 \\ -5.6667 & -5.6667 \\ -17 & -17 \\ -23.2701 & -23.2701 \end{bmatrix},$$

$$\Gamma_{21}^{11} = \begin{bmatrix} 0 & 0 \\ 0 & 0 \\ 2.3333 & 2.3333 \\ 7 & 7 \\ 9.5818 & 9.5818 \end{bmatrix}.$$

On the other hand, we have the following matrices

$$\overline{I}_f = \begin{bmatrix} 1 & 0 & 0 & 0 & 0 \end{bmatrix},$$

$$\overline{B}_d = \begin{bmatrix} 0.1 & 0 & 0 & 0 & 0 \\ 0.2 & 0 & 0 & 0 & 0 \\ -0.0333 & -0.8333 & -0.2333 & 0 & 0 \\ 0.9423 & -1.3 & -0.7 & 0 & 0 \\ 0.7332 & -1.4019 & -0.9582 & 0 & 0 \end{bmatrix},$$

$$\overline{B}_f = \begin{bmatrix} 1.1 & 0 & 0 & 0 & 0 \\ 1.2 & 0 & 0 & 0 & 0 \\ -0.2 & -1.5 & -1.9 & 0 & 0 \\ 6.6818 & -0.3 & -5.7 & 0 & 0 \\ 5.8131 & 0.9109 & -7.8023 & 0 & 0 \end{bmatrix},$$

$$\overline{D}_d = \begin{bmatrix} 0.1 & 0 & 0 & 0 & 0 \\ 0.2 & 0 & 0 & 0 & 0 \end{bmatrix},$$

$$\overline{D}_f = \begin{bmatrix} 0.3 & 0 & 0 & 0 & 0 \\ 0.4 & 0 & 0 & 0 & 0 \end{bmatrix}.$$

Set $\lambda = 0.5$. Solving the optimization problem (89), we obtain $\gamma_{\min} = 0.7$ and

$$L = \begin{bmatrix} 15.1993 & -4.1548 \\ -5.8977 & 21.5871 \\ 53.7296 & -37.7022 \\ -47.5788 & 118.5215 \\ -35.4247 & 102.6286 \end{bmatrix},$$

$$V = \begin{bmatrix} 9.5164 & -4.7344 \end{bmatrix}.$$

5. CONCLUSION

A novel method has been proposed for computing state transformations of time-delay systems in this paper. The H_∞ fault estimation problem for time-delay systems has been re-formulated as the corresponding problem for linear time invariant systems. A numerical example has been given to demonstrate the obtained results. In the

https://doi.org/10.52111/qnjs.2021.15507

future, we will extend the results of this paper to address the problem of H_∞ fault estimation for interconnected systems with time-varying delays and unknown inputs.

REFERENCES

1. P.M. Frank, X. Ding. Survey of robust residual generation and evaluation methods in observer-based fault detection systems, *Journal of Process Control*, **1997**, *7*, 403-424.

2. J.J. Gertler. Survey of model-based failure detection and isolation in complex plant, *IEEE Control Systems Magazine*, **1998**, *3*, 3-11.

3. J. Chen, R.J. Patton. *Robust Model-Based Fault Diagnosis for Dynamic Systems*, Kluwer Academic Publishers, Massachusetts, 1999.

4. M. Fang, Y. Tian, L. Guo. Fault diagnosis of nonlinear system based on generalized observer, *Applied Mathematics and Computation*, **2007**, *185*, 1131-1137.

5. P.J. Zufiria. A mathematical framework for new fault detection schemes in nonlinear stochastic continuous-time dynamical systems, *Applied Mathematics and Computation*, **2012**, *218*, 11391-11403.

6. J.P. Richard. Time-delay systems: An overview of some recent advances and open problems, *Automatica*, **2003**, *39*, 1667-1694.

7. S.X. Ding. *Model-based fault diagnosis techniques, design schemes, algorithms, and tools*, Springer, Berlin Heidelberg, 2008.

8. B. Jiang, M. Staroswiecki, V. Cocquempot. *Fault identification for a class of time-delay systems*, Proceeding of American Control Conference, Anchorage, Anchorage, AK, 8-10 May, 2002, 2239-2244.

9. C.H. Jiang, D.H. Zhou. Fault detection and identification for uncertain linear time-delay systems, *Computers Chemical Engineering*, **2005**, *30*, 228-242.

10. Z.H. Mao, B. Jiang. Fault estimation and accommodation for networked control systems with transfer delay, *Acta Automatica Sinica*, **2007**, *33*, 738-743.

11. M. Zhong, H. Ye, S.X. Ding. An iterative LMI approach to RFDF for linear systems with time-varying delays, *Asian Journal of Control*, **2006**, *8*, 86-90.

12. W. Chen, M. Saif. An iterative learning observer for fault detection and accommodation in nonlinear time-delay systems, *International Journal of Robust Nonlinear Control*, **2006**, *16*, 1-19.

13. L.S. Bai, Z.H. Tian, S.J. Shi. Robust fault detection for a class of nonlinear time-delay systems, *Journal of The Franklin Institute*, **2007**, *334*, 837-888.

14. Z.W. Gao, T. Breikin, H. Wang. Reliable observer-based control against sensor failures for systems with time delays in both state and input, *IEEE Transactions on Systems, Man, and Cybernetics-Part A*, **2008**, *38*, 1018-1029.

15. N. Meskin, K. Khorasani. Robust fault detection and isolation of time-delay systems using a geometric approach, *Automatica*, **2009**, *45*, 1567-1537.

16. M.Y. Zhong, Q.L. Han. Fault-tolerant master-slave synchronization for Lur'e systems using time-delay feedback control, *IEEE Transactions on Circuits and Systems I: Regular Papers*, **2009**, *56*, 1391-1404.

17. D.C. Huong, H. Trinh, H.M. Tran, T. Fernando. Approach to fault detection of time-delay systems using functional observers, *Electronics Letters*, **2014**, *50*, 1132-1134.

18. G.H. Yang, J.L. Wang, Y.C. Soh. Reliable H_∞ controller design for linear systems, *Automatica*, **2001**, *37*, 717-725.

19. B. Jiang, F.N. Chowdhury. Fault estimation and accommodation for linear MIMO discrete-time systems, *IEEE Transactions on Control Systems Technology*, **2005**, *13*, 493-499.

20. M. Misra, H.H. Yue, S.J. Qin. Multivariate process monitoring and fault diagnosis by multi-scale PCA, *Computers and Chemical Engineering*, **2002**, *26*, 1281-1293.

21. H. Wang, L. Shen. Fault detection and estimation for nonlinear systems with linear output structure, *International Journal of Adaptive Control and Signal Processing*, **2004**, *19*, 267-279.

22. T. Iwasaki, S. Hara. Generalized KYP Lemma: unified frequency domain inequalities with design applications, *IEEE Transactions on Automatic Control*, **2005**, *50*, 41-59.

23. H. Wang, G.H. Yang. A finite frequency domain approach to fault detection for linear discrete-time systems, *International Journal of Control*, **2008**, *81*, 1162-1171.

24. X.J. Li, G.H. Yang. Fault detection observer design in low frequency domain for linear time-delay systems, *Acta Automatica Sinica*, **2009**, *35*, 1465-1469.

25. H. Gao, X. Li. H_∞ filtering for discrete-time state-delayed systems with finite frequency specifications, *IEEE Transactions on Automatic Control*, **2011**, *56*, 2935-2941.

26. J. Shen, J. Lam. Improved results on H_∞ model reduction for continuous-time linear systems over finite frequency ranges, *Automatica*, **2015**, *53*, 79-84.

27. Y. He, Q.G. Wang, C. Lin. An improved H_∞ filter design for systems with time-varying interval delay, *IEEE Transaction on circuits and systems-II: Express brieffs*, **2006**, *53*, 1235-1239.

28. X. Li, Z. Li, H. Gao. Further results on H_∞ filtering for discrete-time systems with state delay, *International Journal Robust and Nonlinear Control*, **2011**, *21*, 248-270.

29. X. Li, H. Gao. A new model transformation of discrete-time systems with time-varying delay and its application to stability analysis, *IEEE Transaction on Automatic Control*, **2011**, *56*, 2172-2178.

30. M. Hou, P. Zitek, R.I. Patton. An observer design for linear time-delay systems, *IEEE Transactions on Automatic Control*, **2002**, *47*, 121-125.

31. Q.C. Dong, M. Zhong, S.X. Ding. H_∞ fault estimation for a class of linear time-delay systems in finite frequency domain, *Journal of Systems Engineering and Electronics*, **2010**, *21*, 835-841.

32. D.C. Huong, H. Trinh. Method for computing state transformations of time-delay systems, *IET Control Theory & Applications*, **2015**, *9*, 2405-2413.

33. D.T.H. Yen, D.C. Huong. A new method for designing observers of a nonlinear time-delay Glucose-Insulin system, *Quynhon Journal of Science*, **2020**, *14*(1), 37-46.

34. S. Boyd, L.E. Ghaoui, V. Balakrishnan. *Linear Matrix Inequalities in Systems and Control Theory*, SIAM Studies in Applied Mathematics, Philadelphia, 1994.

https://doi.org/10.52111/qnjs.2021.15507

TẠP CHÍ KHOA HỌC
TRƯỜNG ĐẠI HỌC QUY NHƠN

Khảo sát các chế độ làm việc của hệ thống chỉnh lưu PWM - động cơ điện một chiều kích từ độc lập

Bùi Văn Vũ*, Võ Phương, Đỗ Văn Cần, Lê Thái Hiệp

Khoa Kỹ thuật và Công nghệ, Trường Đại học Quy Nhơn, Việt Nam

Ngày nhận bài: 26/04/2021; Ngày nhận đăng: 04/08/2021

TÓM TẮT

Trước đây, động cơ điện một chiều được cấp nguồn từ lưới thông qua thiết bị chỉnh lưu dùng thyristor. Tuy nhiên, các bộ biến đổi dùng thyristor truyền thống này có những nhược điểm như: Dòng điện đầu vào chứa nhiều sóng hài điều hòa bậc cao; Sự nhấp nhô đỉnh – đỉnh của điện áp đầu ra cao; Chỉ cho dòng điện đi theo một chiều dẫn đến không thể trả năng lượng dư thừa của ĐC về phía xoay chiều; Bộ chỉnh lưu PWM có thể khắc phục được những nhược điểm của các bộ chỉnh lưu, bộ biến đổi truyền thống dùng thyristor. Trong bài báo này, tác giả khảo sát các chế độ làm việc của hệ thống chỉnh lưu PWM – Động cơ điện một chiều kích từ độc lập (CLPWM – Đ) để thấy được những ưu điểm của hệ thống này so với hệ thống chỉnh lưu thyristor – Động cơ điện một chiều truyền thống (T - Đ).

Từ khóa: *Động cơ điện một chiều, chỉnh lưu thyristor, chỉnh lưu PWM, sóng hài bậc cao, điện áp đầu ra.*

**Tác giả liên hệ chính.*
Email: bvvu@ftt.edu.vn

JOURNAL OF SCIENCE
QUY NHON UNIVERSITY

A survey of working models of direct current motor in PWM rectifier - separately excited direct current motor system

Bui Van Vu*, Vo Phuong, Do Van Can, Le Thai Hiep

Faculty of Engineering and Technology, Quy Nhon University, Vietnam

Received: 26/04/2021; Accepted: 04/08/2021

ABSTRACT

Previously, direct current motors (DCMs) were powered from the alternating grid via thyristor rectifiers. However, these traditional thyristor converters have major disadvantagessuch as (1) input alternating currents contain a lot of high order harmonics, (2) peak-to-peak ripple in output direct voltage is high, and (3) output current can only flow in one direction. PWM rectifiers can overcome the disadvantages of conventional thyristor rectifiers or thyristor converters. This paper considers the working modes of DCM in PWM rectifier-DCM system in order that we can see the advantages of this rectifier system when it was compared to the traditional thyristor rectifier-DCM system.

Keywords: *Direct current motor, thyristor rectifier, PWM rectifier, high order harmonic, output voltage.*

1. INTRODUCTION

Direct current motors (DCMs) have the great advantage of being able to adjust the speed in a wider range and smoother than the AC motor. Therefore, these motors are still widely used in electrical equipment that needs to be adjusted speed with high precision and smoothness, such as motors for textile machines, printers, robots, electric cars, etc.

Previously, DCMs were powered by rectifiers using thyristors (T-D).[1,2] However, the traditional drive systems (T-D) have many disadvantages such as low voltage quality at the output of the rectifier, the generation of many high-order harmonics on the grid and difficulties in flowing energy from the DCM side to the grid when the regenerative braking occurs.

The PWM rectification method using IGBT[3-8] is expected to be able to replace traditional rectifiers using thyristors in controlling DCMs. In this paper, the authors examine different working modes of the PWM rectifier-DCM system (CLPWM-DCM) to see the advantages of this system compared to the traditional thyristor rectifier-DCM system (T-D).

The CLPWM-DCM system proposed in this paper can overcome the disadvantages of the drive systems T-D. For instance, the system does not cause many high-order harmonics on the grid; the peak-to-peak ripple of the system's output voltage is low; The PWM rectifier allows power to flow in two directions without any other supporting converters.

2. SURVEY OF WORKING MODES OF DCM

2.1. CLPWM – D drive system

Currently, there are different pulse width modulation (PWM) techniques.[9,10] Most of them require complex transformations and a large

**Corresponding author.*
Email: bvvu@ftt.edu.vn

https://doi.org/10.52111/qnjs.2021.15508

number of current and voltage sensors are used. In this paper, the author uses a PWM rectifier using the Sin-Triangle pulse width modulation method[11-13] to build and analyze the working modes of the DCM in the CLPWM-DCM drive system.

Compared with the PWM control techniques in references 8, 9, 10, the PWM rectifier control technique that the author uses does not use any sensors or any voltage estimator. Besides, this method does not require complicated transformations like space vector modulation[9] or PLL[10] controller, so the controller is not too complicated. This is suitable for designing an empirical system. The circuit diagram of the CLPWM-DCM system is shown in Figure 1.

In the article, the author does not go into a detailed analysis of the controller of the PWM rectifier but goes into the simulation and detailed analysis of the working modes of DCM in the CLPWM-DCM system. The control diagram of the PWM rectifier in the CLPWM-DCM system is also shown in Figure 2.

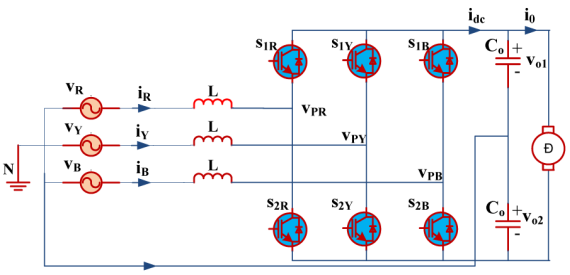

Figure 1. Circuit diagram of CLPWM-DCM system

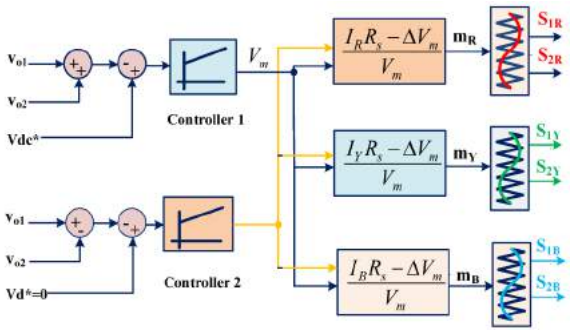

Figure 2. Control circuit diagram of PWM rectifier.[11,12]

2.2. Working modes of DCM

To see the advantages of the CLPWM-DCM system compared to the T-D system, the author analyzes the different working modes of the DCM in both systems. The examined DCM parameters are shown in Table 2. The rectifier used in the T-D system is a controlled 3-phase bridge thyristor rectifier. The circuit diagram of the T-D system is shown in Figure 3.

The simulation diagram of the working modes of the CLPWM-DCM system is shown in Figure 4. The parameters of the CLPWM-DCM system are shown in Table 1, and Table 2.

In the different working modes of DCM in the CLPWM-DCM system, the author uses the DCM starting method by changing the armature voltage,[14] so the starting current of the DC in all modes working (Figure 5, Figure 7, Figure 8, Figure 9, Figure 10, Figure 12 and Figure 15) is less variable, within the allowable limit to increase the service life and ensure the safety of the engine during the work process.

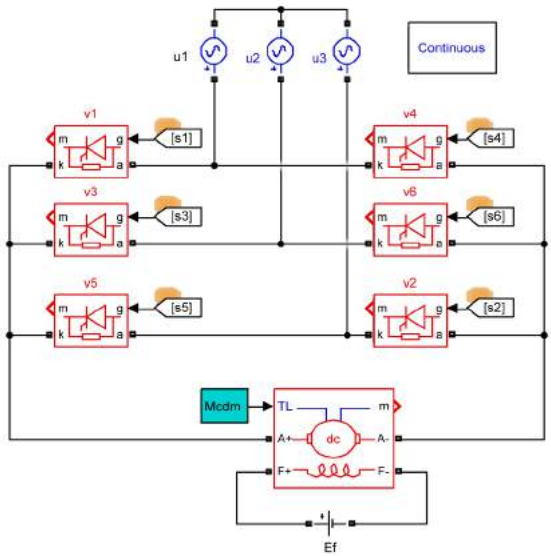

Figure 3. Circuit diagram of T-D drive system.

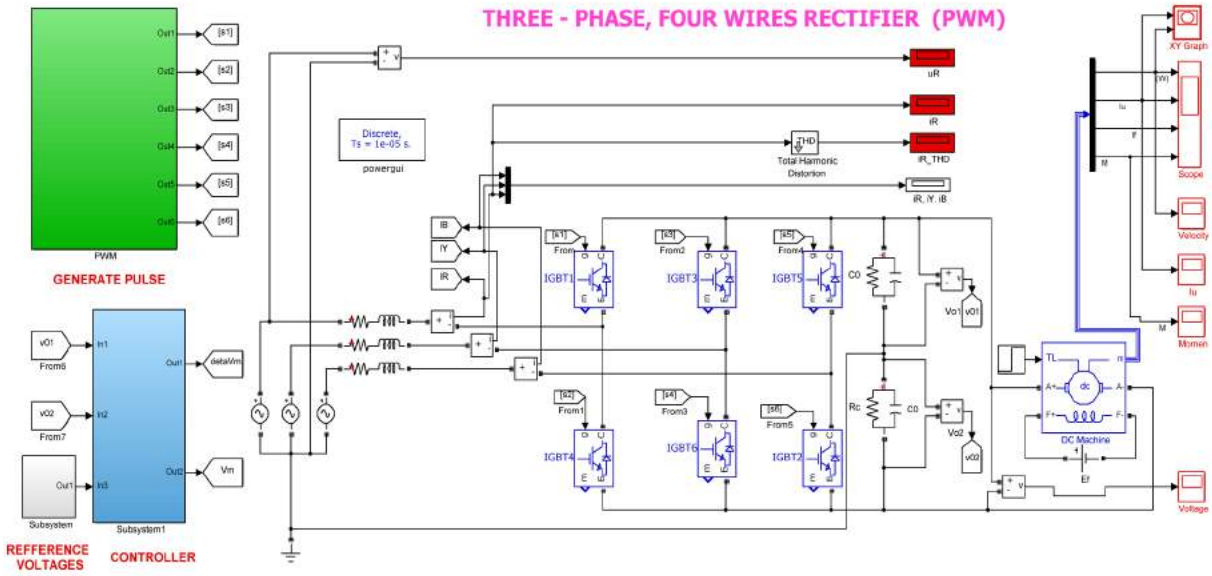

Figure 4. Simulation diagram of working modes of DCM in CLPWM–DCM system

Table 1. Parameters of PWM rectifier

No.	Symbol	Interpretation of the symbol	Parameter
1	f (Hz)	Frequency of the grid.	50
2	V_{Grid} (V)	The average phase voltage of the grid.	220
3	V_{o1}, V_{o2} (V)	The voltage value of two direct current (DC) buses.	120
4	L_c (mH)	Inductance L.	8.61
5	C_o (μF)	Capacitance C.	2200
6	R_S (Ω)	Current sensor gain.	1/10
7	F_c (kHz)	Carrier frequency.	11
8	R_c (Ω)	The resistance of the capacitor C_o.	11000

Table 2. Parameters of DCM

No.	Symbol	Interpretation of the symbol	Parameter
1	P (Hp)	Output Power	5
2	U_{udm} (V)	Input Voltage	240
3	ω_{dm} (Rad/s)	Angular speed	183
4	L_u (H)	Armature inductance	0.12
5	R_u (Ω)	Armature resistance	1.5
6	L_{kt} (H)	Field inductance	156
7	R_{kt} (Ω)	Field resistance	281.3
8	L_m (H)	Field-armature mutual inductance	1.10
9	U_{kt} (V)	Field Voltage	300

2.1.1. Motoring mode

When the motoring mode happens, the DCM speed is greater than 0 (Figure 5), the DCM Armature current is in the same direction as the electromotive force (E_d) of the rectifier, so the current is positive (Figure 5). Therefore, the torque-speed characteristic of DCM is in the first quadrant (Figure 6).

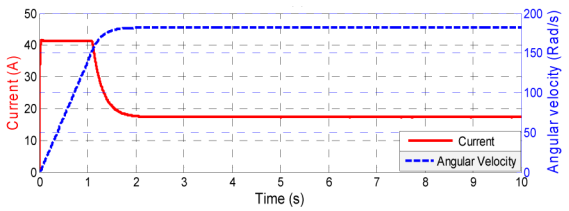

Figure 5. Current and speed of the motor in CLPWM-DCM system when the motoring mode happens

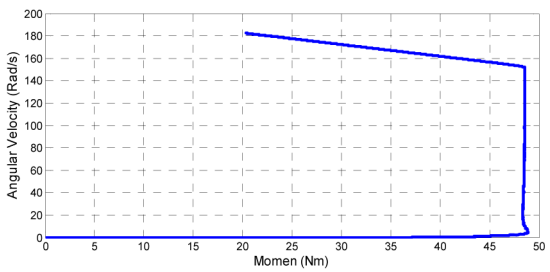

Figure 6. Characteristic of DCM in CLPWM-DCM system when the motoring mode happens

2.1.2. Regenerative Braking

At time t = 5(s), the voltage supplied to the DCM is rapidly reduced from the rated voltage

https://doi.org/10.52111/qnjs.2021.15508

Udm = 240V to 100V. If the DCM load is an inertial one, its speed at this time decreases slowly, not corresponding to the rate of voltage drop, so the DCM current now has a negative value.

Figure 7 shows that in a T-D drive system, the 3-phase bridge rectifier using thyristor only allows current to flow in one direction, so it cannot return excess energy from the DC (Direct current) side to the AC (Alternative current) side. This is the disadvantage of this drive system.

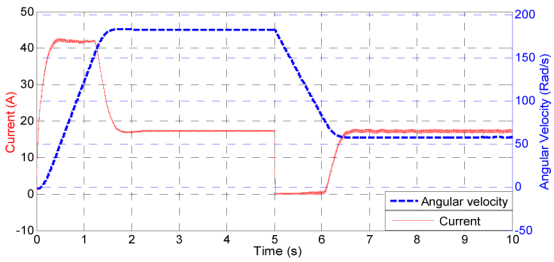

Figure 7. The DCM armature current and speed in T-D when the regenerative braking happens

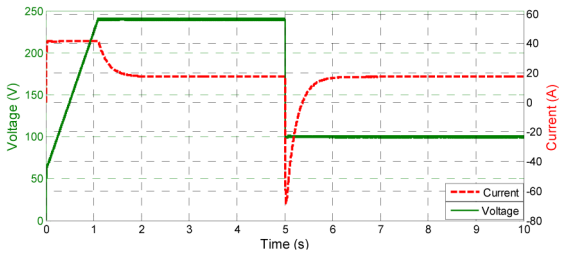

Figure 8. DCM armature current and speed in CLPWM-DCM system when the regenerative braking happens

Regarding the CLPWM-DCM system, the PWM rectifier allows current to flow in the opposite direction from the DC side to the AC side if there is excess energy on the DC side. So now, the excess energy on the DC side flows to the AC side as shown in Figure 8. This is the advantage of the CLPWM-DCM system over the T-D drive system.

The problem here is that the value of the regenerative braking current flowing from the DC side to the AC side is much larger than 2.5 times the DCM rated current (Figure 8). To overcome this problem, the author also calculates and gives a formula to determine the voltage drop rate so that the value of current when the regenerative braking happens is less than or equal to 2.5 times the DCM rated current as is shown in Formula (1).

$$\mathrm{D}u = \frac{(K\mathrm{F})^2 K_h I_{udm} + K\mathrm{F} M_c}{J} t + (K_h I_{udm} + I_{udm}) R_u \quad (1)$$

After determining the voltage drop rate so that the regenerative braking current does not exceed the allowable value as Formula (1), the regenerative braking process is simulated. The simulation results are shown in Figure 9. Specifically, when the DCM is working at rated load, at time t = 5s, we reduce the voltage supplied to the DCM from the rated voltage value to 100V with a voltage decreasing rate is calculated by Figure (1). If the load of the DCM is an inertial one, its speed at this time decreases slowly without corresponding to the voltage drop rate, so the DC current is negative. At this time, the PWM rectifier allows current to flow in the opposite direction, the excess energy on the DC side flows back to the AC side as shown in Figure 9. At this point, the regenerative braking happens, the operation of the DCM is in quadrant II (Figure 10). This is an advantage that the thyristor rectifier in the T-D systems does not have (Figure 7).

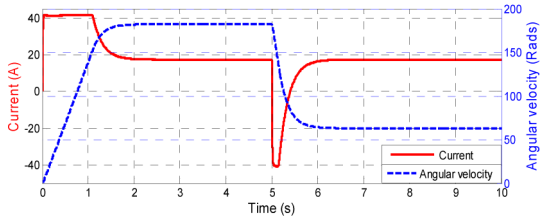

Figure 9. DCM current and speed in CLPWM-DCM system when the regenerative braking happens in case of the braking current is limited.

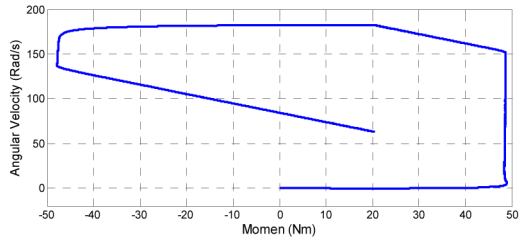

Figure 10. Characteristic of DCM in CLPWM-DCM system when the regenerative braking happens.

As the speed of the DCM gradually decreases, its armature current gradually increases. Until this current increases to greater

than 0, the regenerative braking (in quadrant II) turns into the motoring mode (in quadrant I) (Figure 10).

Thanks to the voltage drop at the rate determined by Formula (1), the DCM current when the regenerative braking happens does not exceed the allowable current value as is the case shown in Figure 8. At this point, the current is less variable and is not exceed the allowable value ($2.5*I_{dm}$) as shown in Figure 9.

2.1.3. Reverse current braking

In order for reverse current braking to take place, at time t = 5(s), the voltage supplied to the DCM is rapidly reduced from the rated voltage Udm = 240 V to 15 V. If the DCM load is an inertial one, its speed at this time decreases slowly, not corresponding to the rate of voltage drop, so the DCM current would now have a negative value.

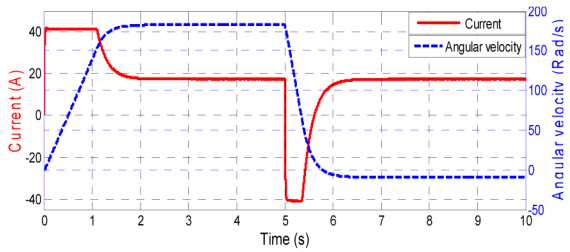

Figure 11. DCM current and speed in the CLPWM-DCM system when the reverse current braking happens.

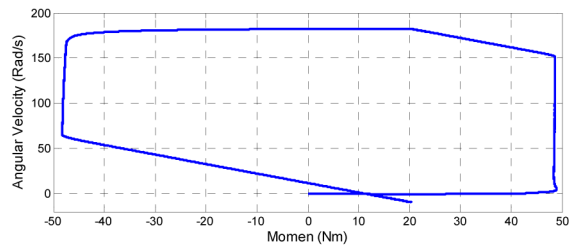

Figure 12. Characteristic of DCM in CLPWM-DCM system when the reverse current braking happens.

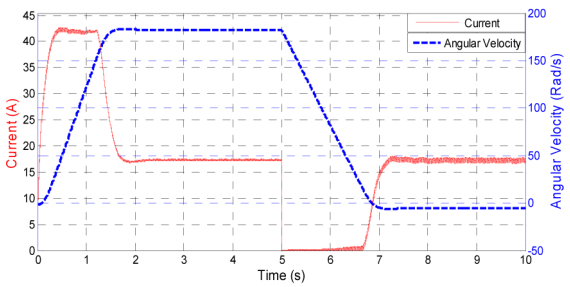

Figure 13. The DCM current and speed in T-D system when the reverse current braking happens.

At this time, the PWM rectifier allows current to flow in the opposite direction, the excess energy on the DC side would flows to the AC side as shown in Figure 11. At this point, the regenerative braking takes place, the operation of the DCM is in quadrant II (Figure 12). This is an advantage that thyristor-using rectifiers cannot do (Figure 13). The simulation results in Figure 11 also show that thanks to the voltage reduction at the rate calculated by Formula (1), the return current to the grid of the motor is not too large, not exceed the allowable value ($2.5*I_{dm}$).

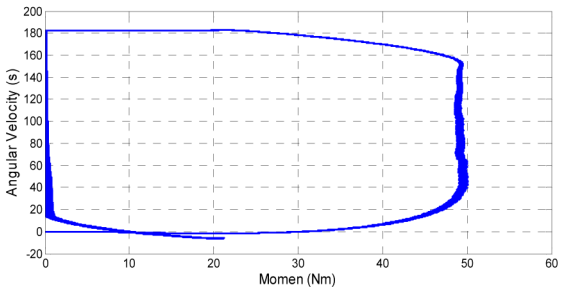

Figure 14. Characteristic of DCM in T-D system when the reverse current braking happens.

If the load is a potential load, under the influence of the load's gravity, the DC speed decreases gradually, so the DCM current gradually increases. Until the current has just increased to greater than 0, the torque is still smaller than the potential torque of the load, so the DCM speed continues to decrease. At this time, the torque-speed characteristic of the motor is in quadrant I (Figure 12).

When the speed drops to 0, because the DCM torque is still smaller than the load potential torque, the DCM speed starts to reverse and increase in the negative direction. The reverse current braking starts happening. The torque-speed characteristic of the motor is shown in Figure 12.

To see the advantages of the CLPWM-DCM system, we compare this system with the traditional T–D system. For the CLPWM-DCM system, the PWM rectifier can allow the current to flow in the opposite direction (Figure 11). So, at the time of voltage is dropped rapidly so

https://doi.org/10.52111/qnjs.2021.15508

that the reverse current braking happens, at first the regenerative braking takes place, returning energy to the grid (Figure 11).

The torque-speed characteristic of the DCM is shown in Figure 12. For the T-D system, the rectifier using thyristors cannot allow the current to flow in the opposite direction, so when reducing the voltage in order for the reverse current braking to happen, the DCM cannot return the excess energy to the grid (Figure 13). This leads to a waste of excess energy when dropping voltage in order the reverse current braking to arise. The characteristic of the motor when the reverse current braking happens is shown in Figure 14.

2.1.4. Dynamic Braking

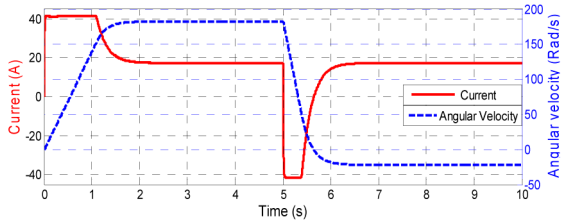

Figure 15. DCM current and speed in CLPWM-DCM when the dynamic braking arises.

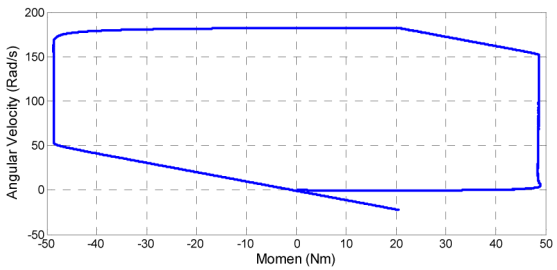

Figure 16. Characteristic of DCM in CLPWM-DCM system when the dynamic braking happens.

At time t = 5(s), the voltage supplied to the DCM is rapidly reduced from the rated voltage to 0V with the voltage reduction rate as (1). If the DCM load is an inertial one, its speed at this time decreases slowly, not corresponding to the rate of voltage drop, so the DCM current now is negative.

At this time, the PWM rectifier allows current to flow in the opposite direction, the excess energy on the DC side flows to the AC side as shown in Figure 15. At this point, the regenerative braking takes place, the operation of the DCM is in quadrant II (Figure 16). This is an advantage that thyristor-using rectifiers cannot have.

Under the influence of the load gravity, the DCM speed decreases gradually to 0 (Rad/s). When the speed is 0(rad/s), the armature current would be 0(A). When the current is zero, the DCM torque is also zero. At this time, the torque is less than the load potential torque, so the DCM reverses rotation and accelerates in the opposite direction. At this time, the dynamic braking happens, the operation of DCM is in quadrant IV and the characteristic of the motor is shown (Figure 16).

When the DCM speed increases (in the negative direction), the DCM current would also increase, so the DCM torque would rise. When the DCM torque and load torque are equal, the motor works stably in quadrant IV (dynamic braking happens) as shown in Figure 16.

To see the advantages of the CLPWM-DCM system, this system is compared with the traditional T-D system. For the CLPWM-DCM system, the PWM rectifier is able to allow the armature current to flow in the opposite direction (Figure 15). Therefore, when we reduce the armature voltage in order for the dynamic braking to happen, regenerative braking at first arise, allow energy to flow to the AC side (Figure 15).

The characteristic of the DC in the CLPWM-DCM system is shown in Figure 16. For the T-D system, the current in the thyristor rectifier cannot flow in the opposite direction. Therefore, when the voltage is reduced in order for dynamic braking to take place, the rectifier does not allow the excess energy to flow to the AC side (Figure 17). This leads to a waste of energy on the DC side when reducing DCM armature voltage to allow the dynamic braking to happen. The characteristic of the motor when the dynamic braking happens is shown in Figure 18. This is the disadvantage of the T-D system compared with the CLPWM-DCM one.

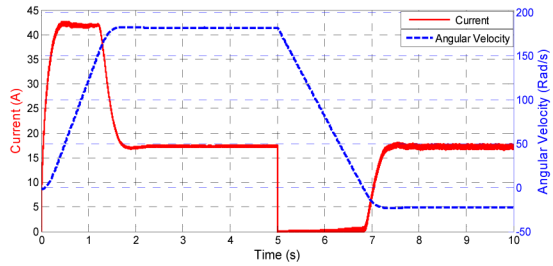

Figure 17. DCM current and speed in T-D system when the dynamic braking happens.

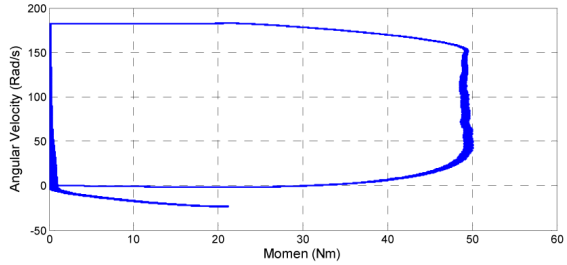

Figure 18. Characteristic of DCM in the T-D system when the dynamic braking happens.

2.2. Quality analysis of DC voltage

To see the advantages of the CLPWM-DCM system compared to the T-D system, the peak-to-peak ripples of the DC voltage at the output of the PWM rectifier and the 3-phase bridge rectifier using thyristors in the T-D system is simulated, compared and analyzed.

Figure 20 shows the peak-to-peak ripple of the DC voltage at the output of the PWM rectifier in a CLPWM-DCM system is about 3(V), approximately 1.25% of the average value of the DC voltage.

Meanwhile, the peak-to-peak ripple of the DC voltage at the output of the 3-phase bridge rectifier using thyristors in the T-D system in the case of the best output voltage quality of this system ($\alpha = 0^o$) is about 38(V) (Figure 19), approximately 15% of the average DC voltage. Therefore, it can be said that the output voltage quality of the PWM rectifier in the CLPWM-D system is better than the output voltage quality of the thyristor rectifier in the T-D system. This helps the motor in the CLPWM system to work more quietly, reducing the losses in the system.

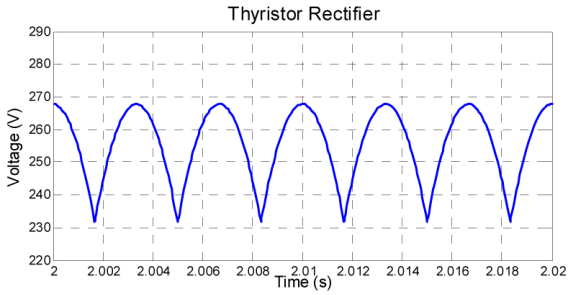

Figure 19. The quality of DC voltage at the output of the 3-phase bridge rectifier with the firing angle $\alpha = 0^o$ in T-D system.

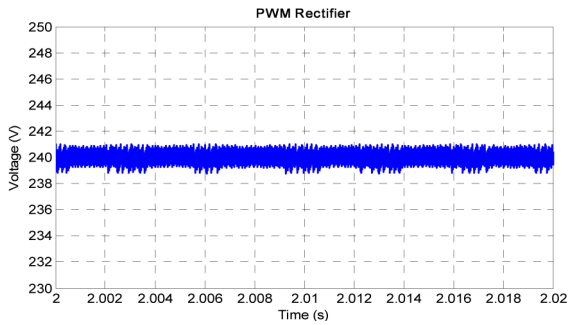

Figure 20. DC voltage quality at output of PWM rectifier in CLPWM system-DCM (zoomed).

To analyze the influence of inductor L and capacitor C on the quality of DC voltage supplied to the DCM in the T-D system, the author simulates the T-D system when adding 2 elements L and C to the system (Figure 21). The values of these two elements L and C in the CLPWM-DCM system and the T-D system are the same (See Table 1). The obtained results show that the peak-to-peak ripple of output voltage in the T-D system is significantly reduced, but the transient time of the system is very large, about 3.5 seconds (Figure 22). This transient time is approximately 3 times larger than that of the CLPWM-DCM system (Figure 23). So, the practical applicability of the T-D system when connecting inductors L and capacitor C is very limited, especially cannot be used in systems that need fast adjustment speeds such as robots, textile machines or electric cars, etc.

https://doi.org/10.52111/qnjs.2021.15508

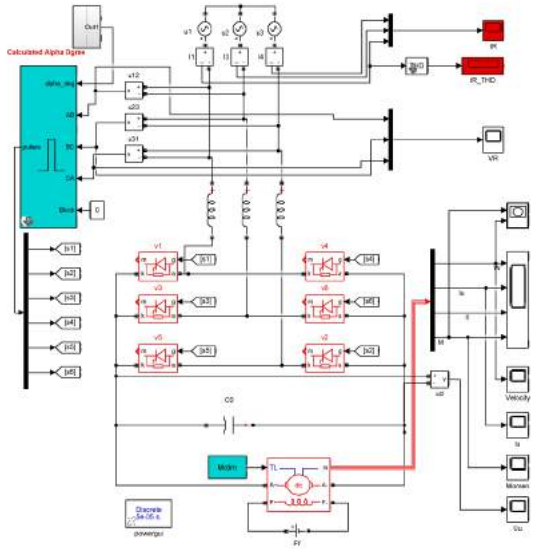

Figure 21. T-D system when adding inductor L and capacitor C.

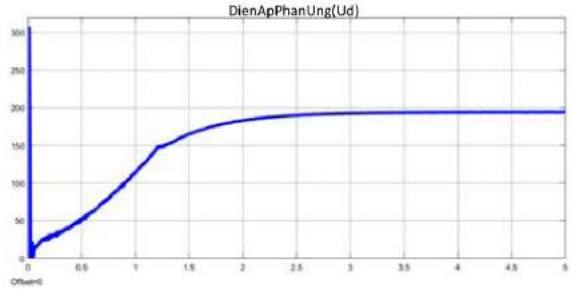

Figure 22. DC voltage in the T-D system when L and C are added.

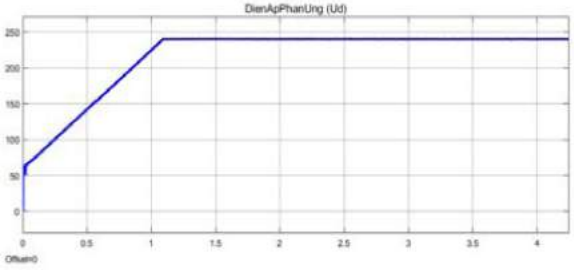

Figure 23. Transient time of CLPWM–DCM system.

2.3. Analysis of high order harmonics

To see the distortion of the alternating current in front of the rectifier in the T-D and in the CLPWM-DCM system, the author uses the fast Fourier analysis tool in Matlab software to analyze the spectrum of the AC current. In this way, alternating current form in front of the rectifier and the total harmonic distortion (THD) of this current were obtained.

Figure 24 and Figure 25 show the alternating current at the input of the rectifier in the T-D system with a non-sine form. From these two figures, it can be seen that the larger the firing angle α is, the greater the distortion of the input current and the larger the current harmonics (THD). For example, When α = 0°, THD = 31.11% (Figure 24); When α = 90°, THD = 33.09% (Figure 25).

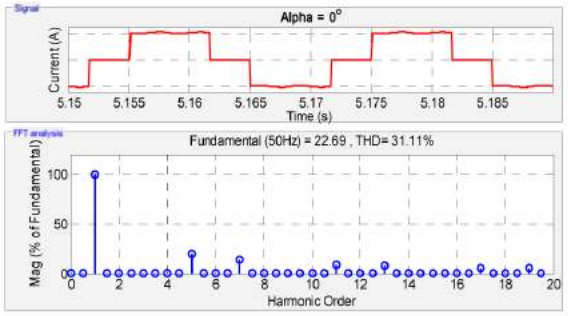

Figure 24. Current and THD of current with firing angle α = 0° in T-D system.

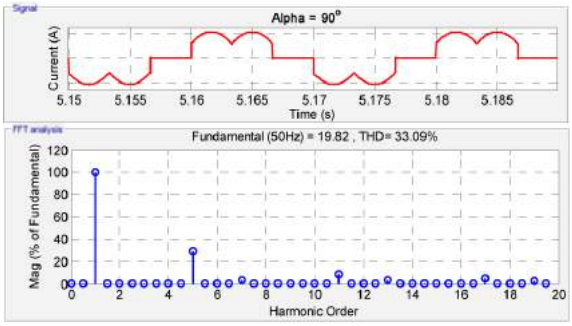

Figure 25. Current and THD of current with firing angle α = 90° in T-D system.

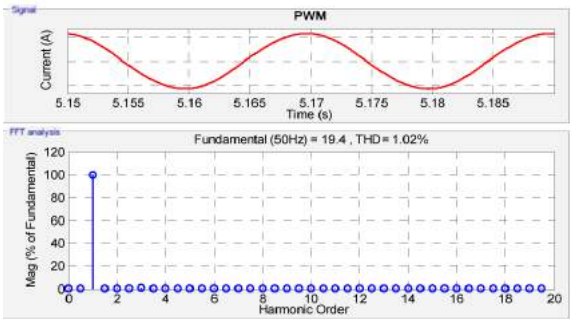

Figure 26. Current and THD of current in CLPWM-DCM system.

Figure 27 shows the simulation results of the current form and the total harmonic distortion THD of the alternating current in front of the PWM rectifier, THD = 1.02%. Comparing the simulation results in Figure 27 with Figure 25 and Figure 26, it can be seen that the PWM rectifier in the CLPWM-DCM system does not

distort the AC current at the input of the rectifier as much as in the case of the rectifier using thyristor in the T-D system. In other words, this input AC current has an almost ideal sine form, and the THD of the current is very small with 1.02%.

To analyze the influence of the inductor L and capacitor C on the current distortion at the input of the rectifier in the T-D system, the author conducts a simulation of the T-D system when adding two L and L elements into this system (Figure 21). The values of these two elements L and C in the T-D system and those in the CLPWM-DCM system was the same (See Table 1). The obtained results show that when adding the inductor L to the T-D system, the total harmonic distortion of the system is reduced, from 31.11% (Figure 24) to 23.14% (Figure 27). However, the THD of current in T-D system is 23.14%, which is still much larger than that in the CLPWM-DCM system, THD = 1.02% (Figure 26).

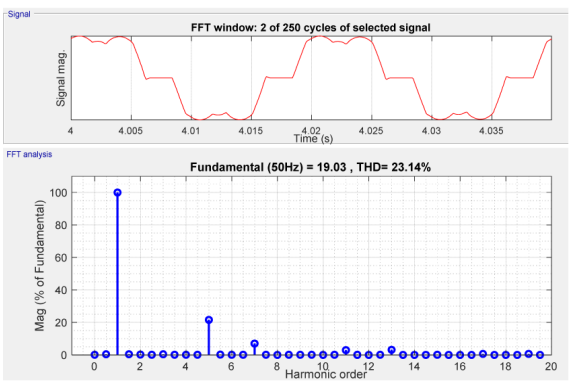

Figure 27. Current and THD of current with firing angle α = 0° in T-D system.

In addition, when we add L and C elements into the T-D system, the DC voltage value feeding to the DCM is significantly reduced, dropping from 514(V) (voltage corresponding to the firing angle α = 0° to 190(V) (Figure 22). Actually, the voltage feeding to the DCM has significantly reduced because of a voltage drop on the additional reductor L in the system. Therefore, adding an inductor L with a large inductance value to the T-D system helps reduce the amount of high-order harmonics returned to the system's grid, but not significantly. In addition, the voltage drop on the inductor is too large, making the system no longer optimal, so it is not prioritized.

3. CONCLUSION

The simulation, comparison and analysis results in the paper show that the T-D drive system still has many disadvantages. In addition, the article also shows that the CLPWM-DCM drive system has many advantages and can overcome many disadvantages of the traditional T-D system. For instance, it does not distort the alternating current in front of the rectifier; The total harmonic distortion of the input current in front of the rectifier is low; The peak-to-peak ripple of the rectifier output voltage is low; It is possible to allow current to flow in two directions, enabling the exchange of energy between the DC side and the AC side easily. However, the CLPWM-DCM drive system also has the disadvantage that the design and control of the system are relatively complicated.

Acknowledgement

This research is conducted within the framework of science and technology projects at institutional level of Quy Nhon University under the project code T2020.671.19.

4. REFERENCES

1. Bui Quoc Khanh, Nguyen Van Lien, and Nguyen Thi Hien. *Electric Drives*, Science and Technics Publishing House, Hanoi, 2004.
2. Bui Dinh Tieu. *Textbook of electric drives*, Science and Technics Publishing House, Hanoi, 2007.
3. P. Zhu, Y. Wei, Z. Zheng, X. Wang, & F. Ma. Fractional modelling and simulation for single-phase PWM rectifier, *The Journal of Engineering*, **2019**, *16*, 1675-1678.
4. R. Wang, F. Wang, D. Boroyevich, R. Burgos, R. Lai, P. Ning & K. Rajashekara. A high power density single-phase PWM rectifier with active ripple energy storage, *IEEE Transactions on Power Electronics*, **2010**, *26*(5), 1430-1443.

5. Z. Yongchang et al. Grid-voltage sensorless model predictive control of three-phase PWM rectifier under unbalanced and distorted grid voltages, *IEEE Transactions on Power Electronics*, **2019**, 8663-8672.

6. R. J. Wai & Y. Yang. Design of backstepping direct power control for three-phase PWM rectifier, *IEEE Transactions on Industry Applications,* **2019**, *55*(3), 3160-3173.

7. M. Li, X. Wu, S. Huang & G. Liang. Model predictive direct power control using optimal section selection for PWM rectifier with reduced calculation burden, *International Journal of Electrical Power & Energy Systems,* **2020**, *116*, 105552.

8. C. Zhang, S. Yu & X. Ge. A stationary-frame current vector control strategy for single-phase PWM rectifier, *IEEE Transactions on Vehicular Technology*, **2019**, *68*(3), 2640-2651.

9. A. Bouafia, J. P. Gaubert, and F. Krim. Predictive direct power control of three-phase pulsewidth modulation (PWM) rectifier using, *IEEE Transactions on Power Electronics*, **2010**, *25*, 228–236.

10. P. Rodríguez, J. Pou, J. Bergas, J. I. Candela, R. P. Burgos, and D. Boroyevich. Decoupled double synchronous reference frame PLL for power converters control, *IEEE Transactions on Power Electronics*, **2007**, *22*, 584–592.

11. R. Ghosh and G. Narayanan. A simple analog controller for single-phase half-bridge rectifier, *IEEE Transactions on Power Electronics*, **2007**, *22*, 186–198.

12. N. Mohan. *Power electronics: a first course*, John Wiley & Sons, 2012.

13. R. Ghosh, and G. Narayanan. Control of three-phase, four-wire PWM rectifier, *IEEE Transactions on Power Electronics*, **2008**, *23*(1), 96-106.

14. Doan Quang Vinh, Doan Duc Tung, Bui Van Vu. Starting separately excited direct current motor by varying armature voltage, *Journal of Science and Technology, University of Danang*, **2017**, *1*(3), 73–78.

TẠP CHÍ KHOA HỌC
TRƯỜNG ĐẠI HỌC QUY NHƠN

Nghiên cứu điều chế mỡ bôi trơn từ dầu nhờn thải tái sinh

Lê Thu Hương*, Trương Thanh Tâm

Khoa Khoa học tự nhiên, Trường Đại học Quy Nhơn, Việt Nam

Ngày nhận bài: 11/05/2020; Ngày nhận đăng: 05/08/2020

TÓM TẮT

Mỡ bôi trơn được điều chế bằng cách tổng hợp từ dầu khoáng và chất làm đặc. Trong nghiên cứu này, mỡ bôi trơn được làm từ chất làm đặc như NaOH, dầu lạc (PO) được kết hợp với dầu nhờn thải tái sinh (RLO) trong phòng thí nghiệm. Kết quả cho thấy tỷ lệ phù hợp của NaOH/PO/RLO là 3,7/13/18, thời gian và nhiệt độ tối ưu cho tổng hợp mỡ bôi trơn là khoảng 55 phút và 105-110 ^{o}C. Mỡ thành phẩm thu được có nhiệt độ nhỏ giọt và độ xuyên kim là 116 ^{o}C và 176 mm.

Từ khóa: *Mỡ bôi trơn, dầu nhờn thải tái sinh, dầu lạc.*

**Tác giả liên hệ chính.*
Email: lethuhuong@qnu.edu.vn

JOURNAL OF SCIENCE
QUY NHON UNIVERSITY

A study on the preparation of greases from recycling of used lubricating oil

Le Thu Huong*, Truong Thanh Tam

Faculty of Natural Science, Quy Nhon University, Vietnam

Received: 11/05/2020; Accepted: 05/08/2020

ABSTRACT

Greases were made by combining a fluid lubricant and a thickener. In this research, the grease was synthesized from thickener materials such as NaOH, and peanut oil (PO), which dispersed in recycled lubricating oil (RLO) in the laboratory. The result shows that the suitable ratio of NaOH/PO/RLO was 3,7/13/18; the achieved time and temperature for synthesizing grease were about 55 minutes and 105 - 110^{o}C, respectively. It was demonstrated that the optimal grease dropping point and the needle penetration were 116^{o}C and 176 mm, respectively.

Keywords: *Greases, recycled lubricating oil, peanut oil.*

1. INTRODUCTION

Nowadays, lubricating oil plays an important role in industrial manufactory and daily life. Application of lubricants is to lubricate moving parts, to reduce friction and to reduce equipment's wear. However, lubricants have some drawbacks such that they cannot lubricate some positions such as bearings at extremely high temperature, or equipment at large load of working condition. As a result, lubricants are replaced by greases. Today, greases are used with relatively large quantities, and they have properties and effects that lubricating oil does not have.[1-6] There are many sources of materials and methods to manufacture greases for various usages. In addition, using recycled lubricants to replace mineral oil for making grease is necessary. Currently, the process of manufacturing grease from recycled lubricants has not been produced on an industrial scale. In fact, this process has only been studied in laboratory and done manually. Utilizing lubricant or waste is denatured and deteriorated by the oxidation. There are valuable hydrocarbons remaining in the composition of discarded waste lubricant, which will have an impact on the environment after releasing without any treatment. Many methods have been applied to recycle them regarding to reusing this source and environmental issues. After regenerating, lubricant is provided with additives to be reused as lubricating oil.[7-12] However, recycled lubricants have some drawbacks such as color, viscosity and some other parameters are still lower than TCVN 8939-9: 2011, so they can only be used for agricultural machinery. To solve these shortcomings, recycled lubricating oil was studied from the aspect of its combination with secondary peanut oil to make grease.

2. EXPERIMENT

2.1. Raw materials: Recycled lubricating oil, peanut oil (Quy Nhon)

*Corresponding author.
Email: lethuhuong@qnu.edu.vn

https://doi.org/10.52111/qnjs.2021.15509

2.2. Chemical: NaOH 96% (China), $BaCl_2$ (China), HCl 36% (Vietnam), KOH 85% (China), phenolphtalein solution 1%, ethyl alcohol 99.5% (Vietnam), glycerin.

3. RESULTS AND DISCUSSION

3.1. Recycle waste lubricants

The waste lubricants are recycled by acid treatment method and the basic four-step procedure as follows:

Step 1: Dehydrate and remove mechanical impurities

The vehicle waste oil is collected and filtered by a vacuum filter to remove large-sized impurities. It is then heated at 110°C for 15 minutes to dehydrate and evaporate the light fuel in the oil.

Step 2: Treat the waste lubricants with acetic acid

100 ml of the dehydrated waste oil (in Step 1) is poured into a 250 ml beaker under at 50 °C. Then 17.5 ml of acetic acid is added at the concentration ≥ 99.5%. The mixture sample is stirred for an hour at 50 °C. After that, the sample is cooled down to room temperature and centrifuged for 20 minutes at rotating speed of 6,000 rpm to separate the residue from the waste oil. The results show that after recycling this oil has a light brown color and its viscosity was 54.5 cSt at 40 °C.

Step 3: Neutralize acid with NaOH solution

80 ml of acid-treated oil is put into a 250 ml beaker, and stirred under to the heat of 80 °C, then 7 ml of 45% NaOH solution is added into the prepared mixture. After 30 minutes, the results reveal that after recycling the oil sample is light reddish brown (Figure 1), and its viscosity is 78.4 cSt at 40 °C.

Step 4: Clean oil with adsorbent

50 grams of Binh Dinh clay mineral material is added into 100 ml of base treated oil. The mixture is homogeneously stirred for 30 minutes at 110 °C. The obtained product -collected using vacuum filtrationis named recycled lubricating oil.

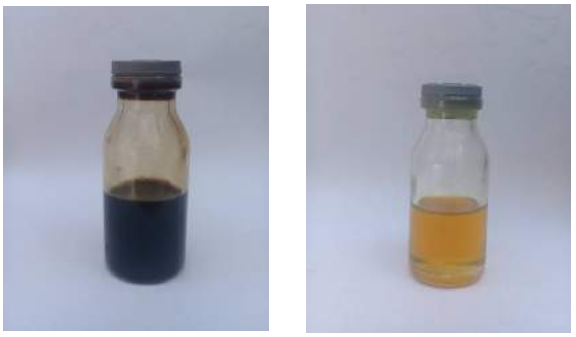

(a) (b)

Figure 1. Photo images of (a) Motorcycle waste lubricant, and (b) Lubricants after regeneration

3.2. Produce lubricants from recycled lubricating oil

The production of lubricants from regenerated waste lubricants with a thickener using the saponification reaction between NaOH and peanut oil is carried out as follows:

Step 1: The raw materials are prepared including recycled lubricating oil, NaOH 30% and peanut oil.

Step 2: The optimal NaOH/PO ratio is investigated in reaction time and reaction temperature to create a thickener.

Step 3: The ingredients are added into a 250 ml glass beaker as summarized in Table 1.

Table 1. Ingredients raw materials for the manufacture of lubricants

Recycled Lubricating oil (grams)	NaOH 30% (ml)	Peanut oil (grams)
18	3.7	13

Step 4: The prepared beaker is heated in glycerin bath using electric stove for the saponification reaction to occur at 85 ÷ 90 °C for 45 minutes, and keeping stirring during greasing with stirring speed 60 ÷ 70 rpm.

Step 5: To get the stable fat mass homogenization phase, the mixture solution

should maintain from 85 ÷ 90 °C in Step 4 to 105 ÷ 110 °C for varying duration (10 min), the consistency and color of the grease are observed and the electric stove is turned off.

3.3. Investigate the saponification process experimentally to create a thickener

3.3.1. Optimal ratio between NaOH and peanut oil (NaOH/PO)

The experiment is performed for 40 minutes at 80 ÷ 85 °C, and kept stirring at 60 ÷ 70 rpm with specific NaOH/PO ratios. The result is shown in Table 2.

Table 2. Optimal ratio between NaOH and peanut oil (NaOH/PO)

Ratio NaOH/PO (ml/g)	Value balance NaOH (%)	Comments Result
3.0/13	0	Liquid, light white, oil film
3.7/13	0.078	Solid, light yellow
4.0/13	0.115	Solid, light yellow
4.5/13	0.202	Solid, light yellow
6.0/13	0.37	Slightly hard, light yellow
7.5/13	0.557	Hard, lumpy, light yellow

Greases highly depend on the quality of the thickener (saponification). Therefore, the optimal NaOH/PO ratio plays an important role to improve the fat quality. As can be seen in Table 3.2, the optimal NaOH/PO ratio is 3.7 ml NaOH and 13 grams PO for the saponification reaction.

3.3.2. Effect of reaction time on soap consistency

The reaction time is investigated to optimal the soap consistency. Experimental results are shown in Table 3.

Table 3. Reaction time affecting the consistency of the soap

Sample	Time Counter Response (minutes)	Remarks on consistency of soap
1	35	Liquid, white
2	40	Slightly thick, white
3	45	Solid, smooth, smooth, light yellow color
4	50	Solid, porous, light yellow
5	55	Slightly hard, porous, light yellow
6	60	Hard, lumpy, straw yellow

From the above results, it is obvious that the reaction time to create the optimal thickening soap sample is 45 minutes. This value is very important to make a preliminary assessment and predicts the thickener quality. Based on this, we can make adjustments to create the optimal grease product.

3.3.3. Effect of reaction temperature on soap consistency

Since the consistency of the soap sample depends on the temperature of the saponification reaction, the optimum temperature of the soap reaction is further investigated. The survey results are presented in Table 4:

Table 4. Effect of temperature on the quality of a soap sample

Sample	Temperature (°C)	Density of soap
1	75÷80	Slightly liquid and smooth
2	80÷85	Solid, smooth
3	85÷90	Slightly hard, gritty
4	90÷95	Hard, lump

According to the sensory evaluation, the optimal reaction temperature for saponification is 85 °C ÷ 90 °C. At this temperature, the soap

https://doi.org/10.52111/qnjs.2021.15509

sample has a moderate consistency, smoothness, and suitability for thickening in the process of grease formation. At higher temperatures, the consistency increases, but the soap sample appears to be thick, hard, and it solidifies into a block and has a burning odor.

3.4. Experimental investigation of grease synthesis process

3.4.1. Optimal ratio between the amount of recycled lubricating oil (RLO) and the thickener (NaOH/PO)

Experimental results are presented in Table 5 as follows.

Table 5. Optimal ratio between the amount of RLO and the thickener (NaOH/PO)

Sample	RLO (grams)	Results and comments about fat
1	16	Thick, hard, slightly gritty, compact, bad stickiness, dark yellow
2	18	Solid, viscous, lustrous on the surface, dark yellow begins to turn red
3	20	Slightly loose, straw-yellow, smooth, glossy grease surface
4	22	Liquid, yellow
5	24	Liquid, yellow

As can be seen from Table 5, Sample 2 has the optimal consistency, color, and the glossiness in comparison to the other samples. Therefore, Sample 2 is chosen as the optimum ratio of raw material to produce grease.

3.4.2. Effects of reaction time on the quality of lubricants

The quality of the grease such as consistency, needle penetration, drip temperature, etc. is quite dependent on the reaction time. Therefore, the reaction time is varied from 40 minutes, 45 minutes, 50 minutes, 55 minutes, 60 minutes respectively with the reaction temperature of 85 ÷ 90 ^{o}C in the saponification phase, and 105 ÷ 110 ^{o}C at the homogenizing stage to create fat. The optimal rate of raw materials (NaOH/PO/Ethnic minorities) is 3.7/13/18 while stirring speed is adjusted at 60 ÷ 70 rpm. Then, the experiments are proceeded to determine the dropping point and needle penetration of the above samples.

The experimental results in Figure 2 show that the reaction time to create a grease with a suitable consistency is 55 minutes (saponification time is 45 minutes and grease homogenization time is 10 minutes), and the reaction time is 10 minutes. This application of the resulting grease has a good consistency and color. Especially, it appears to be lustrous on the grease surface.

Thus, a grease sample with a reaction time of 55 minutes has the optimal drip temperature of 118 °C.

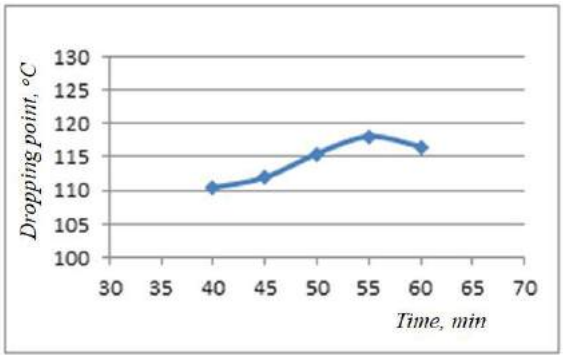

Figure 2. Effect of reaction time on dropping point of grease

3.4.3. Effect of the reaction time on the needle penetration of grease

The experimental results of investigating the effect of reaction time on the needle penetration of grease are shown in Figure 3.

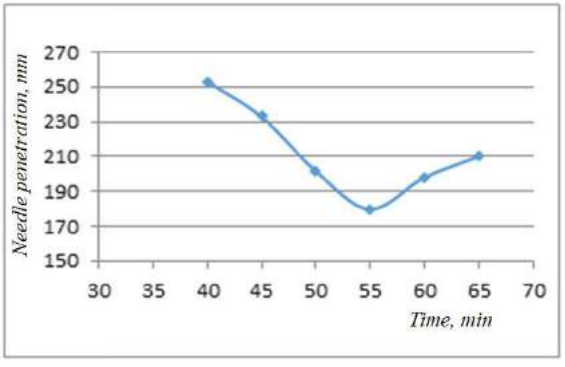

Figure 3. Effect of reaction time on needle penetration of grease

So the grease with a needle penetration of 176 mm is chosen as the grease sample to ensure the smallest needle penetration, which means that the fat consistency is the optimal parameter.

3.4.4. Effect of reaction temperature on the quality of the grease

To investigate the effect of reaction temperature on the quality of the grease, we fix all the investigated factors at the saponification stage, and stir in the grease homogenization stage with a duration of 10 minutes in different temperature ranges. Experimental results are shown in Table 6.

Table 6. Effect of reaction temperature on the quality of the grease

Sample	Temperature stage copper most fat (°C)	Comment on the results	
		Grease consistency	Dropping point (°C)
1	100÷105	Liquid, straw yellow, smooth	112.5
2	105÷110	Solid, yellow bold, smooth, glossy	117.5
3	110÷115	Solid, gritty, from red to shiny yellow	113.5
4	115÷120	turning to liquid	-
5	120÷125	Colloidal solution, lost ability to lubricate the surface, dark red	-

The optimal fat homogenization stage is formed in the range temperature of 105 ÷110 °C. At this uniform temperature, the resulting grease has a smooth, color and luster that ensures the basic properties of the grease. Herein, the fat has a dropping point of 117.5 °C.

3.5. Comparison of experimental results at Chemical Engineering Laboratory, Quy Nhon University and measured results at Quality Standard Technical Center 2 (Da Nang)

Table 7. Comparison of sample measurement results

Serial	Expense	Results measured at the lab of technology, catalytic materials and petro chemicals	Measurement results at the Center for Standards Technical, Metrology and Quality 2
Dropping point (°C)	ASTM D 566	117.5 ÷118	116
Needle penetration (mm)	ASTM D 217	178	176

Based on the experimental data shown in Table 7, we can see the reliability of measured data, analyzing fat samples at the Chemical Engineering laboratory. With the obtained data: the dropping point is 116 °C and the needle penetration is 176 mm, some machine parts can be used to lubricate some machine parts with a working temperature of less than 116 °C.

Some pictures of synthetic grease samples are showed in Figure 4

(a)

(b)

(c)

(d)

https://doi.org/10.52111/qnjs.2021.15509

(e)

Figure 4. Photo images of fat samples during synthesis process

a) Solid, dark yellow, smooth, glossy

b) Liquid, yellow

c) Thick, hard, slightly gritty, poor adhesion, dark yellow

d) Thick, hard, slightly gritty, poor adhesion, dark yellow

e) Solid, gritty, yellow falls red

4. CONCLUSIONS

On the basis of the obtained experimental results, we can reach the following conclusions:

- The most optimal ratio between NaOH/ PO/RLO to synthesize good quality grease is 3.7/13/18 (ml/g/g).

- The optimal reaction temperature for grease synthesis is 85 ÷ 90 ^{o}C in the saponification stage and 105 ÷ 110 ^{o}C in the grease homogenization stage.

- The optimal reaction time for grease synthesis is 55 minutes (45 minutes for the saponification phase and 10 minutes for the grease homogenization phase).

- The optimal dropping point of the grease in the experimental process with the raw material ratio, reaction time, and optimal reaction temperature is 116 ^{o}C.

- The needle penetration of the grease determined in the optimal experimental process is 176 mm.

REFERENCES

1. Tran Van Trieu, Nguyen Dai Le. *Grease and Fuel Textbook*, Hanoi Department of Education and Training Publishing House, 2005.

2. Ngo Thi Ngoc Han, Bui Thi Buu Hue. Synthesis of biological lubricants from used Tra fish fat, Basa fish and vegetable oil, *Journal of Science*, **2010**, *13,* 50-58.

3. Tran Kim Ngan. Research on the factors affecting the waste lubricant regeneration process, master thesis, *Journal of Science - Quy Nhon University*, **2017**, 36-37.

4. J. K. Adesodun, J. S. C. Mbagwu. Biodegradation of waste-lubricating petroleum oil in a tropical alfisol as mediated by animal droppings, *Bioresource Technology*, **2008**, *99,* 5659–5665.

5. Cheryl Yeung Suet Ling. *Production of high temperature grease from waste lubricant sludge and silicone oil*, Faculty of Chemical and Natural Resources Engineering Universiti Malaysia Pahang, 2010, 1-14.

6. A.U.C. Maduako, G.C. Ofunner, C.M. Ojinnaka. The role of metals in the oxidative degradation of automotive crankcase oils, *Tribology International*, **1996**, 29, 153 – 160.

7. M. J. Fuentes, R. Font et al. Pyrolysis and combustion of waste lubricant oil from diesel cars: Decomposition and pollutants, *Journal of Analytical and Applied Pyrolysis*, **2007**, *79*(1–2), 215–226.

8. F. Owrang, H. Mattsson, J. Olsson, Pedersen. Investigation of oxidation of a mineral and a synthetic engine oil, *Thermochimica Acta*, **2004**, *413,* 241–248.

9. R. R. Mohammed, I. A. R. Ibrahim, A. H. Taha. Waste lubricating oil treatment by extraction and adsorption, *Chemical Engineering Journal*, **2013**, *220*, 343 – 351.

10. Seung – Soo Kim, Byung Hee Chun, Sung Hyun Kim. Non– thermal pyrolysis of waste automobile lubricating oil in a stirred batch reactor, *Chemical Engineering Journal*, **2003**, *93*, 225 – 231.

11. S. S. Kim, S. H. Kim. Pyrolysis kinetics of waste automobile lubricating oil, *Fuel,* **2000**, *79*, 1943–1949.

12. T. Yusaf, B. F. Yusaf, M. M. Elawad. Crude palm oil fuel for diesel – engines: Experimental and ANN simulation approaches, *Energy*, **2011**, *36,* 4871–4878.

JOURNAL OF SCIENCE
QUY NHON UNIVERSITY
http://js.qnu.edu.vn
Vol. 15, N° 5, 2021
ISSN : 1859-0357

CONTENTS

1. Research on the capture of flue gases of the metal-organic framework $Ni(BDC)(TED)_{0.5}$ by the classical simulation method
Nguyen Thi Xuan Huynh , Bui Thi Duyen, Pham Thao Tram, Tran Thi Diem Thanh, and Nguyen Truong My Duyen 6

2. Application of Raspberry and PLC Mitsubishi to the design of tomato classified system automatically
Bui Van Vu, Nguyen Duc Thinh, Pham Thanh Binh, Do Van Can 14

3. Analysis of electromagnetic on transformer due to inrush power system by Ansys Maxwell
Doan Thanh Bao, Ha Huynh Huy Vu 22

4. Design of control and monitoring system for smart distributed urban lighting system
Le Thai Hiep, Dinh Quoc Dat 30

5. Classification of ECG images by Deep Learning to support the diagnosis of cardiovascular diseases
Le Xuan Vinh, Le Xuan Viet, Vu Hoang Thuong 40

6. Theoretical study on adsorption of sulfamethoxazole on rutile-TiO_2 (110) surface using quantum chemical method
Nguyen Ngoc Tri, Nguyen Tien Trung 48

7. H∞ fault estimation problem for a class of time-delay systems using a new state transformation
Dang Thi Kim Hong, Le Ba Thong, Dinh Cong Huong 56

8. A survey of working models of direct current motor in PWM rectifier - separately excited direct current motor system
Bui Van Vu, Vo Phuong, Do Van Can, Le Thai Hiep 76

9. A study on the preparation of greases from recycling of used lubricating oil
Le Thu Huong, Truong Thanh Tam 88